UNLV | UNIVERSITY LIBRARIES

UNLV Theses, Dissertations, Professional Papers, and Capstones

5-1-2014

Simulation of Thermal Transit-Time Flow Meter for High Temperature, Corrosive and Irradiation Environment

Elaheh Alidoosti
University of Nevada, Las Vegas

Follow this and additional works at: https://digitalscholarship.unlv.edu/thesesdissertations

Part of the Electrical and Computer Engineering Commons, and the Mechanical Engineering Commons

Repository Citation

Alidoosti, Elaheh, "Simulation of Thermal Transit-Time Flow Meter for High Temperature, Corrosive and Irradiation Environment" (2014). *UNLV Theses, Dissertations, Professional Papers, and Capstones*. 2053.
http://dx.doi.org/10.34917/5836072

This Thesis is protected by copyright and/or related rights. It has been brought to you by Digital Scholarship@UNLV with permission from the rights-holder(s). You are free to use this Thesis in any way that is permitted by the copyright and related rights legislation that applies to your use. For other uses you need to obtain permission from the rights-holder(s) directly, unless additional rights are indicated by a Creative Commons license in the record and/or on the work itself.

This Thesis has been accepted for inclusion in UNLV Theses, Dissertations, Professional Papers, and Capstones by an authorized administrator of Digital Scholarship@UNLV. For more information, please contact digitalscholarship@unlv.edu.

SIMULATION OF THERMAL TRANSIT-TIME FLOW METER FOR HIGH TEMPERATURE, CORROSIVE AND IRRADIATION ENVIRONMENT

By

Elaheh Alidoosti

Bachelor of Science
University of Shahid Beheshti
Tehran, Iran
2003

A thesis submitted in partial fulfillment
of the requirements for the

Master of Science in Engineering - Electrical Engineering

Department of Electrical and Computer Engineering
Howard R. Hughes College of Engineering
Graduate College

University of Nevada, Las Vegas
May 2014

Copyright by Elaheh Alidoosti 2014
All Rights Reserved

UNLV
UNIVERSITY OF NEVADA LAS VEGAS

THE GRADUATE COLLEGE

We recommend the thesis prepared under our supervision by

Elaheh Alidoosti

entitled

Simulation of Thermal Transit-Time Flow Meter for High Temperature, Corrosive and Irradiation Environment

is approved in partial fulfillment of the requirements for the degree of

Master of Science in Electrical Engineering
Department of Electrical and Computer Engineering

Yingtao Jiang, Ph.D., Committee Chair

Biswajit Das, Ph.D., Committee Member

Mei Yang, Ph.D., Committee Member

Hui Zhao, Ph.D., Graduate College Representative

Kathryn Hausbeck Korgan, Ph.D., Interim Dean of the Graduate College

May 2014

ABSTRACT

Simulation of Thermal Transit-Time Flow meter for High temperature, Corrosive and Irradiation Environment

By

Elaheh Alidoosti

Dr. Yingtao Jiang, Examination Committee Chair
Associate Professor of Electrical Engineering
University of Nevada, Las Vegas

In the environments of high temperature (300^{o} C – 1000^{o} C), corrosive and even irradiation application, the challenges of providing reliable and accurate flow rate measurement is significant. In comparing with many other existing technologies for normal operation environments, correlated thermal transit-time flow meter show its advantages of resolving the challenges encountered in those harsh conditions. The correlated thermal signals can be detected by two separated thermal sensors (for example, thermocouples) in series alignment along the pipe, and derive the flow rate. It was evaluated to have accurate measurement for small pipe at slow fluid speed. In the higher flow rate and big pipe size application, this technology shows its weakness due to the limitations associated with slow response time of thermal sensor, dimension, and low strength of thermal signal. In this project, we present a sophisticated layout of thermal transit-time flow meter with validation of numerical simulation and experiments. We observed that the simulation results are in good agreement with the experimental results and showing that the measured flow is successfully extended to high range and with stable and accurate measurement results. Also, the linear hypothesis of ratio between the bypass to the main flow was successfully tested.

ACKNOWLEDGMENT

Many thanks to Dr. Yingtao Jiang, my advisor and committee chair and Dr. Jian Ma, my co-adviser for their helpful comments, suggestions and fruitful contributions during this project.

This thesis research has been sponsored by a DOE NEUP program (Department of Energy, Nuclear Engineering University Program).

TABLE OF CONTENTS

ABSTRACT iii

ACKNOWLEDGMENT iv

LIST OF TABLES ix

LIST OF FIGURES xi

CHAPTER 1 1

INTRODUCTION 1

1.1 Differential Pressure 2

1.2 Pitot Tubes 3

1.3 Velocity Flowmeter 4

1.4 Calorimetric 4

1.5 Positive Displacement Flowmeters 4

1.6 Turbine 5

1.7 The magnetic flowmeter 5

1.8 Electromagnetic flowmeters 6

1.9 Mass flowmeters 6

1.10 Thermal Mass Flowmeters 6

1.11 Coriolis Flowmeter 7

1.12 Ultrasonic flowmeters 7

1.13 The vortex flow meter 9

1.14 Paddlewheel 10

1.15 Float Type 10

1.16 Open Channel Flowmeters....10

CHAPTER 2 13

CORRELATED THERMAL SIGNALS BASED FLOWMETER 13

2.1. Time delay estimation methods 13

2.2. Accuracy and error analysis....20

2.3. Verification of time delay estimation methods....23

2.4. Measurement and calibration of correlated thermal signals-based flowmeter 27

2.5. Experiments for calibration....32

CHAPTER 3 38

FLOW RATE MEASUREMENT WITH BY-PASS DESIGN 38

3.1.Bypass (Flow Ratio Technique)....39

3.2 Types of bypass flowmeters....42

CHAPTER 4 46

NUMERICAL SIMULATION OF THE DESIGNED FLOWMETER 46

4.1 Theoretical Equations 46

4.1.1 The Continuity Equations 46

4.1.2 The Momentum Equations....50

4.1.3 The Energy Equations....54

4.2 Simulations and Computations 58

4.2.1Geometry and Mesh....59

4.2.2 Verification and Validation of Mesh 62

4.2.3 Boundary Conditions 64

4.3 Results and Discussions 65
4.3.1 Temperature distribution along the pipe (Temperature contours) 66
4.3.2 Velocity distribution along the pipe 67
4.3.3 Time Delay and Flowrate Calculations 68
4.4 Geometry 74
4.5 Boundary Conditions and Parameter Settings 74
4.6 Verification and Validation of mesh results 76
4.7 Results and Discussions 78
4.7.1 Velocity distribution in the pipe 78
4.7.2 Turbulent fluid velocity in a pipe 79
4.7.3 Laminar and Turbulent Flows in pipes and Reynolds Number 81
4.7.4 Condition in bypass 85
4.7.5 Impact of different ratios of diameters 85
4.7.6 The theory of entrance region 86
4.7.7 Entry length 87
4.7.8 Impact of entrance length L 88
4.7.9 Impact of the bypass height 89
4.7.10 Impact of different angle 89
4.7.11 Pressure distribution in the pipes 93
4.7.12 Temperature distribution along the pipes 95
4.7.13 Flow rate calculation using signal processing method 98
4.8 Simulations of Experimental setup 102
4.8.1 Geometry and Mesh 102

4.8.2 Results and Discussions 103

CHAPTER 5 104

CONCLUSIONS 104

REFERENCES 105

VITA 108

LIST OF TABLES

Table1.1 Flowmeter's reliability in the nuclear industry. 11

Table 2.1 Periodic heating patterns 24

Table 2.2 FWHM and CPU time comparison of the methods with the same variance of estimated time delay of 0.005 seconds 27

Table 2.3 Linear fitting results for the one inch pipe. 35

Table 2.4 Linear fitting results for the half inch pipe. 35

Table 2.5 Calibrated results using Eq. (2.33) for the one inch pipe. 36

Table 2.6 Calibrated results using Eq. (2.33) for the half inch pipe. 36

Table 4.1 Calculated flowrate from time delay (3D Simulation) 72

Table 4.2 The experimental results. 72

Table 4.3 calculated the measurement error for experiment. 73

Table 4.4 Summary of boundary conditions 75

Table 4.5 Reynolds number in bypass 85

Table 4.6 Line fitted to different angles 92

Table 4.7 Calculation of Sigma over the average flow rates 92

Table 4.8: Pressure distribution along the pipe (with and without bypass) using simulations 95

Table 4.9 Pressure distributions along the straight pipe using calculations and compare with simulation 95

Table 4.10 Calculation of the response time of each thermocouple 97

Table 4.11 Simulation data for different velocities 100

Table 4.12 Error measurement data calculation. 101

Table 4.13 Ratio calculation of by-pass flowrtae to initial flowrate in steady state condition. 103

LIST OF FIGURES

Fig. 2.1 Transit time configuration. 13

Fig. 2.2 Cross correlation of thermal signals recorded by thermocouples..... 15

Fig. 2.3. System model for basic transfer function estimation. 15

Fig. 2.4. Transfer function estimation for noisy input and output. 16

Fig. 2.5 Impulse response of the system obtained from transfer function estimation. 17

Fig. 2.6 (a): The autocorrelation function of $i_1(t)$, (b): The cross correlation function of $i_1(t)$ and $i_2(t)$ 19

Fig. 2.7 (a): The windowed version of the autocorrelation function of $i_1(t)$, (b): The windowed version of cross correlation function of $i_1(t)$ and $i_2(t)$ 19

Fig. 2.8 Point by point cross-correlation..... 22

Fig. 2.9 A water-based test apparatus. 23

Fig. 2.10. Variance of estimated time delay for considered methods for flow rate of 2 gpm, sampling frequency of 10 Hz and for five different configurations: (i) CCF, (ii) AAIRF, (iii) MAFCCF with its moving average filter assuming a length of 2, (iv) MAFCCF with its moving average filter assuming a length of 4, and (v) MAFCCF with its moving average filter assuming a length of 6. 25

Fig. 2.11. Calculated flow rate deviation with respect to sampling frequency..... 26

Fig. 2.12 The full width at half maximum representation. 27

Fig. 2.13 The cross-section view of pipe showing the flow velocity distribution. 29

Fig. 2.14. Rising edge of the TC signal. 30

Fig. 2.15 The water-based test apparatus with pipe diameter of o.5 inch..... 33

Fig. 2.16 Flow velocity versus radius point for the 1 inch pipe using 10 experiment runs…….33

Fig. 2.17 Flow velocity versus radius point for the 0.5 inch pipe using 10 experiment runs..... 34

Fig. 2.18 The NMSE of calibrated flow using 4 experiment runs for the one inch pipe.. 37

Fig. 2.19 The NMSE of calibrated flow using 4 experiment runs for the half inch pipe. 37

Fig. 3.1 Bypass design using in the simulation..... 38

Fig. 3.2 Bypass Flowmeter 39

Fig. 3.3 Flowmeter Bypass Piping:1, 2, and 3 are the front valve, rear valve and bypass valve, respectively. 4 is the flowmeter. L≥10D and L≥5D are the lengths of the front and rear straight pipe segments, respectively. 42

Fig. 3.4 Operational diagram of the mass flow controller. 45

Fig. 4.1 Shear stress and normal stress. 52

Fig. 4.2 Infinitesimally small, moving fluid element. The forces are in *x* direction..... 52

Fig. 4.3 Energy fluxes with an infinitesimally small, moving fluid element in x-direction.

Fig.4.4 Flowmeter design 59

Fig.4.5 Mesh generated for 2D around the thermocouple 60

Fig.4.6 Mesh generated for3D around the thermocouple 62

Fig.4.7. 2D compare of different mesh in radial direction at centerline location 62

Fig.4.8 2D compare of different mesh in radial direction at TC1 location..... 63

Fig.4.9 Compare of mesh and the refined one for velocity at radial direction at TC1 location..... 63

Fig.4.10 Boundary conditions at simple pipe. 64

Fig.4.11 Heating pattern for transient time. 65
Fig.4.12 Contours of temperature in different times, 2D W/O TCs. 67
Fig.4.13Contours of velocity in steady state, 2D without TCs, *Q*=1GPM. 68
Fig.4.14 Plot of position v.s. velocity in steady state, 2D position of the first and second thermocouple..... 68
Fig.4.15. the temperature profile detected from locations 1 and 2. 69
Fig.4.16 The temperature profile detected from locations 1 and 2, Q= 1GPM. 69
Fig.4.17 Different point at the first thermocouple location (TC1). 70
Fig.4.18. Time delay calculation for different points at TC1 and TC2. The flowrate is 1 GPM. 71
Fig.4.19. Time delay calculation for different points at radial direction at the location of TC1 & TC2. The flowrate is 2 GPM. 71
Fig.4.20 Time delay comparison at flowrate range of 1 to 4 GPM as the reference flow. 72
Fig.4.21. The calculated flowrate over the reference flow, using the data in table 4.1 and 4.2..... 73
Fig.4.22 Named selections for boundaries. 74
Fig. 4.23 Example of mesh preview in the horizontal pipe (ISO View). 75
Fig. 4.24 Post processing comparison of different mesh size in bypass at position 7. 78
Fig. 4.25 velocity vectors colored by velocity magnitude (m/s)..... 79
Fig. 4.26 Velocity profile comparison of laminar flow (a) and turbulent flow (b)..... 79
Fig. 4.27 The effect of different diameter ratios 85
Fig. 4.28 The computed bypass flow rates versus main-pass flow rates for different entrance lengths. 88

Fig. 4.29 The computed by-pass flow rates versus main-pass flow rates for different length of the vertical arm in the bypass pipe. 89

Fig. 4.30 The ratio between the bypass flow and main-pass flow. 90

Fig. 4.31 Velocity plot in the centerline of the bypass. 91

Fig. 4.32 The relative deviation of the ratio between the by-pass flow and main-pass flow. 92

Fig. 4.33 The pressure along the main-pass pipe for velocity of 1 m/s for a pipe simulation and calculation. 94

Figure 4.35 Temperature distributions at different position of bypass. 96

Figure 4.36 Response time at different TC locations. 97

Fig 4.37 The time delay of two signals 1 second heater on and 6 second off 98

Fig 4.38 Linearity of bypass to mainline from table 4.11. 100

Fig 4.39 Error bars showing the errors at each points 101

Fig 4.40 Simulation geometry used for experiment. 102

Fig 4.41 Mesh using the inflation layer from the wall and calculate the first layer thickness. 102

CHAPTER 1

INTRODUCTION

In this project we are introducing a most promising method to measure the flow rate in harsh environment (high temperature, pressure, and corrosive ones). The existing technologies fail to operate reliably, since for long term operation corrosive environment degrades the performance of the transducer and it needs frequent re-calibration. Usually the non-intrusive flow meters are capable of working in corrosive environments. One of the examples is the ultrasonic flowmeters that in corrosion/erosion in the pipe inner surface produces significant variation of ultrasonic wave. In our method, the flow rate can be obtained by the cross-correlation calculation of flow temperatures recorded by two separate temperature sensors. But we should already know the cross-sectional area of the pipe that the liquid flows. The problem is in cross-correlation calculation wide peak or additional false peaks are generated. These problems can be solved by a new adaptive signal processing algorithm to estimate the impulse response function of the sensor system. So in this way the peak is much narrower and the additional peaks are reduced. The simulation is performed by using commercial computational fluid dynamic (CFD) software (ANSYS-FLUENT)

- *Existing technologies for flow rate measurement*

Flow measurement is a critical need in many industrial applications with variety of purposes such as monitoring, control and experimental works. There are two basic ways to measure the flow: One measures the amount of fluid that passes through the flowmeter during a time period like 100 liters per minute. The other way is measuring the totalized amount of fluid passes through flowmeter like 100 liters. The two components of the

flowmeters are transducer and transmitter. The fluid passes through the primary device is the sensed by the transducer, while a flow signal will be produced by the transmitter from the raw transducer signal.

Many flowmeter technologies have been developed for measuring of fluid flow including [1]: differential pressure flowmeters (primary element options, pitot tubes, variable area flowmeters), mechanical flowmeters (positive displacement, turbine, and other rotary flowmeters), electronic flowmeters (magnetic, vortex, and ultrasonic flowmeters), and mass flowmeters (Coriolis mass, thermal mass flowmeters, and hot-wire anemometers). In the following most of popular flow meters is briefly reviewed.

1.1 Differential Pressure

It is used for all liquids and gases that have low or medium viscosity, low solids content, and are compatible with the materials of construction. It measures flows of liquids and compressed gases. It is based on the orifice principle using the Bernoulli's equation by creating a pressure drop across the flowmeter in a pipe. By increasing the flow, more pressure drop creates.

Four different kinds of differential pressure flow meters are [3]:

- Orifice Plates
- Flow Nozzles
- Venturi Tubes
- Variable Area – Rotameters

-Orifice plates

The measurement is based on the difference in pressure from upstream to downstream side of a pipe which is partially obstructed. The advantages of this flowmeter are

cheapness and the application for any material. But the accuracy is poor for low flow rates.

-*Flow Nozzles*

Flow nozzles are suitable for gas flow in which the velocity increases by accelerating the gas through the nozzle, whereas the pressure and the gas density decrease. That helps to achieve a fixed, accurate, and repeatable gas flow rates without being affected by the downstream pressure. Again the nozzles are cheap and applicable in any materials.

-*Venturi Tube*

In this case the fluid flow rate is measured by a pressure difference which is generating by a reduction in the cross sectional flow area in the flow path. After that the flow passes through the pressure recovery area to be recovered up to 80%.

- *Variable Area / Rotameter*

It is the most common specified, purchased, and installed flowmeter in the world. Fluid flow moves the float upward against gravity and finds the equilibrium when area around float equals to the column flow of the fluid. The cross section area varies with the flow rate so that the higher flow path area is for the higher flow rate. The advantage is the ease of installation and operation because of the simple variable-area design. The disadvantage is that there may not be enough head room for the rotameter to be installed in vertical position. Also for the larger rotameter the cost would be higher.

1.2 Pitot Tubes

The pitot tubes used to measure the fluid for the air applications like ventilation and HVAC systems, and the speed measurement in airplanes [2]. It converts the kinetic energy of the fluid to the potential energy. It is restricted to point measuring. Pitot Tubes are suitable for high temperatures and a wide range of pressures. A pitot tube is

measuring two pressures. The static pressure which is the operating pressure and it is measured at right angles to the direction of the flow. Next is the total impact pressure which is the sum of the static and kinetic pressures and it will be measured at the opening facing the oncoming flow stream. Then the point velocity will be measured and multiplied by the cross sectional area to obtain the flow rate [6].

$$V_P = \frac{C_P\left(\sqrt{P_T - P}\right)}{D} \qquad (1.1)$$

where V_P : is the point velocity, C is a dimensional constant, D is density, P_T : is the total pressure, P is the static pressure.

1.3 Velocity Flowmeter

The flow is measuring by picking some points in the flow and by integration the flow speed over the flow area.

1.4 Calorimetric

It is used for measure and monitor of small and average flows of air in pipes such as flow monitoring of air and gases, in air conditioning systems, and in extraction systems. It is based on calorimetric principle [3]. By applying the voltage, a thermistor integrated in the sensor is heated to a medium temperature. The velocity and the rate of flow equalize the temperature and the resistance of the sensor is reduced. The flow velocity is determined by measuring the resistance. In other words, the two temperature sensors are insulated from each other but in close contacts with the fluid so that one of the two sensors is heated and by measuring the cooling effect of the fluid the flowrate will be monitored. The most accuracy of this flowmeter is at the lower flowrates.

1.5 Positive Displacement Flowmeters

There are two gears that rotate to measure precise volumes of liquid that pass through the flow meter .We can count the number of rotations of the rotor by using intergral electronic pulse transmitter and convert it to volume and flowrate. It is used for measuring of viscous liquids and thicker fluids such as resins, polyurethanes, adhesives, paints, and various petrochemicals. PD meters do not require a power supply for their operation and also they don't require straight pipe for their installation. The fluid must be clean so by using the filter we can remove the particles. Most widely used for household water meters [6].

1.6 Turbine

It is used in the corrosive and abrasive fluids such as oil field waterflood project pipelies, in-situ mining operation offshore facilities and plant locations. The main advantages are the simplicity to install and operation in any orientation (horizontal to vertical). The rate of spin in the turbine once the flow reach to it through a pipe is measured to calculate the flow.

1.7 The magnetic flowmeter

They place the magnets above and below the pipe to produce the magnetic flux. Because of the movement of conductive fluid a potential is induced into the flow stream. The fluid flow is proportional with the produced voltage between these two electrodes.

The advantages of this method include no pressure drop, working in laminar, turbulent, and transitional flow, and they have no moving parts.

The disadvantages are first the fluid needs to be conductive. Also the pipe must be grounded because of utilizing magnetic and electric fields. Also using graphite is not recommended here since it causes erroneous signals. [6]

1.8 Electromagnetic flowmeters

It provides accurate measurement in water cycle and process applications. It includes the improvement to the magnetic distribution elements that performs the accurate operation throughout the flow regimes [2]. According to the Faraday's law a voltage would be induced if a conductor moves through a magnetic field. Here the liquid is as a conductor and outside the flow tube there is an energized coil which creates the magnetic field. The produced voltage is proportional to the flow rate. The voltage is detected by the two electrodes mounted in the pipe wall and the voltage will be measured by a secondary element. These flowmeters are suitable for corrosive liquids. But they consume high power and should be used for conductive fluids like water.

1.9 Mass flowmeters

It measures the mass flow rate directly in three ways. First the mass flow rate directly calculated from the outputs of a volumetric flowmeter and a densitometer. This method is not efficient because of the error and slow response time. Second method is by using the angular momentum. The rotary motion accelerates the fluid to a constant angular velocity. The flow mass was obtained from the resulting spring torsion which is exposed to angular momentum. This method was in use of measuring the aircraft fuel but the problem was complexity and high maintenance cost. The third method is using two d/p transmitters with different elevations on the lower part of the atmospheric tank. We can measure the pressure differential of these different levels and from that the density of the material in the tank. This method is suitable for measuring the total mass flow of the slurries.

1.10 Thermal Mass Flowmeters

It is designed for measuring gas flow rates in ranges from 0-10 sccm to 0-500 slm. The outstanding performance and unsurpassed value makes it accurate for a wide temperature and pressure range for a response time of two seconds. Flow stream conducts heat from the sensing element which is isolated from the fluid flow path. The temperature difference can be calculated to the mass flow rate [3].

1.11 Coriolis Flowmeter

Coriolis flowmeters are based on the direct mass measurement which is not sensitive to any changes in pressure, temperature, viscosity, and density. By using the Coriolis Effect we can measure flowrate. The flow runs through a U-shaped tube which is causing angular harmonic oscillation and additional vibration component from the Coriolis forces which causes a phase shift that could be measured by sensors.

1.12 Ultrasonic flowmeters

It is suitable for high pressure, sanitary environments, and corrosive fluids where material compatibility is an issue. These meters are installed on the outside of the pipe. They work by either the ultrasonic transit time detection or Doppler Effect. The size of the pipe line can be 3/8 to 12-inch. They are suggested for the pipe lines that we prefer not to break the line. In ultrasonic Doppler flowmeter, the frequency of the reflected signal is modified by the velocity and direction of the fluid flow. The increase or decrease in the frequency of the returning signal depends on the direction of the fluid toward or away from a transducer [3].

This type of flowmeter uses ultrasound to calculate volume of flow and measure the velocity of the fluid. Unlike the mechanical flow meters, they don't use the moving part.

The three different types of ultrasonic flow meters are intrusive, non-intrusive, and open channel flowmeter. In the intrusive ones the transmission flowmeters are distinguished into in-line. While the non-intrusive or the clamp-on type does not touch the fluid.

Totally ultrasonic flowmeters are measuring the difference of the transit time which is propagating in the reverse direction of the flow. The two transit time difference are showing the delay, the distance between receiving and transmitting transducers is (L), the inclination angle α, and the velocity is obtained by,

$$v = \frac{L}{2\sin(\alpha)} \frac{t_{up} - t_{down}}{t_{up} t_{down}} \qquad (1.2)$$

where t_{up} and t_{down} are upstream and downstream transit time.

The second method in ultrasonic flowmeters is based on the Doppler shift. The reflection of an ultrasonic beam, reverse the direction of beam and repeating the measurement is using in this method. This kind of flow meter operates similarly to the radar speed traps used in the road. [4]

Both Doppler and transit time ultrasonic meters are expensive. Specially, they are not recommended in sludge, mixed liquor, carbon sludge. Another disadvantage for Doppler is that they do work well for low velocities, and it is not a good choice for clean liquids.

The advantages of Doppler flowmeter are that it is designed in non-intrusive and used on the surface of the pipe. Also it has easy installation, zero pressure drops, and it works in corrosive fluids. However, when the flow is clean and there is no wave reflecting particles, this flowmeter may fail to measure the flowrate.

Another problem with ultrasonic flowmetes is corrosion/erosion problem in the inner side of wall surface. The propagated waves may deviate due to the wall roughness changes caused by corrosion. Therefore, the ultrasonic flowmeter requires frequently calibration due to the inner surface degradation [5].

1.13 The vortex flow meter

It works for measuring both liquid and gas. By using the shedder bar in the path of the fluid, the vortices are created. Then, a sensor measures the frequency of the vortex shedding. The frequency is proportional to the fluid velocity [2].

In this design there is a bluff body or bodies that placed in the fluid stream. Just behind that there is a pressure transducer which measures the pressure and velocity fluctuations. These fluctuations are proportional to the flowrate. In other words, as fluid moves around the baffles, vortices move and form downstream. The frequency of the vortices is directly proportional to flow rates.

The advantages of this method are that it can be used in liquids, gases, and steam. It is available for a wide variety of temperature range and different pipe size. They have also low cost of installation.

The disadvantages are: first, these are not a good choice for a low velocity fluid. There are some constraints for the pipe diameter and the length.

In the nuclear application with high temperature application the pressure sensors which are used in this flow meter the high temperature is a barrier for this type of sensor. In addition, material degradation of blunt body due to corrosion/erosion will also introduce significant errors in the measurements [6].

Some vertex shedding designs can be used for high flow velocities by using water as fluid [7].

1.14 Paddlewheel

It is designed for using water and other low viscosity liquids. The components are PVC body and lithium battery powered LCD display [2]. The installation affects the performance. They can be installed horizontally or vertically. They can use battery instead of electrical connections. They have the flexibility such as batch process control, analog output signals and remote readouts also a power source supplied by an AC/DC plug-in style transformer. The disadvantage is that they cannot measure very dirty fluid, or liquids with rocks or pebbles that could break or damage the paddle or axle. The pipe should be in straight length and without corners the performance is poor.

1.15 Float Type

It is designed for minimum pressure loss at high flow rates with extremely low flow switching points [2].

1.16 Open Channel Flowmeters

In open channel flowmeters the height of the liquid would be measured as it passes over an obstruction as a flume or weir in the channel [3].

In nuclear industry, flow measurements are avoided for highly active process. Therefore, they are using the alternative methods for example by using constant volume feeders and the rate of charge of vessel level will be monitored. Table 1 shows the failure rate of commonly used flowmeters in the nuclear industry.

Table1.1 Flowmeter's reliability in the nuclear industry.

Flowmeter	Failure rate (fpa)
Magnetic	0.60
Variable aria, transmitting	0.85
Variable aria, not-transmitting	0.04
Turbine	0.20
Flowswitch	1.10
Pitot tube (vent duct)	0.002

Since the produced voltage by the meter is a function of dimension of pipe, electric conductivities of the pipe wall, liquid and contact resistance at the liquid wall boundary, any changes in the inner diameter, or contact resistance due to corrosion/erosion leads to measurement errors.

This thesis investigates the practical problems with the correlated thermal signals based flowmeters. The main contribution of this work is to address the limitation of this flowmeter when the flow is high or the pipe is big and propose a solution to overcome these limitations.

Chapter one presents a brief discussion about the existing flowmeters which are utilized in corrosive environments. The advantages and disadvantages of these flowmetes are also mentioned.

Chapter two introduces the theory of correlated thermal signals based flowmeter and its practical problems in the harsh environments. In this chapter, the signal processing solutions as well as calibration procedure is presented.

Chapter 3 gives a theoretical study on the bypass flow measurement system. In this chapter, problems with the theoretical analysis of these systems are discussed.

Chapter 4 presents the design and simulation of the proposed flowmeter. This chapter investigates several design parameters such as entrance length, pipe angel, ratio of bypass

and mainpass pipe sizes and the distance between their centerlines and their effects on the performance of the flowmeter.

Finally, conclusions and some future directions for further study and research will be discussed.

CHAPTER 2

CORRELATED THERMAL SIGNALS BASED FLOWMETER

We develop a flowmeter to be used in a harsh environment such as a nuclear power plant/reactor which uses two thermal signals recorded from two temperature sensor placed certain distance apart along the pipe. By assuming these signals are correlated to each other, the time delay between these signals is used to calculate the flow rate. This delay can be obtained from some signal processing methods which are discussed in this chapter.

2.1. Time delay estimation methods

Assume that the change of characteristics of the flow profile, provided by the thermocouples within a certain distance is not changed very much (Fig. 2.1) such that the downstream and the upstream thermal signals are correlated with each other. In practice this assumption may not be valid. We use a heater in the system to generate heat pulses so that strong correlated thermal signals from the thermocouples can be achieved.

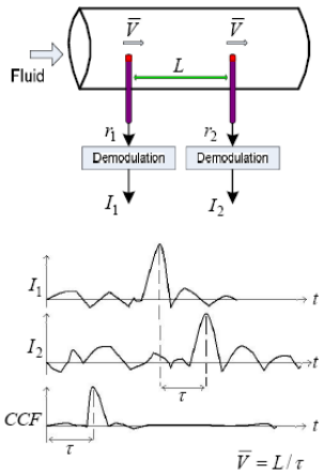

Fig. 2.1 Transit time configuration.

In this case, the upstream thermocouple records a temperature signal $L/\overline{V}$ seconds earlier than the downstream one, where L is the distance between the two sensors and $\overline{V}$

is the average flow speed. Therefore, by estimating the time delay, τ, the flow speed can be obtained by [8],

$$\overline{V} = L/\tau \qquad (2.1)$$

There have been several time delay estimation tmethods available in the literatures. In the following a few of them are introduced.

A. Cross-correlation Method

The key idea of this method is that the cross correlation function of two correlated signals has a peak at the delay point which gives an indication of the time delay between the two thermocouples [9]. The cross correlation of $i_1(t)$ at time *t* and $i_2(t)$ at time $t-\theta$ is obtained from the following equation [9],

$$CCF(\theta)=\int_{-\infty}^{+\infty} i_1(t) i_2(t-\theta)dt \qquad (2.2)$$

If assume that $i_2(t)$ is a copy of $i_1(t)$ delayed by τ, one has,

$$CCF(\theta)=\int i_1(t) i_2(t-\theta-\tau)dt = ACF(\theta-\tau) \qquad (2.3)$$

where *ACF* is the autocorrelation function of $i_1(t)$.

Since the autocorrelation function (ACF) always has its maximum at zero, the cross correlation function (CCF), reaches its maximum after τ [9]. In other words, the amount of time that CCF reaches its peak is the time delay, τ.

As shown above, in theory the peak of cross correlation function gives the time delay related to the corresponding flowrate. But in practice, as it was observed from the lab experiments, the cross correlation calculation generate a wide peak or a weak peak which may not be distinguishable from the one caused by background noise or fluctuation [8], [9](Fig. 2.2). In either case, the accuracy of this technique is degraded. This problem can

be alleviated by the generalized cross correlation method [10]. However, this method requires *a priori* knowledge of the power spectra of both the signal and the noise, or it can give poor performance if the estimated spectra do not match well with the true spectra [8], [11]. In [8] the following methods have been proposed and tested experimentally using an in-house developed test apparatus.

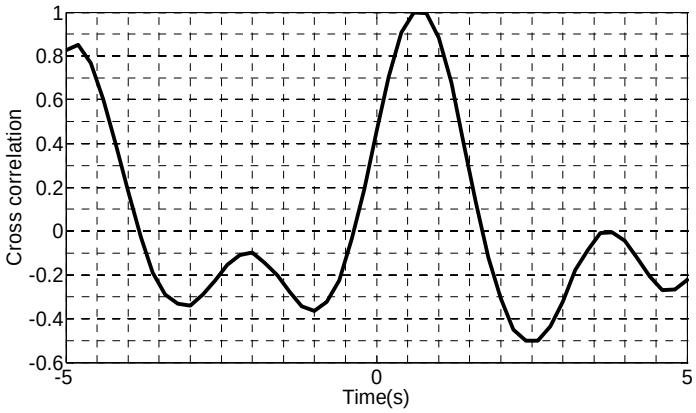

Fig. 2.2 Cross correlation of thermal signals recorded by thermocouples

B. Impulse response estimation using transfer function calculation

The system is modeled as a single input single output system (Fig. 2.3). The signals $i_1(t)$ and $i_2(t)$ are considered as input and output of the system, and $h(t)$ is its impulse response function.

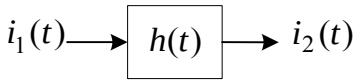

Fig. 2.3. System model for basic transfer function estimation.

If the applied signal at the first thermocouple is an impulse function, $i_1(t) = \delta(t)$, the CCF of $i_1(t)$ and $i_2(t)$ will be equal to the impulse response function, $h(t)$ [9]. This imply that the maximum peak of $h(t)$ corresponds to the time delay, τ. Therefore, estimation of τ boils down to estimating $h(t)$.

To obtain $h(t)$, first the transfer function of the system is obtained and then by using Fourier transformation $h(t)$ is obtained.

To obtain an unbiased estimation of the transfer function, the measured signals $i_1(t)$ and $i_2(t)$ are corrupted by added white noise (Fig. 2.4). The transfer function, $H(j\omega)$, is obtained by [9],

$$\frac{CPSD_{12}}{APSD_1} = \frac{H}{1+\frac{|W_1|^2}{|I_b|^2}} \tag{2.4}$$

where $CPSD_{12}$ is the cross-power spectral density of I_1 and I_2, and $APSD_1$ is the auto power spectral density of I_1. In Eq. (2.4), we can assume that $\frac{|W_1|^2}{|I_b|^2}$ is much less than 1, therefore by ignoring this term the above equation is simplified to,

$$\hat{H} = \frac{CPSD_{12}}{APSD_1} \tag{2.5}$$

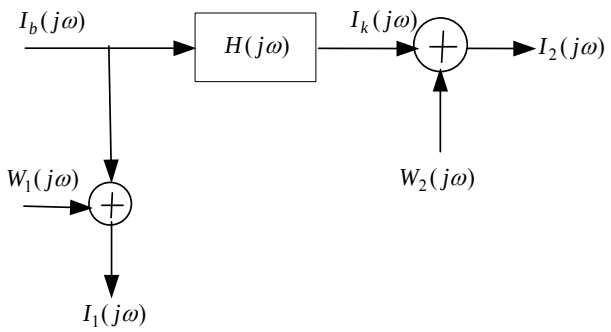

Fig. 2.4. Transfer function estimation for noisy input and output.

A summary of this method is given as,

1) Calculate the frequency representations of $ACF(t)$ and $CCF(t)$ to get $APSD_1$ and $CPSD_{12}$, respectively.

2) Use Eq. (2.5) to get $H(j\omega)$ and convert it back to $h(t)$ by the inverse Fourier transform.

3) Detect the peak of $h(t)$ to obtain τ .

As this method experimentally verified in-house developed test apparatus, the results showed that this method produces multiple peaks with same or similar height (Fig. 2.5).

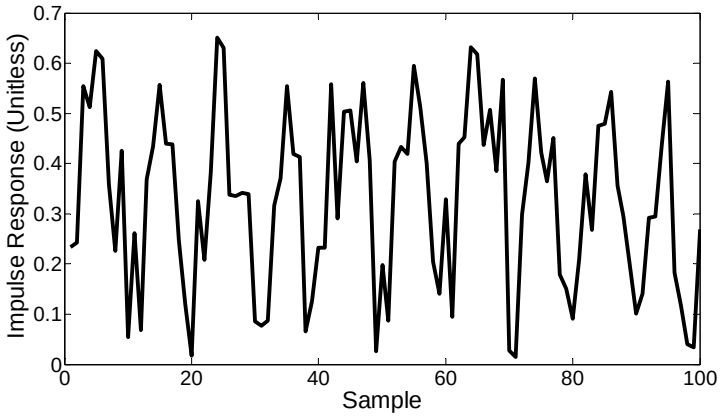

Fig. 2.5 Impulse response of the system obtained from transfer function estimation.

C. Auto-Adaptive Impulse Response Function estimation (AAIRF)

From Fig. 2.5 we can see that in the estimated impulse response function using the conventional transfer function, the real delay point cannot be detected and also it generates multiple peaks. To overcome this problem, the Auto-Adaptive Impulse Response Function estimation (AAIRF) method has been proposed in [8]. In this method, a windowed version of cross correlation and autocorrelation functions is used for transfer function estimation. In this case, only the points around the peak (between two adjacent valley points around the peak) are considered. As shown below this method gives a significantly narrower and stronger peak. This method has been also experimentally verified in [8].

Assume that the autocorrelation function, $ACF(t)$ and cross correlation function $CCF(t)$ have multiple peaks (Figs. 2.6.a and 2.6.b). Let $\psi_{11}(t)$ and $\psi_{12}(t)$ be the windowed versions of $ACF(t)$ and $CCF(t)$, respectively, (Figs. 2.7.a and 2.7.b). $\psi_{12}(t)$ can be written in terms of $\psi_{11}(t)$ as follows,

$$\psi_{12}(t) = \psi_{11}(t-\tau) + \delta\psi_{11}(t-\tau) \tag{2.6}$$

Let $\tilde{H}(j\omega)$ be the Fourier transform of the system for the windowed correlation function. By transforming Eq. (2.6) to frequency domain, one may get,

$$\begin{aligned}\tilde{H}(j\omega) &= \frac{F\left(\psi_{12}(t)\right)}{F\left(\psi_{11}(t)\right)} = \frac{F\left(\psi_{11}(t-\tau) + \delta\psi_{11}(t-\tau)\right)}{F\left(\psi_{11}\right)} \\ &= \frac{\Psi_{11}(j\omega)}{\Psi_{11}(j\omega)} e^{-j\omega\tau} + \frac{\Delta\Psi_{11}(j\omega)}{\Psi_{11}(j\omega)} e^{-j\omega\tau} = \left(1 + \frac{\Delta\Psi_{11}(j\omega)}{\Psi_{11}(j\omega)}\right) e^{-j\omega\tau} \\ &= \left(1 + \left|\frac{\Delta\Psi_{11}(j\omega)}{\Psi_{11}(j\omega)}\right| e^{j(\phi_{\Delta\Psi_{11}} - \phi_{\Psi_{11}})}\right) e^{-j\omega\tau}\end{aligned} \tag{2.7}$$

Since $\psi_{11}(t-\tau)$ and $\delta\psi_{11}(t-\tau)$ have almost the smae phase and the amplitude of $\delta\psi_{11}(t)$ is much smaller than that of $\psi_{11}(t)$, Eq. (2.7) gives the following approximation for $\tilde{H}(j\omega)$,

$$\tilde{H}(j\omega) \cong e^{-j\omega\tau} \tag{2.8}$$

Therefore,

$$\tilde{h}(t) \cong \delta(t-\tau) \tag{2.9}$$

Eq. (2.9) indicates that the impulse response function $\tilde{h}(t)$ is theoretically close to the impulse function, meaning that it has one extremely narrow and strong peak at point τ.

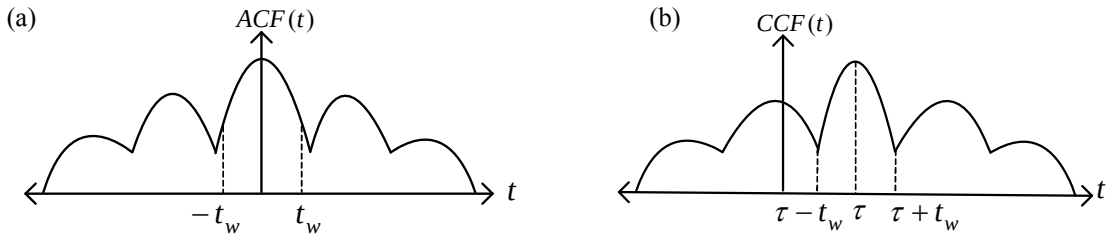

Fig. 2.6 (a): The autocorrelation function of $i_1(t)$, (b): The cross correlation function of $i_1(t)$ and $i_2(t)$.

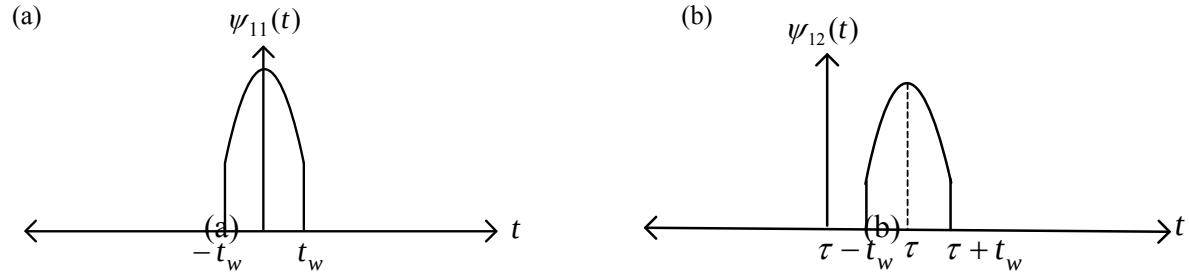

Fig. 2.7 (a): The windowed version of the autocorrelation function of $i_1(t)$, (b): The windowed version of cross correlation function of $i_1(t)$ and $i_2(t)$.

D. Moving Average Filter based Cross correlation Function method

The accuracy of AAIRF can be further improved if a moving-average-filter is used for calculation of the cross correlation function. In the AAIRF, since the accuracy of detected peak is dependent on the peak point deviation in cross correlation function, the variation of detected point can be large. To alleviate this problem, another method called Moving Average Filter based Cross Correlation Function (MAFCCF) [8],[12]. In this method, the raw data are simply averaged using a moving average filter, then the filtered data is fed to the autocorrelation and cross correlation for next step of calculation. This function can be expressed as,

$$R_{i_1 i_2}(rT_s) = \frac{1}{T}\sum_{k=1}^{N-1} i_{1M}(kT_s) i_{2M}((k-r)T_s) \qquad (2.10)$$

where

$$i_{1M}(kT_s) = \frac{1}{M}\sum_{l=0}^{M-1} i_1((k-l)T_s) \tag{2.11}$$

$$i_{2M}((k-r)T_s) = \frac{1}{M}\sum_{l=0}^{M-1} i_1((k-r-l)T_s) \tag{2.12}$$

where r is the number of sampled-data in CCF, k is the number of sampled-data in signals $i_1(t)$ and $i_2(t)$, T_s is the sampling period, and M is the length of moving average filter.

2.2. Accuracy and error analysis

The performance of the cross correlation based time delay estimator depends on the accuracy of the peak detection in the cross correlation function. The other parameter that may effect on the accuracy of this method include the bandwidth of measured signals, number of samples, background noise, waveform sampling, waveform quantization and distortion of the trace pattern in the flow between the thermocouples (and TC responses), filter mismatch, pipe diameter variations and differences between the geometrical and effective thermocouple spacing [13]. In [8], it was reported that the system error is very small that can be ignored compared to the time delay estimation error and the error due to the sampling frequency.

- Error due to time delay estimation method (cross-correlation function)

As shown in [13] the normalized mean square error in cross correlation function and the variance of time delay estimates τ_* are given by,

$$e^2(\tau)=\frac{1}{2BT}\left[1+\frac{1}{\rho^2 xy(\tau)}\left(1+\frac{1-q}{f_sT}\right)^2\right] \quad (2.13)$$

$$\mathrm{var}(\tau^*)=\frac{0.038}{TB^3}\left\{\left[\frac{1}{\rho^2 xy(\tau^*)}\left(1+\frac{1-q}{f_sT}\right)^2\right]-1\right\} \quad (2.14)$$

$$\rho^2 xy(\tau)=\frac{CCF^2(\tau)}{ACF_1(0)ACF_2(0)} \quad (2.15)$$

where B is the bandwidth of measured signals, T is the length of measured signals, ACF_1 and ACF_2 are the respective autocorrelation functions of $i_1(t)$ and the cross correlation of $i_1(t)$ and $i_2(t)$, f_s is the sampling frequency, $\rho^2{}_{xy}(\tau)$ is the normalized cross correlation, and q is the correlation coefficient between the instantaneous flow event. This correlation coefficient for the measured signals is given by [13],

$$q=1-\frac{f_sT}{SNR} \quad (2.16)$$

where SNR is the mean square signal to noise ratio defined by [6],

$$SNR=\frac{\rho^2{}_{xy}(\tau)}{1-\rho_{xy}(\tau)} \quad (2.17)$$

Since the MACCF method increases the SNR, according to Eqs. (2.13) and (2.16), the normalized mean square error of time delay estimates in MACCF will be smaller than that in CCF method.

- Error due to the sampling frequency

As we deal with discreet signals in the measurement, the cross correlation function is calculated point by point (Fig. 2.8). This function gives only the position of peak and the time delay is obtained by dividing the detected number where the peak occurred by

the sampling frequency. As shown below, the sampling frequency must be large enough to reduce the error in the calculation of the time delay.

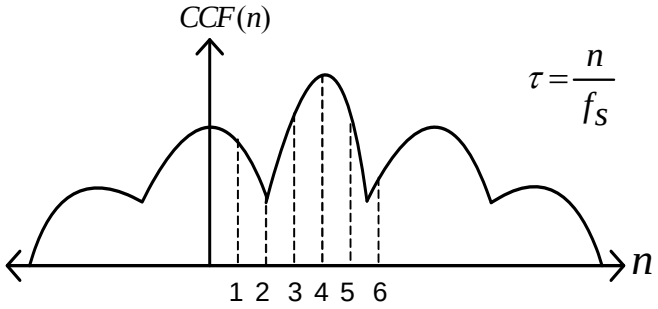

Fig. 2.8 Point by point cross-correlation

The flow rate can be expressed as,

$$Q = VA = \frac{L}{\tau}\frac{\pi D^2}{4} \tag{2.18}$$

where Q is the flow rate, V is the flow velocity, A is the cross-sectional area of the pipe, L is the distance between two thermocouples, τ is the time delay between the two thermal signals, and D is the internal diameter of pipe.

Substituting $\tau = \frac{\theta}{f_s}$, where θ is the sample offset delay between two thermal signals, into Eq. (2.18) yields,

$$Q = \frac{K}{\tau} = K\frac{f_s}{\theta} \tag{2.19}$$

Therefore,

$$\frac{\Delta\tau}{\Delta f_s} = -\frac{\theta}{{f_s}^2} \tag{2.20}$$

From Eq. (19) and (20) one may get,

$$\frac{\Delta\tau}{\Delta f_s} = -\frac{K}{Qf_s} \tag{2.21}$$

By combining $\frac{\Delta Q}{\Delta \tau} = -\frac{K}{\tau^2}$ and Eqs. (2.19) and (2.21), one may find,

$$\frac{\Delta Q}{\Delta f_s} = \frac{Q}{f_s} \qquad (2.22)$$

As seen from the above equation, the deviation of measured flow rate deviation with respect to the sampling frequency is inversely proportional to the sampling frequency.

2.3. Verification of time delay estimation methods

In [8] the considered time delay estimation methods have been verified experimentally using a developed water-based test apparatus in the laboratory (Fig. 2.9). This system consists of a water tank, a water pump, an electrical heater, a data acquisition system, and two thermocouples with spacing of 50 *cm* along the pipe with diameter of 21 *mm*. The thermocouple spacing was chosen longer than three times the pipe diameter so that the meter can measure wider time delay span. The tips of the thermocouples are placed at the center of pipe.

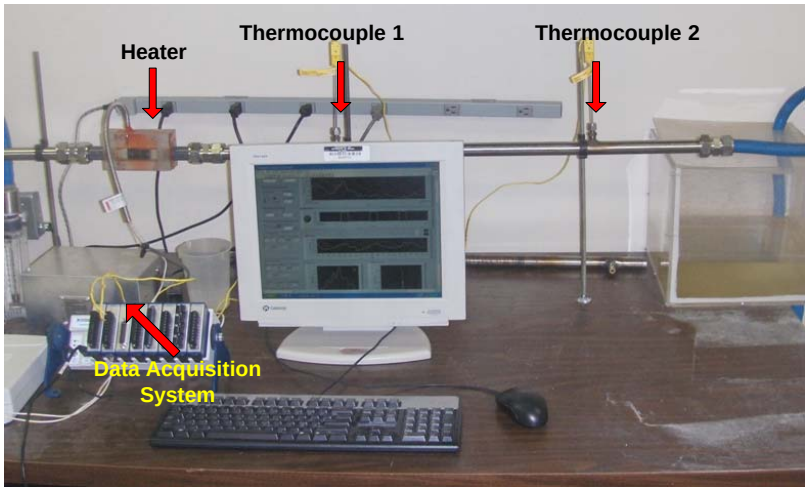

Fig. 2.9 A water-based test apparatus.

The temperature data has been gathered over flow range of 0.5 - 5 GPM with periodic heating and random heating patterns.

- *Experiments using Periodic Heating*

To create a strong thermal signal in the system, a heater has been employed. To examine the effect of the period and the duty cycle of the heating signal on the accuracy of the time delay estimation, four different heating patterns were tested (Table 2.1).

Table 2.1 Periodic heating patterns

Heating Pattern	On Heating Time (s)	Off Heating Time (s)	Duty Cycle	Period (s)
1	1	4	20%	5
2	2	3	40%	5
3	1	7	12.5%	8
4	2	6	25%	8

In this set of experiments, it was found that the period of the heating signal must be sufficiently higher than the time delay between the two thermal signals. Otherwise, the cross correlation function tends to generate multiple peaks with same height and/or negative peaks. For example, when the estimated time delay is 4.2 seconds, and the heating patterns 1 and 2 with a period of 5 seconds are applied, the side-lobe peaks have the same height as the main peak.

It was also found that the duty cycle has no noticeable effect on the time delay estimation.

- *Experiments using Random Heating:* Sampling Window Size

In the second set of experiments, to create temperature fluctuations in the water flow the heater was randomly turned on/off. In this experiment, the effect of the sampling window size which varied from1 to 400 samples on the accuracy of the time delay

estimation was evaluated. The results are plotted in Fig. 2.10. As seem from this figure, the size of the sampling window has significant impacts on the accuracy of the time delay estimation. Both CCF and the baseline AAIRF methods give nearly identical variance of estimated time delay. But when the moving average filter is used, one can see from Fig. 2.10 that the variance is reduced, indicating improved accuracy. It can be found that the longer of the moving average filter, the less of the variance of estimated time delay.

It is see that when the size of the sampling window is below 270 samples, the variance is high. When it exceeds 270 samples, the accuracy is very small improved. When the sample size is 400 samples and goes higher, no improvement is made which means that the variance is largely due to the system errors Therefore, the sampling window size is of 400 samples is good setting for the experiments.

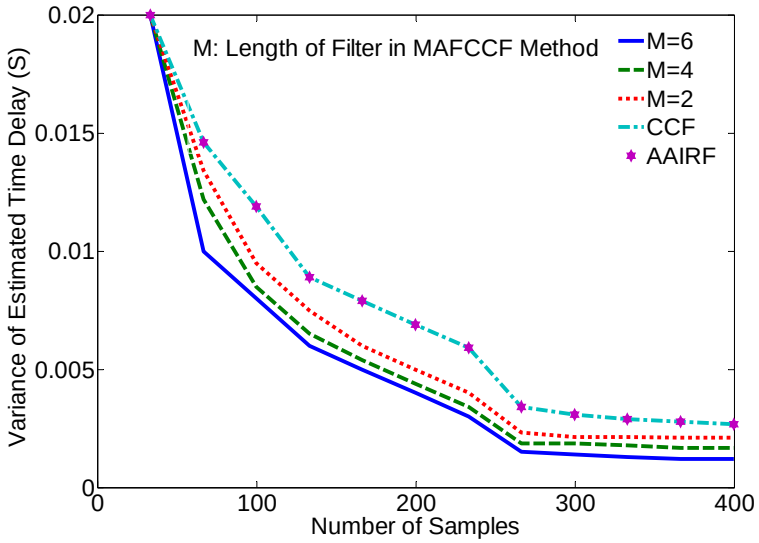

Fig. 2.10. Variance of estimated time delay for considered methods for flow rate of 2 gpm, sampling frequency of 10 Hz and for five different configurations: (i) CCF, (ii) AAIRF, (iii) MAFCCF with its moving average filter assuming a length of 2, (iv) MAFCCF with its moving average filter assuming a length of 4, and (v) MAFCCF with its moving average filter assuming a length of 6.

- Experiments using Random Heating: Sampling Frequency

In the third set of experiments, the effect of the sampling frequency on the accuracy of the time delay estimation was evaluated. In these experiments, the number of samples was set to 400 samples, and the sampling frequency varied from 1 to 40 Hz. Fig. 2.11 illustrates the results of the sampling frequency (Hz) vs. deviation of calculated flow rate (gpm). As seen the results agree well with the theoretical predications by Eq. (2.22). For all three flow rates, for the sampling frequency less than 10 Hz, significant deviation has been observed. Also, when the sampling frequency exceeds 10 Hz, the deviation of flow rate does not change significantly. Therefore, in practice, the sampling frequency was set to 10 Hz.

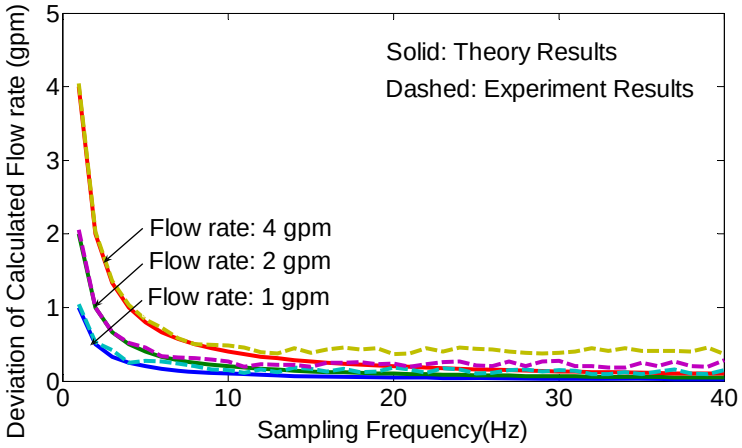

Fig. 2.11. Calculated flow rate deviation with respect to sampling frequency.

To compare the accuracy of the time delay estimation methods, including CCF, the baseline AAIF, and the MAFCCF with its moving average filter assuming a length of 6 two metrics were used: (i) the variance of time delay estimates, which is given in Eq. (2.14), and (ii) the Full Width at Half Maximum (FWHM), defined as peak height divided by its width (Fig. 2.12). The results are summarized in Table 2.2. Also, these three methods are compared in terms of their computation efficiency given in CPU time.

From Table 2.2, it is seen that in terms of FWHM, the AAIF outperforms the other two but at the cost of computation time. But this method has the same deviation of estimated time delay as the CCF does. MAFCCF on the other hand, has the least deviation of estimated time delay. In terms of CPU time, for the same variance of estimated time delay of 0.005 seconds, the CCF and AAIF methods require longer CPU time than MAFCCF method which means that the MAFCCF method requires fewer samples to achieve a certain level of accuracy. As a result, concerning both accuracy and CPU time, the MAFCCF has better performance over the other methods.

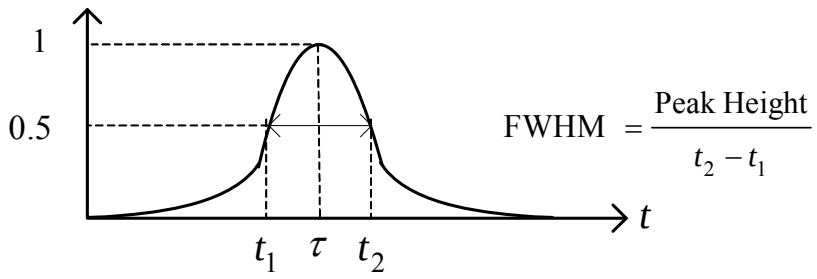

Fig. 2.12 The full width at half maximum representation.

Table 2.2 FWHM and CPU time comparison of the methods with the same variance of estimated time delay of 0.005 seconds

Methods	FWHM	Normalized CPU Time
CCF	0.035	1
AAIF	1.653	1.12
MAFCCF (M=6)	0.042	0.45

2.4. Measurement and calibration of correlated thermal signals-based flowmeter

It is reported in [14] that in practice, the calculated flowrates using the proposed time delay estimations in [8] are not in good agreement with readings from a standard flowmeter. To adjust the calculated flow, in [14], the calibration process with measurements obtained from lab experiments was performed. It was observed a nearly

linear relationship between the readings from the standard flowmeter and those from our flowmeter for flowrates ranging from 0.5- 3 gpm (gallon per minute).

- Flow velocity profile and flowrate calculation

The flow profile across a pipe can be predicted by an approximate curve-fit as given in [15] (Fig. 2.13),

$$V(r) = \begin{cases} V_C\left[1-(2r/D)^2\right], & \text{Laminar} \\ V_C\left[1-(2r/D)\right]^{1/n}, & \text{Turbulent} \end{cases} \qquad (2.23)$$

where $V(r)$ is the flow velocity at radial position r, D is the pipe diameter, V_C is the velocity at the center of the pipe, and n is a constant number which is related to the Reynolds number. For example, the corresponding Reynolds number for the flowrate range between 0.5 and 3 gallon per minute is equal to 6.6.

The flowrate can be derived from the velocity by,

$$Q = K\bar{V}A \qquad (2.24)$$

where Q is the flowrate, K is the calibration factor and A is the cross-sectional area of the pipe.

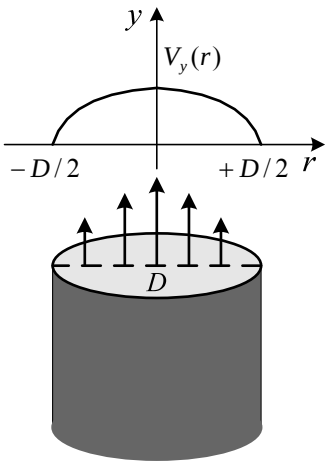

Fig. 2.13 The cross-section view of pipe showing the flow velocity distribution.

- *Flowrate Resolution vs. Response Time of Thermocouple*

The response time of thermocouples (TC) has effect on the flow range and resolution. Because the flowrate is obtained from the time delay between the thermal signals. Let δ and t_r denote the TC resolution and the rise time of the TC signal, respectively. It is simply shown that that the sampling frequency can be found by (Fig. 2.14) [14],

$$f_s \cong \frac{\Delta T}{t_r \delta} \tag{2.25}$$

where ΔT is the temperature change from 10% to 90% of the final value.

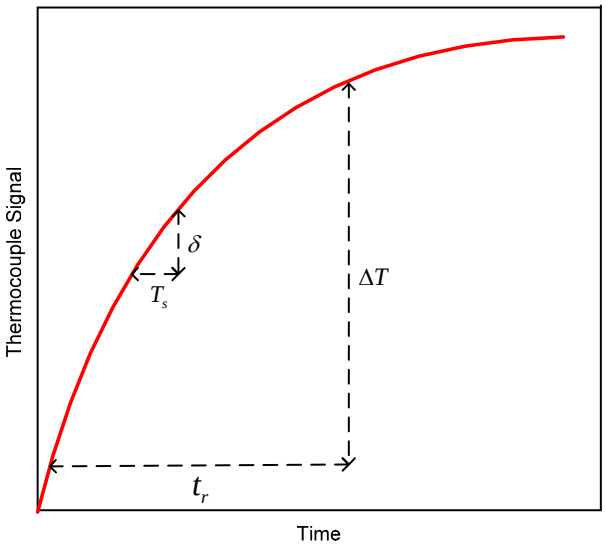

Fig. 2.14. Rising edge of the TC signal.

In [14], by experiments it was observed that the highest frequency contained within the thermal signal is around one Hertz. Therefore, based on the Nyquist rate theorem, the minimum theoretical sampling frequency required to avoid aliasing, is 2 Hertz. However, using (2.25) and the experiments data, $\Delta T = 0.4\,^0C$, $\delta = 0.1\,^0C$ and $t_r = 1s$, the sampling frequency will be 4 Hz. Therefore, in this project we set this parameter to 4 Hz.

In this flowrate calculation method, all the possible detected time delays will fall into the following set,

$$\tau\ (\text{second}) = \left\{ \frac{n}{f_s} = \frac{n}{4}, n = 1,2,... \right\} \tag{2.26}$$

Therefore, the flowrate for sampling frequency of f_s Hz will be,

$$Q = \frac{\pi D^2 L}{4} \frac{f_s}{n} \tag{2.27}$$

where L is the thermocouple spacing and D is the internal diameter of the pipe.

- *Deviation of Calculated Flow Velocity and Flowrate*

If we assume that the error $\Delta\tau$ due to time delay estimation leads to a deviation ΔQ in the calculated flowrate, it can be shown that,

$$\left|\frac{\Delta Q}{\Delta \tau}\right| = 4\frac{Q^2}{\pi D^2 L} \tag{2.28}$$

- *Calibration factor estimation*

Since the measured flow is based on the temperature change which is very small as a fraction of 1 degree it is assumed that it does not have any influence on the physical system dimensions such as the pipe diameter or thermocouple spacing. Also, since the roughness of the pipe wall does not affect the temperature profile, the calibration factor shall not be sensitive to roughness.

Therefore, the single factor that is considered in calibration factor estimation is the measurement error due to either background noise or the time delay estimation technique. The following empirical equation that relates the detected time delay to the reference flow is considered for calibration factor estimation,

$$\tau_i = k_0 + \frac{k_1}{Q_i} + \varepsilon_i \tag{2.29}$$

where k_0 and k_1 are the calibration coefficients which have to be estimated through calibration operation, and ε is the error in the measured time delay data.

The linear regression model is applied to the observation data for error minimization and the MSE criterion is used to fit this model [16]. That is,

$$\mathrm{MSE}(\tau_i, Q_i) = \frac{1}{n}\sum_{i=1}^{n}\left(k_0 + \frac{k_1}{Q_i} - \tau_i\right)^2 \tag{2.30}$$

where *n* is the number of calibration points.

This leads to the following equations [17],

$$[k] = \left[Q_r^T \cdot Q_r\right]^{-1} \cdot \left[Q_r^T \cdot \mathrm{T}\right] \tag{2.31}$$

Where

$$[k] = \begin{bmatrix} k_0 \\ k_1 \end{bmatrix},\ T = \begin{bmatrix} \tau_1 \\ \tau_2 \\ \vdots \\ \tau_n \end{bmatrix},\ Q_r = \begin{bmatrix} 1 & 1/Q_1 \\ 1 & 1/Q_2 \\ \vdots & \vdots \\ 1 & 1/Q_n \end{bmatrix} \tag{2.32}$$

As a result, the calibrated flow is obtained by

$$Q_c = \frac{k_1}{\bar{\tau} - k_0} \tag{2.33}$$

2.5. Experiments for calibration

To estimate the calibration factor, in [14] the calibration task was performed using experimental data from a water loop testing apparatus. This system has two physical settings: one with pipe diameter of 1 inch (2.54 cm) and TC spacing of 50 cm, (Figs. 2.9), and the other with a diameter of 0.5 inch (1.27 cm),(Fig. 2.15).

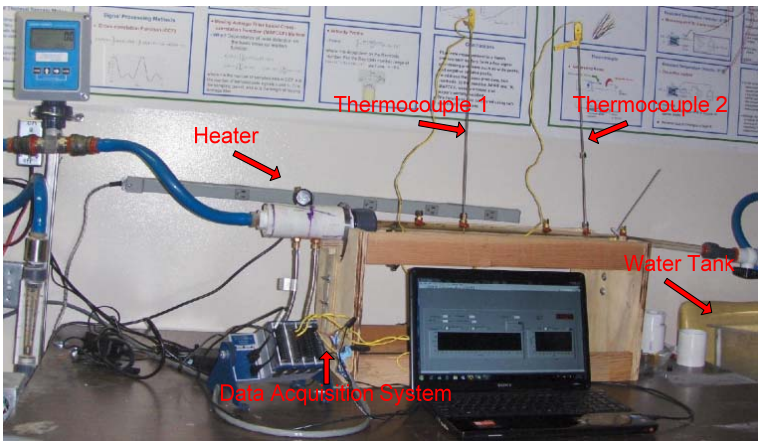

Fig. 2.15 The water-based test apparatus with pipe diameter of o.5 inch.

- Thermocouple location across the pipe

To get the flow velocity at different point across the pipe, the thermocouple tips have been placed at different radius points from 0 (the pipe center) to 0.8 (close to the pipe wall). Figs. 2.16 and 2.17 show the flow velocity profile for the flow of 0.5 to 4 *gpm*. The error bars indicate the standard deviation of the measured velocity in 10 experiment runs at different radius points.

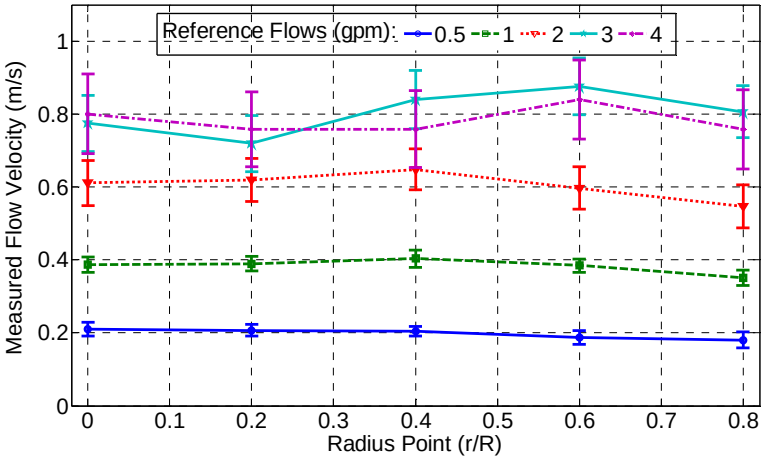

Fig. 2.16 Flow velocity versus radius point for the 1 inch pipe using 10 experiment runs.

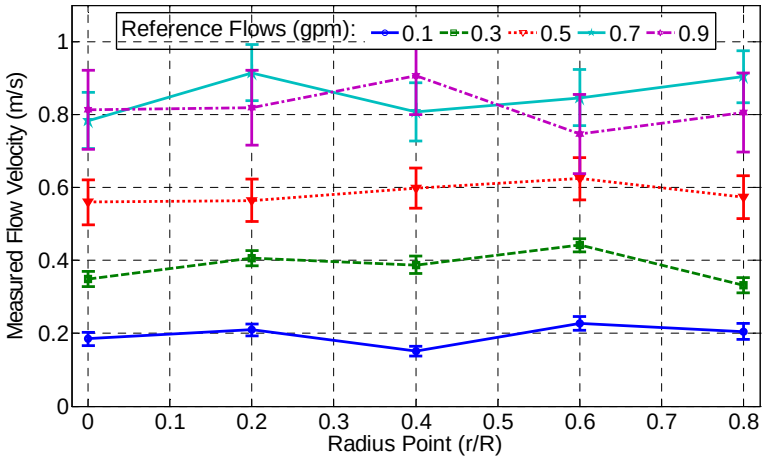

Fig. 2.17 Flow velocity versus radius point for the 0.5 inch pipe using 10 experiment runs.

As seen from Fig. 2.16, the deviation of the measured velocity is increased with the flow rate. In specific, for a higher flow (> 0.8 *m/s*), the deviation is too high so that it is hard to read the measured flow which agrees with the theoretical prediction given in Eq.(2.28). Also, similar results are seen in Fig. 2.17. For this pipe size setting, one may see that the flowmeter cannot distinguish the measured velocity above 0.8 *m/s*.

To choose the best location of the thermocouples tips across the pipe, the mean square error of measured velocity and the relationship between the measured flow velocities at each location with the mean flow velocity is considered. From Fig. 2.16, it is seen that the mean square errors for radius points less than 0.7 are likely the same. Therefore, from the accuracy point of view, any location inside this region can be a good location for the thermocouple tips. Also, it is seen that that the mean velocity over radius point of [0, 0.3] is close to the velocity measured at each point. That is,

$$V(r) \cong \overline{V} \qquad 0 \le r \le 0.3R \qquad (2.34)$$

As a result, any location interior this radial position shall be useful for the thermocouple tips. In addition, any point velocity in this region can gives a good estimate for the mean velocity.

- *Estimation of Calibration Coefficients*

The calibration coefficients have been estimated based on the data from the mean of 10 time delay estimates, each one using 100 temperature data from the two TCs. For each pipe, eight experimental data sets were considered: four for calibration points and four for validation of calibration model), each contains six time delay values corresponding to six reference flowrates. For the one inch pipe the reference flows were: 0.5, 1, 1.5, 2, 2.5 and 3 gpm and for the half inch pipe they were 0.1, 0.3, 0.5, 0.7, 0.9, 1.1 gpm. Tables 2.3 and 2.4 show the results of the linear regression model. As seen, in each data set the calibration coefficients are closed, meaning that the estimated coefficients are not sensitive to the measured data.

Table 2.3 Linear fitting results for the one inch pipe.

Experiments	1	2	3	4
k_0	0.065	0.0861	0.0520	0.0856
k_1	1.467	1.431	1.436	1.397
MSE of Fitting	0.005	0.005	0.003	0.003

Table 2.4 Linear fitting results for the half inch pipe.

Experiments	1	2	3	4
k_0	0.075	0.0745	0.0640	0.0763
k_1	1.453	1.424	1.433	1.416
MSE of Fitting	0.004	0.005	0.004	0.003

Tables 2.6 and 2.7 show the calibrated results. One may see that the calibrated flowrates tracks the reference flows but as the flow goes up the results will be far worse.

Table 2.5 Calibrated results using Eq. (2.33) for the one inch pipe.

Reference Flow (gpm)	Experiments			
	1	2	3	4
0.5	0.51	0.51	0.50	0.49
1	0.93	0.94	0.99	1.06
1.5	1.49	1.41	1.37	1.38
2	1.99	1.87	1.92	2.13
2.5	2.38	2.63	2.62	2.40
3	3.8	3.93	3.60	3.52

Table 2.6 Calibrated results using Eq. (2.33) for the half inch pipe.

Reference Flow (gpm)	Experiments			
	1	2	3	4
0.1	0.11	0.12	0.12	0.08
0.3	0.27	0.32	0.31	0.35
0.5	0.56	0.41	0.42	0.58
0.7	0.79	0.81	0.62	0.63
0.9	1.02	1.03	0.92	1.12
1.1	1.25	1.23	1.03	1.22

- *Validation of Calibration*

To validate the calibration model, a noise signal with amplitude equal to 0.50% of the full-scale amplitude was added to the measured time delay data. In this way, the effect of deviation in the estimated calibration coefficients on the calibrated flow is evaluated and it is seen how robust the calibration model against the noise. The error is measured by the following normalized mean square error equation,

$$NMSE = \frac{1}{M}\sum_{i=1}^{M}\left(\frac{\hat{Q}_c - Q_r}{Q_r}\right)^2 \qquad (2.35)$$

where $\hat{Q}_c$ is the calibrated flowrate using Eq.(2.33), Q_r is the reference flow, and M is the number of experiment runs.

The results are shown in Figs. 2.18 and 2.19. It is seen that the low flows like 0.5 *gpm* the calculated flow are resulted less than 10% error by introducing 0.50% error of the full-scale amplitude in the measured time delays. However, as flow goes up the error becomes larger. This is in agreement with the theoretical prediction given in Eq. (2.28).

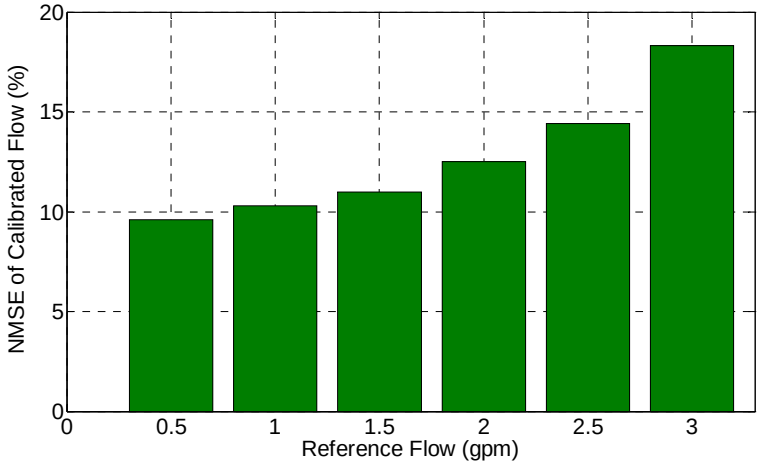

Fig. 2.18 The NMSE of calibrated flow using 4 experiment runs for the one inch pipe.

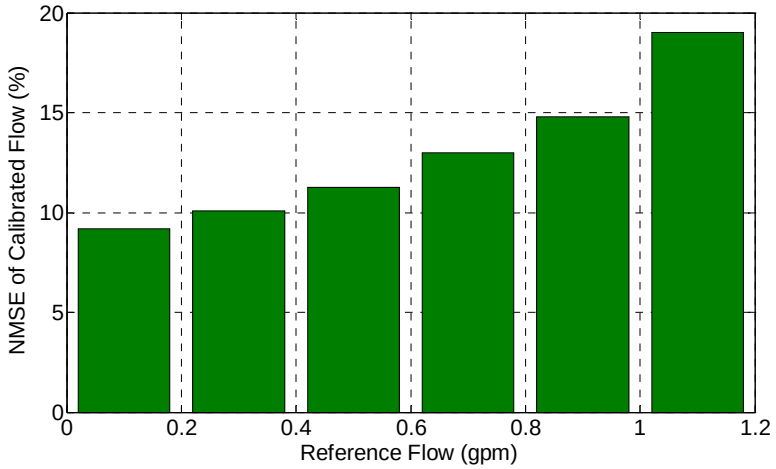

Fig. 2.19 The NMSE of calibrated flow using 4 experiment runs for the half inch pipe.

CHAPTER 3

FLOW RATE MEASUREMENT WITH BY-PASS DESIGN

The proposed technique is not efficient for the bigger size of the pipe and also for the higher flow rates. In these cases because of the slow response time of thermal sensor, dimension, and low strength of thermal signal this technique shows the weakness and we need thermal sensors with shorter response time plus strong heating signals which means more power. As a result we come up with a solution by using a small pipe for measurement and measuring a fraction of the flow. By using a bypass the measurement range will be increased and the velocity will be reduced. Due to complexity of analytical solution for the ratio of velocities in the by-pass pipe to the main pipe, numerical analysis were performed which verifies the linearity between two velocities. The ratio of the velocity in the bypass to the main pipe should be linear.

H: Height

L: Leading distance

17 inch long main pipe with diameter 1 inch

9 inch long by-pass with diameter 0.5 inch

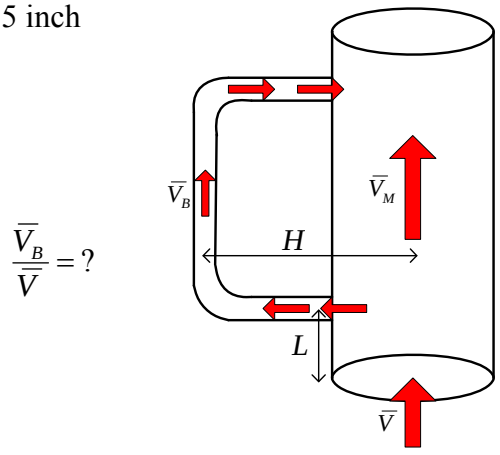

Fig. 3.1 Bypass design using in the simulation

3.1.Bypass (Flow Ratio Technique)

In the large-line-size flow measurement system, a very convenient and economical technique is the by-pass approach or flow ratio technique). As we can see in Fig. 3.1, a small by-pass flow leg is constructed on a larger flow line. Here the ratio of the flow rate in the bypass to the main line is constant. Therefore, a small flowmeter can be used for measuring the flow rate in main line by using the known constant value.

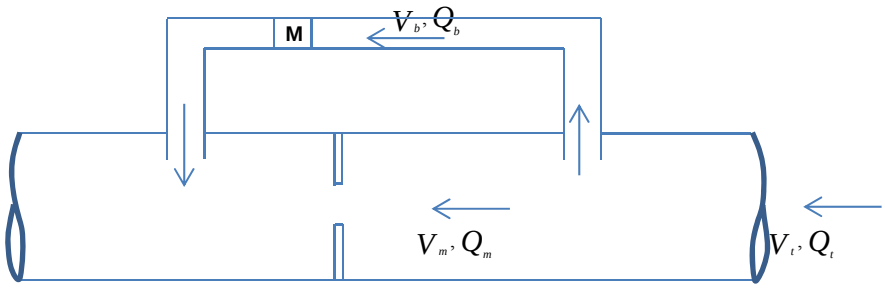

Fig. 3.2 Bypass Flowmeter

In Fig. 3.1 there is an orifice plate as a restrictor. The flow measuring is in the bypass line and the differential pressure-producing device can be used in the main line. The discharge coefficient of both restrictions in the main line and the bypass leg is constant and also independent of the flowrate.

Here the flow goes through the bypass which has a flowmeter. In the main line there is an orifice plate and the differential pressure which is developed across the orifice plate can be obtained by the following equation [18],

$$\Delta P_0 = \frac{\rho V_m^2}{2C^2}\frac{\left(1-\beta^4\right)}{\beta^4} \qquad (3.1)$$

where ρ is the density, V_m is the actual velocity in main line, β is beta ratio, and C is the discharge coefficient.

The pressure loss exists in two forms. One across the orifice and another one is a natural pressure loss between the intake and exhaust ports of the by-pass due to friction on the wall of the main line. The natural pressure drop can be obtained by[18],

$$\Delta P_1 = \frac{f\rho V_m^2}{2}\left(\frac{L}{D_m}\right) \tag{3.2}$$

Combining Eqs. (3.1) and (3.2) gives the total pressure loss between bypass ports in the main line[18],

$$\Delta P_b = \Delta P_0 + \Delta P_1 = \rho V_m^2\left[\frac{\left(1-\beta^4\right)}{2C^2\beta^4} + f\left(\frac{L}{D_m}\right)\right] \tag{3.3}$$

In Eq. (3.3) if *C* and *f* are independent of flowrate, then the term in the bracket will be constant.

The important observation that allows the calculation and relates the bypass flowrate to the main line flowrate is that the differential pressure ΔP_b generates between the inlet and the exhaust ports of the bypass leg, initiates flow in the bypass leg. Thus, the total pressure drop in the bypass leg must be equal to ΔP_b.

In general form the pressure drop in the by-pass leg can be expressed as[18],

$$\Delta P_b = K_b \frac{\rho}{2} V_b^2 \tag{3.4}$$

where V_b is the actual velocity in bypass line and K_b is the loss coefficient in the bypass line.

The loss coefficient in the by-pass line is composed of five parts: the inlet loss, the loss coefficient of two 90º elbows, friction loss due to the pipe length, the flowmeter loss coefficient, and the exit loss. It can be shown that [19],

$$K_b = 2K_{90^\circ\ elbow} + K_{pipe} + K_{meter} + K_{inlet} + K_{exit} \tag{3.5}$$

The velocity in the bypass V_b to the velocity in the main line V_m can be obtained by combining Eqs. (3.3) and (3.4)[19],

$$\frac{V_b}{V_m} = \left\{ \frac{2}{K_b} \left[\frac{\left(1-\beta^4\right)}{2C^2\beta^4} + f\left(\frac{L}{D_m}\right) \right] \right\}^{1/2} \tag{3.6}$$

In Eq. (3-6), if C, f, and K_b are constant, then the velocity ratio is constant and independent of flowrate.

Since the total flow splits between the main line and bypass, the total volumetric flowrate can be obtained by $Q_t = Q_m + Q_b$, where Q_t is total volume flow which is equal to $V_t A_m$, Q_m is the main line volume flow equal to $V_m A_m$, and Q_b is the by-pass line volume flow equal to $V_b A_b$.

And the final form[20],

$$Q_b / Q_t = \frac{\left(D_b / D_m\right)^2 \left(V_b / V_m\right)}{\left[1 + \left(D_b / D_m\right)^2 \left(V_b / V_m\right)\right]} \tag{3.7}$$

Therefore, we can obtain,

$$V_b / V_t = \frac{V_b / V_m}{\left[1 + \left(D_b / D_m\right)^2 \left(V_b / V_m\right)\right]} \tag{3.8}$$

The bypass piping is also needed when the flowmeter in the case of maintenance or failure cannot be taken out of the service. Therefore, the need for bypass valving is determined by the construction of the flowmeter and the nature of the process.

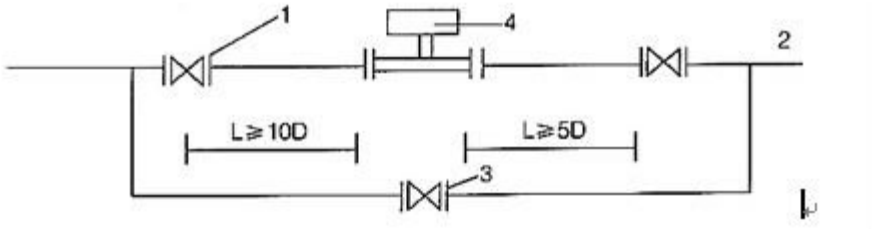

Fig. 3.3 Flowmeter Bypass Piping:1, 2, and 3 are the front valve, rear valve and bypass valve, respectively. 4 is the flowmeter. L≥10D and L≥5D are the lengths of the front and rear straight pipe segments, respectively.

Another application of the bypass flowmeter technique is in the large pipes where the flowmeter becomes impractical or uneconomical. The basic principle of bypass is to use an element that generates an output signal which is measured with another flowmeter. Most of these devices are producing the differential pressure which uses a secondary flowmeter to measure the flow developed by the differential pressure across the first flowmeter. The turndown of the system is limited to the secondary flowmeter, since the flow through the bypass is linear with the flow in the total flowmeter system. For the overall accuracy, the accuracy of both flowmeters must be considered.

3.2 Types of bypass flowmeters

- Orifice Plate/Turbine

Here, the orifice plate flowmeter is the primary and the turbine flowmeter is the secondary. This flowmeter often called a shunt flowmeter[21]. There is an in-line flowmeter in the 1 to 4- inch size which internally uses the bypass flow principle. The accuracy can be achieved up to ±2percent of rate over 10:1 range in some applications and applied for steam services and other gases [21].

- Orifice Plate/Rotameter

To achieve economical local indication over a wide turndown this type is used and it works with a differential pressure indicator. It can also be specified with a transmitter.

- *Orifice Plate/Thermal*

In this type, thermal flowmeter is a secondary flowmeter which is bypassing an orifice plate in some application.

- *Laminar Flow Element/ Thermal*

Here, thermal flowmeter can be used as a secondary flowmeter, bypassing a laminar flow in some applications [21].

- *Sensirion*

It uses digital micro-sensors which is for the humidity, temperature, mass flow controllers, and differential pressure sensors. It is useful for gas and liquid flow sensors and it is also used in the medical and HVAC industries. The sensors are the differential pressure sensors that measure the mass flow using a bypass configuration. In this design, a differential pressure in a flow channel will be generated by using an orifice or a linear flow restrictor. Therefore, the pressure is measured over the orifice and the difference in pressure before and after the orifice determines the volumetric flow in the channel. As a result, the mass flow can be calculated from this differential pressure over the orifice [21].

- *Mass Flow Controller (MFC)*

It is a device with a closed loop that measures the flow of gas or liquid, using mostly for thermal process with cost effective price. Elements of an MFC are base, sensor, bypass, control valve, and printed circuit board. Base is the platform that all other components placed on it. It contains the channel of gas and type 316 stainless steel [22]. The sensor is a thermal one and designed for quick response. The sensors are stable and

reliable in long term with very small diameter and mass for a faster response to the changes in gas flow. The bypass consists of a constant gas flow path. The total flow can be measured by measuring a small portion of gas passes through the sensor. The control valve responds to the signal generated by comparing the actual flow to the set point and by that it establishes the flow of gas. The printed circuit board in area of MFC shows optimum stability. It uses the minimum number of electronic components with highest reliability.

- *Operating principle of MFC*

The thermal sensor is the main component, consisting of a small bore tube plus two resistance-thermometer elements around outside of the tube. By applying electric current the sensor tube is heated. A temperature differential is created between the two elements by the cooling effects of the constant portion of gas flowing through the senor tube. The temperature differential will be measured as an electrical signal and the change in the resistance. The temperature differential depends on the mass flow and is a function of density, specific heat, and flowrate. The units of the mass flow are in standard cubic centimeters per minute (sccm) or in standard liters per minute (slm). The mass flow is converted into volume flow by the electronics of a mass flow controller and in standard conditions which is 0°C (32°F) and in 1 atmosphere [22]. It is because the volume of 1 mole of an ideal gas at 0°C (32°F) and 1 atmosphere occupies 22.4 liters, and 1 mole of gas will flow during 1 minute at a set point of 22.4 slm [22].

The function of the bypass is to force a constant portion of the gas toward the sensors. Due to the gas flow through the sensor tube, the heat transfers from upstream to downstream resistance-thermometer element. The temperature differential will be distributed into a zero to five volt (bridge circuit) flow output signal and comparing this

signal to the signal of mass flow controller in the external set point. The error signal that generates by this comparison causes the control valve to open or close and as a result it maintains a constant flow at the set point level [22]. Fig. 3.3 shows the diagram of this flowmeter.

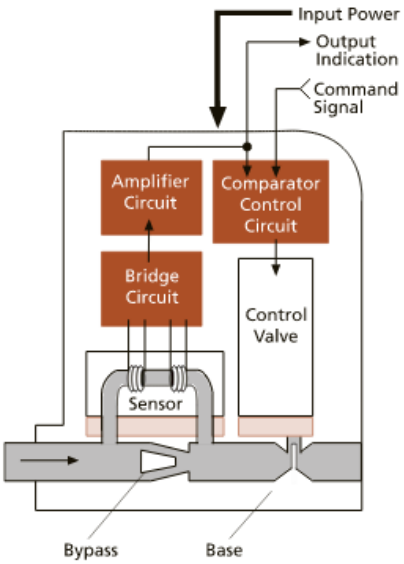

Fig. 3.4 Operational diagram of the mass flow controller.

CHAPTER 4

NUMERICAL SIMULATION OF THE DESIGNED FLOWMETER

4.1 Theoretical Equations

As mentioned in chapter 2, the correlated thermal signal flowmeter has two limitations: slow response time of the temperature sensors and need for large heating power in the big pipe applications. By using bypass flow measuring, the flow range in the by-pass will be reduced such that we can apply this technique efficiently.

- *Governing Equations of Computational Fluid Dynamics (CFD)*

Governing equations of fluid dynamics consists of continuity, momentum and energy equations [23]. These are the conservation equations,

4.1.1 The Continuity Equations

$$\frac{\partial \rho}{\partial t} + \nabla(\rho u) = 0 \rightarrow \frac{D\rho}{Dt} + \rho \nabla . u = 0 \qquad (4.1)$$

For incompressible flows,

$$\frac{D\rho}{Dt} = 0 \rightarrow \nabla . u = 0 \qquad (4.2)$$

There are two models for a continuum approach,

a) Finite Control Volume

Here, a closed volume within a finite region of flow defines a control volume *V*, and a finite surface *S*, as closed surface that bounds the volume. The control volume can be fixed in space while the flow is running, or the control volume maybe moving with the flow. The fluid flow equations can be earned directly by applying the integral form to the finite control volume. Besides these equations can be obtained indirectly from partial

differential equations which in both case called the conservation form of the governing equations for the time we are using a fixed control volume. When we are using a moving control volume with the fluid, both the integral and the conservation form is calling the non-conservation form of the governing equations.

b) Infinitesimal Fluid Element

An infinitesimally small fluid element with a differential volume (dV) is considered in the flow. It can be performed in two ways: The fluid element may be fixed in space with the fluid moving through it, or it may be moving and every point has a vector velocity V equal to the flow velocity. Here, the equation can be obtained by partial differential form and similar to the control volume, if it obtains from the fluid element fixed in space; they are the conservation form of equations. Whereas the partial differential equations obtained from the moving fluid element are called the non-conservational form of equations.

To understand the concept of the conservation of mass we will choose the finite control volume to be fixed in space and the infinitesimal fluid element will be moving with the flow. Then we will understand the differences between the conservation and non-conservation forms of the equations.

To reach the non-conservation form of the continuity equation, first the model of an infinitesimal fluid element is applied, and then the model to be moving with the flow is chosen.

$$\delta m = \rho \delta \nu \tag{4.3}$$

By using the physical meaning of substantial derivative,

$$\frac{D(\delta m)}{Dt} = 0 \tag{4.4}$$

Combining (4.1) and (4.2),

$$\frac{D(\rho\delta v)}{Dt} = \delta v \frac{D\rho}{Dt} + \rho \frac{D(\delta v)}{Dt} = 0 \rightarrow \frac{D\rho}{Dt} + \rho\left[\frac{1}{\delta v}\frac{D(\delta v)}{Dt}\right] = 0 \qquad (4.5)$$

$$\frac{D\rho}{Dt} + \rho\nabla\vec{V} = 0 \qquad (4.6)$$

Equation (4.4) is the continuity equation in non-conservation form.

The second model is a finite control volume fixed in space. There exists a control surface on which the flow velocity is $\vec{V}$ and the vector element surface aria is $d\vec{S}$. The elemental volume inside the finite control volume is *dv*. The mass is conserved on this control volume. We have $B = C$, where:

$B = S$ is the net mass flow out of control volume through surface

C is the time rate of decrease of mass inside control volume

For *B* that is equal to the product of density time's area of the surface and times component of velocity perpendicular to the surface, we can obtain the elemental mass flow across the aria *dS* as,

$$\rho V_n dS = \rho\vec{V}.\vec{dS} \qquad (4.7)$$

where $\vec{dS}$ is pointing in a direction out of the control volume. When $\vec{V}$ points out of the control volume, the product is positive. In this case; the mass flow that leaves the control volume, called the outflow. We can get a positive $\rho\vec{V}.\vec{dS}$ as an outflow. Whereas, when $\vec{V}$ points into the control volume the product is negative and this case is called inflow. So, a negative product of $\rho\vec{V}.\vec{dS}$ is an inflow.

As *S* is equal to the summation over the elemental mass flows, in the limit *B* becomes the surface integral,

$$B = \oiint_S \rho \vec{V}.\vec{dS} \tag{4.8}$$

To calculate *C*, we have:

The mass of the elemental volume of $d\nu$ is $\rho\, d\nu$,

The total mass of the control volume is $\oiiint_\nu \rho\, d\nu$,

The time rate of increased mass inside ν is: $\frac{\partial}{\partial t}\oiiint_\nu \rho\, d\nu$,

Therefore, the time rate of decrease of mass inside ν will be equal to,

$$C = -\frac{\partial}{\partial t}\oiiint_\nu \rho\, d\nu \tag{4.9}$$

Using $B = C$, we get $\oiint_S \rho \vec{V}.\vec{dS} = -\frac{\partial}{\partial t}\oiiint_\nu \rho\, d\nu$. Or,

$$\frac{\partial}{\partial t}\oiiint_\nu \rho\, d\nu + \oiint_S \rho \vec{V}.\vec{dS} = 0 \tag{4.10}$$

Equation (4.8) is the conservation form of the continuity equation.

Therefore, by choosing the model to be fixed in space we can obtain the conservation form of the continuity equation. The partial differential form also can be obtained. Since the control volume is fixed in space, the limits of integration for the integrals in equation (4.8) are constant and the time derivative $\frac{\partial}{\partial t}$ can be placed inside the integral. The surface integral can be expresses as a volume integral by applying the divergence theorem from vector calculus.

$$\oiint_S \rho \vec{V}.\vec{dS} = \oiiint_\nu \nabla.\left(\rho \vec{V}\right) d\nu \tag{4.11}$$

Substituting (4.11) into (4.8),

$$\oiiint_\nu \frac{\partial \rho}{\partial t}\, d\nu = \oiiint_\nu \nabla.\left(\rho \vec{V}\right) d\nu = 0 \tag{4.12}$$

Or,

$$\iiint_v \left[\frac{\partial \rho}{\partial t} + \nabla . \left(\rho \vec{V} \right) \right] d\nu = 0 \qquad (4.13)$$

In equation (4.13), the integrand has to be zero at every point within the control volume. That is,

$$\frac{\partial \rho}{\partial t} + \nabla . \left(\rho \vec{V} \right) = 0 \qquad (4.14)$$

which is the continuity equation in conservation form.

Both the conservation and non-conservation can be obtained from each other. Considering the vector identity involving the divergence of the product of a scalar times a vector as,

$$\nabla . \left(\rho \vec{V} \right) \equiv \rho \nabla . \vec{V} + \vec{V} . \nabla \rho \qquad (4.15)$$

Substituting equation (4.15) in the conservation form (4.14),

$$\frac{\partial \rho}{\partial t} + \vec{V} . \nabla \rho + \rho \nabla . \vec{V} = 0 \qquad (4.16)$$

The first two terms of the left side of equation (4.16) is the derivative of density. So,

$$\frac{D\rho}{Dt} + \rho \nabla . \vec{V} = 0 \qquad (4.17)$$

This is the non-conservation form of the equation (4.4).

4.1.2 The Momentum Equations

In this section the Newton's 2nd law ($\vec{F} = m\vec{a}$) is applied to a model of flow. Here, the moving flow element is chosen. So the net force on the fluid element will be equal to its mass times the acceleration of the element. This vector relation can be split into three scalar relations along the *x*, *y*, and *z*-axes. For the *x*-component of Newton's 2nd law,

$$F_X = ma_X \tag{4.18}$$

Where F_X is the scalar *x*-components of the force and a_X is the scalar *x*-components of the acceleration.

For F_X , the moving fluid element experiences a force in the *x*-direction. There are two sources for this force: body forces and surface forces. Body forces like gravitational, electric and magnetic forces, act directly on the volumetric mass of the fluid element at a distance. Surface sources act directly on the surface of the fluid element. There are two sources for surface forces. First, it is the pressure distribution acting on the surface from outside which is acting on the fluid element. Second, the shear and normal stress distributions acting on the surface from outside of the fluid which push on the surface creating the friction. For each element of the fluid in *x*-direction, the volume of the fluid element is $(dx\,dy\,dz)$. So,

Body force on the fluid element acting in *x* direction $= \rho f_X\,dx\,dy\,dz$

The shear stress τ_{xy} is related to the time rate of change in shearing deformation of fluid element.

The normal stress τ_{xx} is related to the time rate of change in fluid element (Fig. 4.1) . Both of stresses depend on the velocity gradients in the flow. In the viscose flow we usually ignore the normal stresses, because they are much smaller than the shear stresses. We just consider the normal stress when the normal velocity gradients are very large.

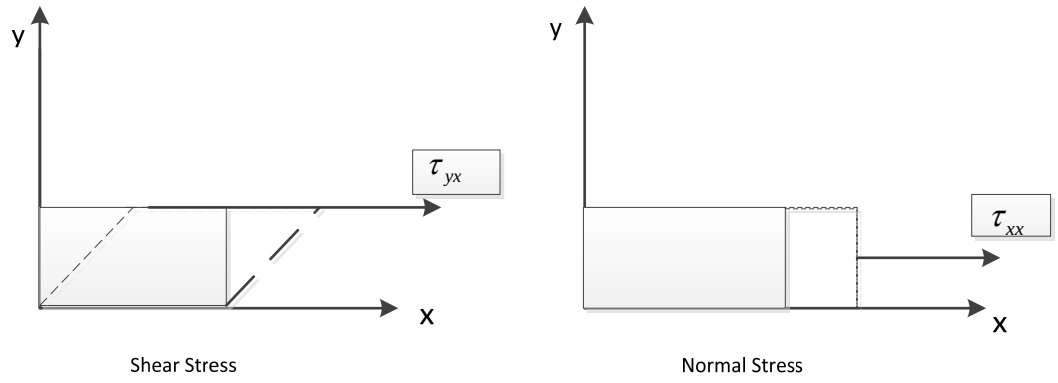

Fig. 4.1 Shear stress and normal stress.

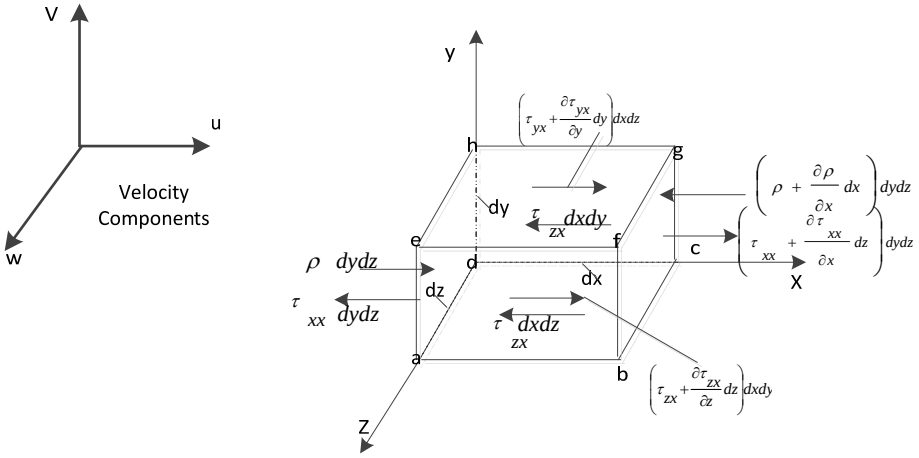

Fig. 4.2 Infinitesimally small, moving fluid element. The forces are in *x* direction.

Fig. 4.2, shows the surface forces in the *x* direction for a fluid element. Here to show a stress in the *y* direction which is exerted on a plane perpendicular to the *x* axis we use the notation τ_{ij} . From this figure the net force in the *x* direction will be,

$$\left\{\begin{matrix}Net\ suerface\ \ force\ in\\ the\ x-direction\end{matrix}\right\}=\left[\rho-\left(\rho+\frac{\partial\rho}{\partial x}dx\right)\right]dy\,dz+\left[\left(\tau_{xx}+\frac{\partial\tau_{xx}}{\partial x}dx\right)-\tau_{xx}\right]dy\,dz$$
$$+\left[\left(\tau_{yx}+\frac{\partial\tau_{yx}}{\partial y}dy\right)-\tau_{yx}\right]dx\,dz+\left[\left(\tau_{zx}+\frac{\partial\tau_{zx}}{\partial z}dz\right)-\tau_{zx}\right]dx\,dy$$

(4.19)

Therefore, the total force in *x*-direction F_x will be,

$$F_x = \left(-\frac{\partial \rho}{\partial x} + \frac{\partial \tau_{xx}}{\partial x} + \frac{\partial \tau_{yx}}{\partial y} + \frac{\partial \tau_{zx}}{\partial z} \right) dx\, dy\, dz + \rho f_x\, dx\, dy\, dz \qquad (4.20)$$

As the acceleration of the fluid element is the time-rate-of-change of its velocity, we get,

$$\alpha_x = \frac{Du}{Dt} \qquad (4.21)$$

By substituting in equation (4.14), we get the *x*-component of the momentum equation for viscous flow,

$$\rho \frac{Du}{Dt} = -\frac{\partial \rho}{\partial x} + \frac{\partial \tau_{xx}}{\partial x} + \frac{\partial \tau_{yx}}{\partial y} + \frac{\partial \tau_{zx}}{\partial z} + \rho\, f_x \qquad (4.22)$$

In similar way, for the *y* and *z* components of the momentum equation would be,

$$\rho \frac{Dv}{Dt} = -\frac{\partial \rho}{\partial y} + \frac{\partial \tau_{xy}}{\partial x} + \frac{\partial \tau_{yy}}{\partial y} + \frac{\partial \tau_{zy}}{\partial z} + \rho\, f_y \qquad (4.23)$$

$$\rho \frac{Dw}{Dt} = -\frac{\partial \rho}{\partial z} + \frac{\partial \tau_{xz}}{\partial x} + \frac{\partial \tau_{yz}}{\partial y} + \frac{\partial \tau_{zz}}{\partial z} + \rho\, f_z \qquad (4.24)$$

They are partial differential equation obtained from fluid element moving with the flow. Therefor the equations are in *non-conservative* form. They are scalar equations and called the *Navier-Stoke equations.*

The Navier-Stokes equations in conservation form is,

$$\rho \frac{Du}{Dt} = \frac{\partial u}{\partial t} + \rho \vec{V}.\nabla u \qquad (4.25)$$

Solving this equation we will obtain:

$$\rho \frac{Du}{Dt} = \frac{\partial (\rho u)}{\partial t} + \nabla.\left(\rho u \vec{V}\right) \qquad (4.26)$$

Substituting in non-conservative form, we will obtain the conservative form of The Navier-Stokes equations as,

$$\frac{\partial(\rho u)}{\partial t}+\nabla.\left(\rho u\vec{V}\right)=-\frac{\partial \rho}{\partial x}+\frac{\partial \tau_{xx}}{\partial x}+\frac{\partial \tau_{yx}}{\partial y}+\frac{\partial \tau_{zx}}{\partial z}+\rho f_x \qquad (4.27)$$

$$\frac{\partial(\rho u)}{\partial t}+\nabla.\left(\rho u\vec{V}\right)=-\frac{\partial \rho}{\partial y}+\frac{\partial \tau_{xy}}{\partial x}+\frac{\partial \tau_{yy}}{\partial y}+\frac{\partial \tau_{zy}}{\partial z}+\rho f_y \qquad (4.28)$$

$$\frac{\partial(\rho u)}{\partial t}+\nabla.\left(\rho u\vec{V}\right)=-\frac{\partial \rho}{\partial z}+\frac{\partial \tau_{xz}}{\partial x}+\frac{\partial \tau_{yz}}{\partial y}+\frac{\partial \tau_{zz}}{\partial z}+\rho\, f_z \qquad (4.29)$$

4.1.3 The Energy Equations

The physical principle is that the energy is conserved as stated by the first law of thermodynamics. By applying this principle to the moving fluid element we will have,

$$A = B + C \qquad (4.30)$$

where *A* is the rate of change of energy inside the fluid element, *B* is the net flux of heat into the element, and *C* is the rate of working done on the element due to body and surface forces.

The term *C*, which is the rate of work done by the body force acting on the fluid element moving at a velocity $\vec{V}$ is,

$$C = \rho\, \vec{f}\,.\vec{V}\left(dx\, dy\, dz\right) \qquad (4.31)$$

In Fig 4.3 the rate of work done on each face by surface forces in the *x*-direction is shown explicitly. Here, the positive *x*-direction does positive work and forces in the negative *x*-direction do negative work.

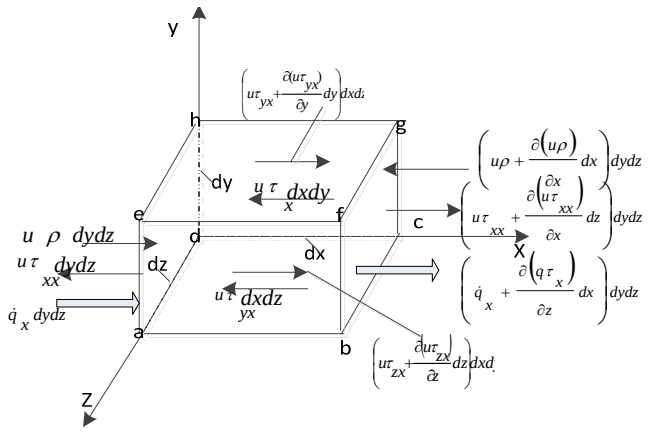

Fig. 4.3 Energy fluxes with an infinitesimally small, moving fluid element in x-direction.

The net rate of work done on the moving fluid element due to the forces on *x*-direction is,

$$\left[-\frac{\partial(up)}{\partial x}+\frac{\partial(u\tau_{xx})}{\partial x}+\frac{\partial(u\tau_{yx})}{\partial y}+\frac{\partial(u\tau_{zx})}{\partial z}\right]dx\,dy\,dz$$

Also adding the *y* and *z* direction to *x*-direction, the total of net rate of work done on the moving fluid element will be,

$$C=\left[\begin{array}{l}-\left(\frac{\partial(u\rho)}{\partial x}+\frac{\partial(v\rho)}{\partial y}+\frac{\partial(w\rho)}{\partial z}\right)+\frac{\partial(u\tau_{xx})}{\partial x}+\frac{\partial(u\tau_{yx})}{\partial y}+\frac{\partial(u\tau_{zx})}{\partial z}\\ +\frac{\partial(v\tau_{xy})}{\partial x}+\frac{\partial(v\tau_{yy})}{\partial y}+\frac{\partial(v\tau_{zy})}{\partial z}+\frac{\partial(w\tau_{xz})}{\partial x}+\frac{\partial(w\tau_{yz})}{\partial y}+\frac{\partial(w\tau_{zz})}{\partial z}\end{array}\right]dx\,dy\,dz+\rho\,\vec{f}\,.\vec{V}\,dx\,dy\,dz$$

(4.32)

For *B* part the heat flux is due to,

1) Volumetric heating such as absorption or emission of radiation.
2) Heat transfer across the surface due to temperature gradients for example thermal conduction. Here $\dot{q}$ denotes the rate of volumetric heat addition per unit mass. And the mass of moving fluid is equal to $\rho\,dx\,dy\,dz$. So,

$$\begin{Bmatrix} Volumetric\ Heating \\ of\ the\ element \end{Bmatrix} = \rho \dot{q}\, dx\, dy\, dz \qquad (4.33)$$

We also can see the heat transfer in Fig. (4.3) in *x*-direction by thermal conduction will be,

$$\left[\dot{q}_x - \left(\dot{q}_x + \frac{\partial \dot{q}_x}{dx} dx \right) \right] dy\, dz = -\frac{\partial \dot{q}_x}{\partial x} dx\, dy\, dz \qquad (4.34)$$

Also by adding the forces in *y* and *z* directions we obtain,

$$\begin{Bmatrix} Heating\ of\ the \\ fluid\ element\ by \\ thermal\ conduction \end{Bmatrix} = -\left(\frac{\partial \dot{q}_x}{\partial x} + \frac{\partial \dot{q}_y}{\partial y} + \frac{\partial \dot{q}_z}{\partial z} \right) dx\, dy\, dz \qquad (4.35)$$

Both volumetric heat and thermal conduction heat goes to term *B*:

$$B = \left[\rho \dot{q}_x - \left(\frac{\partial \dot{q}_x}{dx} + \frac{\partial \dot{q}_y}{\partial y} + \frac{\partial \dot{q}_z}{\partial z} \right) \right] dx\, dy\, dz \qquad (4.36)$$

Because of the proportionality of the thermal conduction heat transfer to the local temperature gradient, we may get,

$$B = \left[\rho \dot{q} + \frac{\partial}{dx}\left(k \frac{\partial T}{dx} \right) + \frac{\partial}{dy}\left(k \frac{\partial T}{dy} \right) + \frac{\partial}{dz}\left(k \frac{\partial T}{dz} \right) \right] dx\, dy\, dz \qquad (4.37)$$

Term *A* is the time-rate-of-change of energy of the fluid element. For the total energy of a moving fluid per unit mass, we consider the sum of the internal energy per unit mass, *e*, and the kinetic energy per unit mass, $V^2/2$. So the total energy would be ($e+V^2/2$). For a moving fluid element the substantial derivative is used. We know that the mass of fluid element is $\rho\, dx\, dy\, dz$, So,

$$A = \rho \frac{D}{Dt}\left(e + \frac{V^2}{2} \right) dx\, dy\, dz \qquad (4.38)$$

Therefore, the final form of energy equation in *non-conservation* form for a moving fluid element will be,

$$\rho\frac{D}{Dt}\left(e+\frac{V^2}{2}\right)=\rho\dot{q}+\frac{\partial}{dx}\left(k\frac{\partial T}{dx}\right)+\frac{\partial}{dy}\left(k\frac{\partial T}{dy}\right)+\frac{\partial}{dz}\left(k\frac{\partial T}{dz}\right)-\left(\frac{\partial(u\rho)}{\partial x}+\frac{\partial(v\rho)}{\partial y}+\frac{\partial(w\rho)}{\partial z}\right)+$$
$$\frac{\partial(u\tau_{xx})}{\partial x}+\frac{\partial(u\tau_{yx})}{\partial y}+\frac{\partial(u\tau_{zx})}{\partial z}+\frac{\partial(v\tau_{xy})}{\partial x}+\frac{\partial(v\tau_{yy})}{\partial y}+\frac{\partial(v\tau_{zy})}{\partial z}+\frac{\partial(w\tau_{xz})}{\partial x}+$$
$$\frac{\partial(w\tau_{yz})}{\partial y}+\frac{\partial(w\tau_{zz})}{\partial z}+\rho\vec{f}.\vec{V} \qquad (4.39)$$

For the conservation form, starting from the definition of the substantial derivative,

$$\rho\frac{De}{Dt}=\rho\frac{\partial e}{\partial t}+\rho\vec{V}.\nabla e \qquad (4.40)$$

$$\rho\frac{\partial e}{\partial t}=\frac{\partial(\rho e)}{\partial t}-e\frac{\partial\rho}{\partial t} \qquad (4.41)$$

From the vector identity (divergence of the product of a scalar, times a vector), we have,

$$\rho\vec{V}.\nabla e=\nabla.\left(\rho e\vec{V}\right)-e\nabla.\left(\rho\vec{V}\right) \qquad (4.42)$$

Substituting into Eq. (4.41),

$$\rho\frac{De}{Dt}=\frac{\partial(\rho e)}{\partial t}-e\left[\frac{\partial\rho}{\partial t}+\nabla.\left(\rho\vec{V}\right)\right]+\nabla.\left(\rho e\vec{V}\right) \qquad (4.43)$$

According to the continuity equation, the term in the bracket is zero. So it reduces to,

$$\rho\frac{De}{Dt}=\frac{\partial(\rho e)}{\partial t}+\nabla.\left(\rho e\vec{V}\right) \qquad (4.44)$$

Therefore,

$$\frac{\partial(\rho e)}{\partial t}+\nabla.\left(\rho e\vec{V}\right)=\rho\dot{q}\ +\frac{\partial}{\partial x}\left(k\frac{\partial T}{dx}\right)+\frac{\partial}{dy}\left(k\frac{\partial T}{dy}\right)+\frac{\partial}{dz}\left(k\frac{\partial T}{dz}\right)-\rho\left(\frac{\partial u}{\partial x}+\frac{\partial v}{\partial y}+\frac{\partial w}{\partial z}\right)+$$

$$\lambda\left(\frac{\partial u}{\partial x}+\frac{\partial v}{\partial y}+\frac{\partial w}{\partial z}\right)^2+$$

$$\mu\left[2\left(\frac{\partial u}{\partial x}\right)^2+2\left(\frac{\partial v}{\partial y}\right)^2+2\left(\frac{\partial w}{\partial z}\right)^2+\left(\frac{\partial u}{\partial y}+\frac{\partial v}{\partial x}\right)^2+\left(\frac{\partial u}{\partial z}+\frac{\partial w}{\partial x}\right)^2+\left(\frac{\partial v}{\partial z}+\frac{\partial w}{\partial y}\right)^2\right]$$

(4.45)

Instead of using the integral energy e, by using the total energy $(e+V^2/2)$ [A], we get,

$$\frac{\partial}{\partial t}\left[\rho\left(e+\frac{V^2}{2}\right)\right]+\nabla.\left[\rho\left(e+\frac{V^2}{2}\vec{V}\right)\right]=\rho\dot{q}\ +\frac{\partial}{\partial x}\left(k\frac{\partial T}{dx}\right)+\frac{\partial}{dy}\left(k\frac{\partial T}{dy}\right)+\frac{\partial}{dz}\left(k\frac{\partial T}{dz}\right)$$

$$-\frac{\partial(u\rho)}{\partial x}-\frac{\partial(v\rho)}{\partial y}-\frac{\partial(w\rho)}{\partial z}+\frac{\partial(u\tau_{xx})}{\partial x}+\frac{\partial(u\tau_{yx})}{\partial y}+\frac{\partial(u\tau_{zx})}{\partial z}+\frac{\partial(v\tau_{xy})}{\partial x}+\frac{\partial(v\tau_{yy})}{\partial y}+\frac{\partial(v\tau_{zy})}{\partial z}$$

$$+\frac{\partial(w\tau_{xz})}{\partial x}+\frac{\partial(w\tau_{yz})}{\partial y}+\frac{\partial(w\tau_{zz})}{\partial z}+\rho\,\vec{f}.\vec{V}$$

(4.46)

4.2 Simulations and Computations

The computations are performed by CFD ANSYS Fluent 14 [24], water is considered as the flow, and three dimensional geometry is considered for computation.

- Part 1: Simulation of the transit time flowmeter in a single pipe

At first we designed a simple pipe with an outer diameter of 1 inch and the inner diameter of 0.021 inch. A heater with 10 *cm* long is located on the outside wall of the pipe and 20 *cm* away from the inlet. The first thermocouple is placed along the pipe 30 *cm* next to the heater. The next thermocouple is placed on the distance 50 *cm* from the first one. The pipe length is 150 *cm*. The design is performed in 2D and 3D. One time

was without thermocouple and another time by inserting the two thermocouples. The flowrate range is from 1 to 4 GPM.

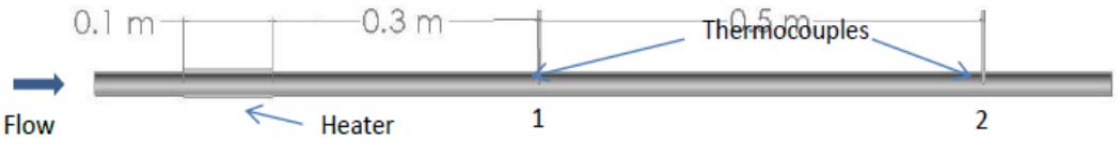

Fig.4.4 Flowmeter design

4.2.1Geometry and Mesh

- 2D Simulation without Thermocouple

To reach the same results and time delay like the other designs here, we design this part as planar instead of axisymmetric. The heater is placed on the surface of wall. So, we use $\left(W/M^2\right)$ for the heat flux as the heater source. There is one part and one body as Fluid. The element size of the mesh is 0.001*m* and 60 mesh in radial direction. The total elements are 90000 by using the advanced size function as On, Curvature and fine mesh which is useful for the thermal transfer in Fluent. Using the transient time the profile for one second on and then off will be,

- ((heater transient 3 0 0)
- (time0.000000e+00 1.000000e+00 2.000000e+00)
- (source7.582651e+04 0.000000e+00 0.000000e+00))

The power of heater is 500 *W* which is divided by the surface area to give the heat flux of 7.582651e+04 $\left(W/M^2\right)$.

- 2D Simulation with Thermocouple

The geometry can be designed by creating two surfaces from sketches and using Boolean to subtract, so we have just one part and one body. The diameter of the thermocouple is 0.125 inch. The 2D with thermocouple is planar with the mesh size of 0.0006 *m* plus the inflation with the total thickness of 0.0015, using 17 layers and the growth rate of 1.2. Also here the thermocouples are considered as a wall so that the inflation applied to the thermocouples too.

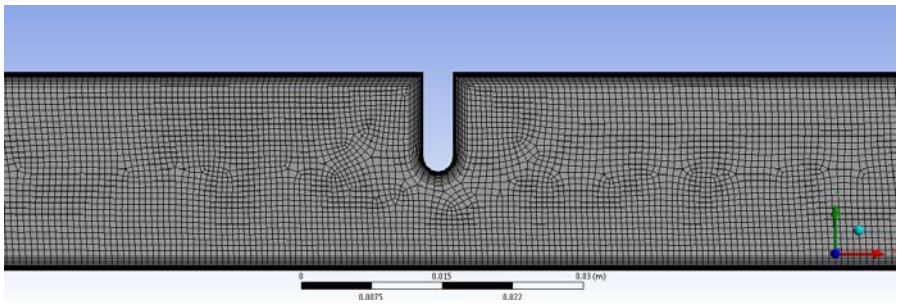

Fig.4.5 Mesh generated for 2D around the thermocouple

- 3D without thermocouple

Three different pipes are considered with two inflations. One from the wall and one from the heater with the first layer thickness of 8.0898e-005 with maximum layers of 10 and growth rate of 1.2 are performed.

The turbulent boundary layer thickness can be calculated by,

$$\delta = \frac{0.16\, x_1}{\mathrm{Re}_{x_1}^{1/7}}$$

$$x_1 = \left(\frac{1*0.021}{2}\right)*\frac{\pi}{2} = 0.016485$$

$$\mathrm{Re} = \frac{\rho v D}{\mu} = \frac{998.2*(0.1822479)*(0.021)}{0.001003} = 3808.89 \qquad (4.47)$$

$$v = 1GPM = 0.1822479 \text{ m/s}$$

$$\delta = 8.122\text{e-}4m$$

Since the Fluent has the limitation in mesh for academic use only, and the thickness of the inflation should be higher than the calculated in above, we are selecting the 5% to 10% of the diameter for the inflation, which is $0.0021m$.

The first layer thickness can be calculated by,

$$\delta = \sum_{k=0}^{n-1} ar^k = a\frac{1-r^k}{1-r} \tag{4.48}$$

For the 10^{th} layer with growth rate of $1.2r$, we have,

$$\delta = S_1 + S_1 r + S_1 r^2 + S_1 r^3 + ...S_1 r^9 = \sum_{k=0}^{9} S_1 r^k = S_1 \frac{1-r^{10}}{1-r}$$
$$0.0021 = S_1 \frac{1-(1.2)^{10}}{1-1.2} \rightarrow S_1 = 8.0898\text{e-}5\ \text{m} \tag{4.49}$$

- 3D with thermocouple

The sweep operation is used for creating three different pipes. Another design is for the thermocouple that can be created by the combination of the sphere and the sweep and a Boolean operation to unify these and finally another Boolean to subtract the thermocouple from the pipe. At the end, we have one part and three bodies as fluid. Here the pipe created as half so we name the symmetry, wall, and heater. The inside of the thermocouples are also wall.

The mesh is the same as 3D without thermocouple but because the thermocouple are selected with wall the inflation also include around them. In this case, the total element mesh will be 487246.

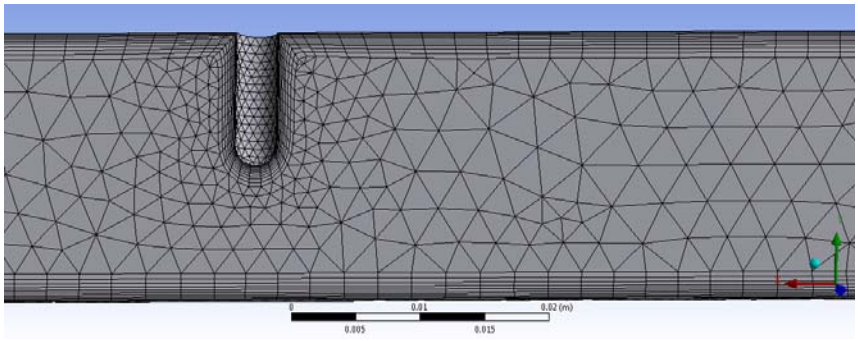

Fig.4.6 Mesh generated for3D around the thermocouple

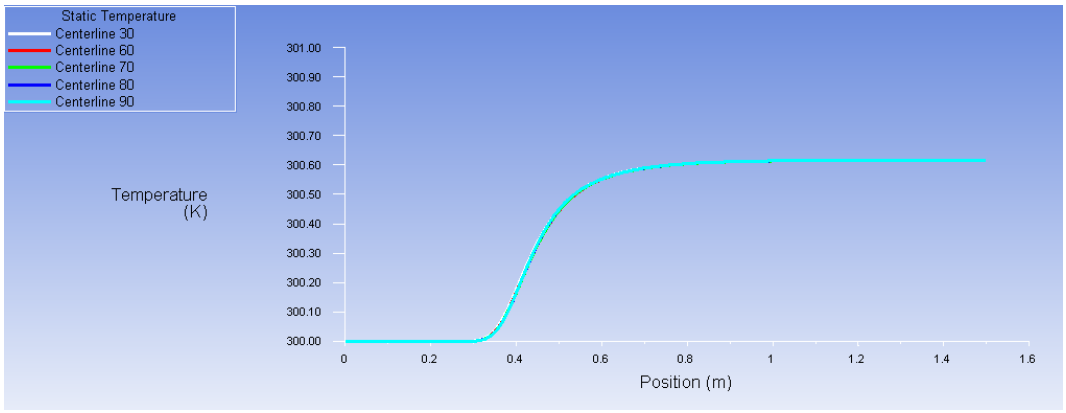

Fig.4.7. 2D compare of different mesh in radial direction at centerline location

4.2.2 Verification and Validation of Mesh

For 2D as we increase the number of meshes in radial direction no difference in mesh at different locations happened.

At the first thermocouple position (TC1) which is named line 1, also no difference in temperature plot comparison happened.

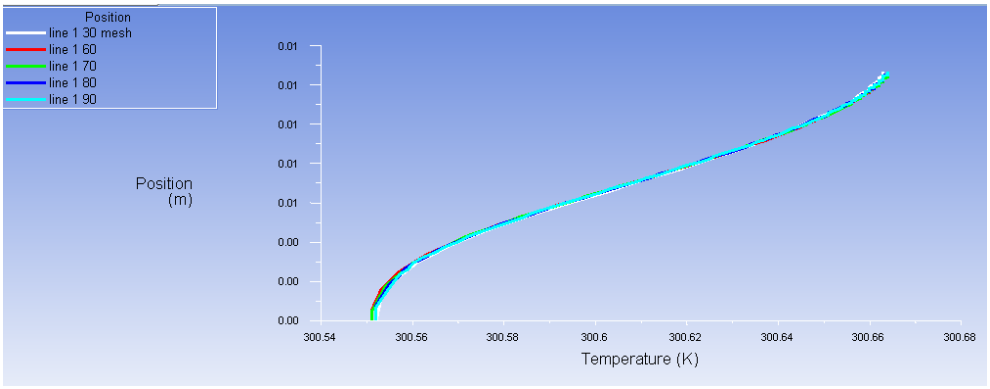

Fig.4.8 2D compare of different mesh in radial direction at TC1 location

For 3D without TC, comparison of mesh is made by applying the adaption on gradient and computing for the velocity, then putting the refined threshold to 10 percent of that, the adaption will be perform for 62749 cells then run the simulation again and compare the results in post processing. Here, the results show that the mesh is enough because by increasing the number of mesh (which exceeds more than limitation) the velocity in radial direction overlaps (Fig 4.9).

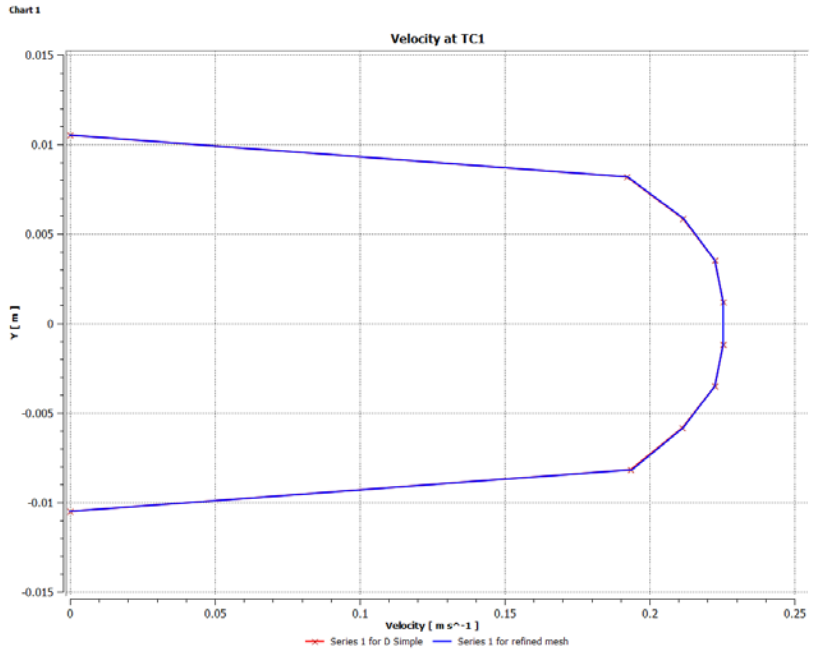

Fig.4.9 Compare of mesh and the refined one for velocity at radial direction at TC1 location.

4.2.3 Boundary Conditions

The heater power is 500 W and since it is located at the surface of the pipe the heat flux is 7.582651e+04 $\left(W/M^2\right)$. The boundary condition of the inlet is the velocity inlet and the flow rate range is from 1 to 4 GPM. For outlet we choose zero Pascal pressure outlets.

Since we have a circular pipe, the flow is axially symmetric. So for a symmetric flow, one of the boundaries is the axis of symmetry. Here, the axis of symmetry is the centerline of the flow which at the centerline the velocity field is the maximum.

Boundary condition 1 (symmetry), for all $z, r = 0$,

$$\frac{\partial v_z}{\partial r} = 0 \qquad (4.50)$$

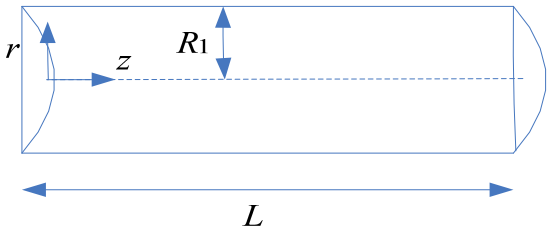

Fig.4.10 Boundary conditions at simple pipe.

Next boundary is the wall of the pipe. There is a no slip boundary condition which means the flow velocity is zero at the walls. The position of the wall is $r = R_1$, ($0 < z < L$).

Boundary Condition 2 (no slip):

$$\{0 \prec z \prec L \qquad r = R_1 \qquad v_z = 0 \qquad (4.51)$$

Using the transient time the profile for one second on and then off will be,

- ((heater transient 3 0 0)

- (time0.000000e+00 1.000000e+00 2.000000e+00)
- (source7.582651e+04 0.000000e+00 0.000000e+00))

Heating pattern is Single Pulse and for 1 second on and then off.

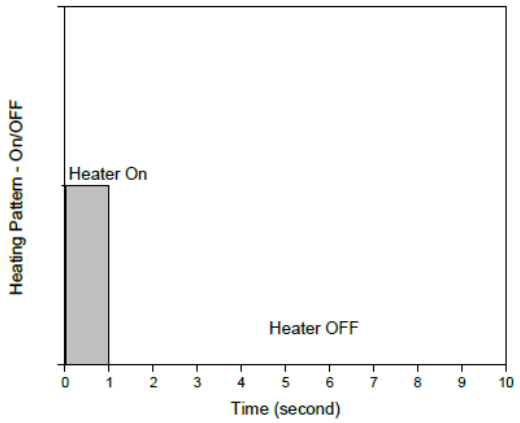

Fig.4.11 Heating pattern for transient time.

4.3 Results and Discussions

The setting used here includes transient time, K-epsilon model with energy equations on. Also the water is using as fluid, and the steel is using as solid. Using second order dissipation for Momentum, Turbulent, and Energy help better convergences along with the double precision. We are creating different points close to the thermocouples with the same location with TC or without TC design. Then we compare the time delays of each point in each flow rate. By having the time delay we can calculate the flow rate in GPM and compare it with the reference flow rate which is from 1 to 4 GPM.

Since we are using the transient time, the settings for the monitors would be creating some surface monitors based on the selected points with the flow variable of temperature and the *X*-Axis of flow time. By selecting print, plot and write, later we extract the files for time delay and temperature profile. Since the heater is 1 second On and then Off, for

the 2D simulation picking 0.01 as time step so auto save every 50 time steps. For the results we may import each saving data to show the velocity contours. Also in post processing temperature contours for each saving will be shown as seen in Fig. 4.12.

4.3.1 Temperature distribution along the pipe (Temperature contours)

We saved the data every 0.5 *s*. Then we do the post processing for each saved data. For 2D simulation, the temperature distribution for 1 GPM is shown in Fig. 4.12. From these figures we can see how the temperature will be mixed and how it has been taken integral by the fluid after seconds.

As we can see from the contours, the flow starts to mix the temperature toward the end. This mixing is also happens for the velocity. That's one reason we can conclude the fluid is already take the integral and we don't need to take the integral velocity. Using the distance between the TCs which is 0.5 *m*, over the obtained time delay, the average velocity for calculating the flow rate is obtained. The verification can be shown by simulation that if we take the integral velocity along a plane in three dimensional the result will be the same as by calculating the velocity from the time delay.

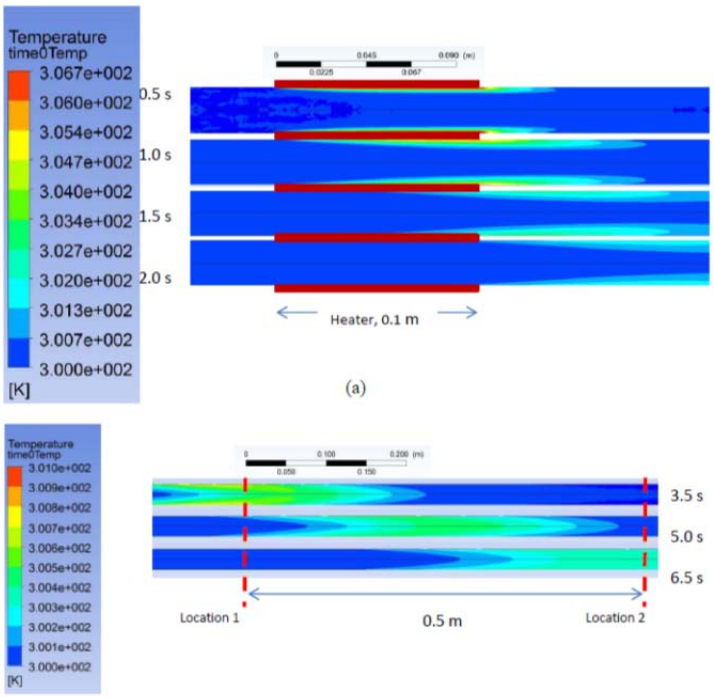

Fig.4.12 Contours of temperature in different times, 2D W/O TCs.

4.3.2 Velocity distribution along the pipe

In steady state, running the 2D simulation for a simple pipe without thermocouple, gives us the velocity distribution as shown in Fig. 4.13. At first, there is the inlet velocity which goes to the fully development soon because the flow is turbulent and the diameter of the pipe is small. Plotting data in radial direction at the position of two thermocouples gives us the plot figure like the turbulent fully developed (Fig. 4.14).

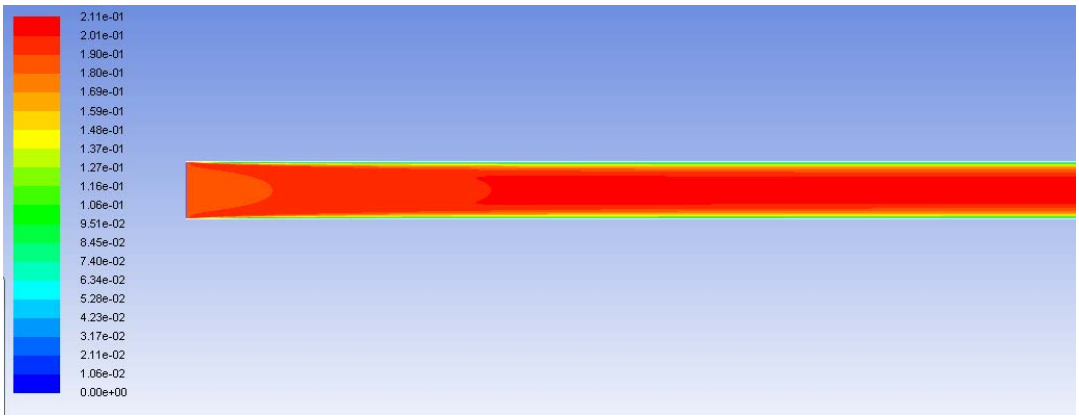

Fig.4.13Contours of velocity in steady state, 2D without TCs, *Q*=1GPM.

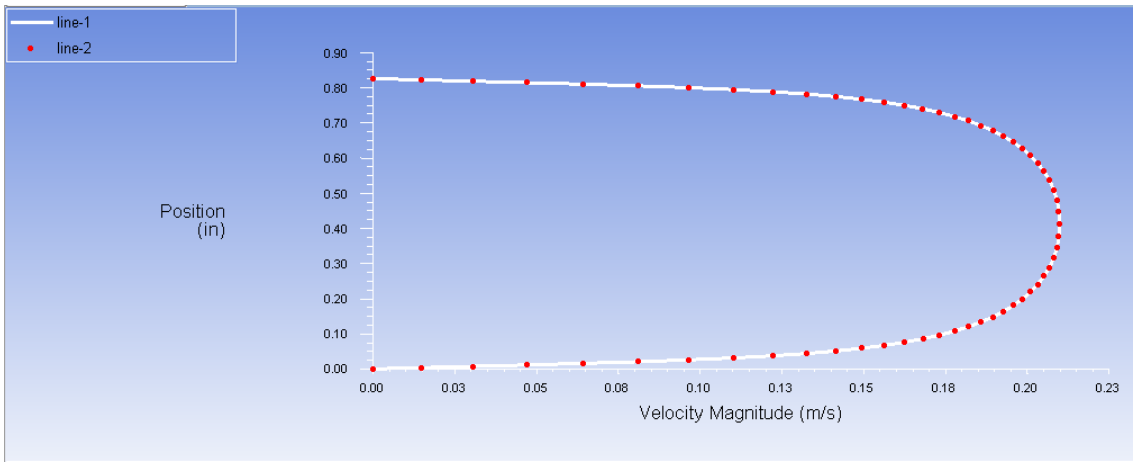

Fig.4.14 Plot of position v.s. velocity in steady state, 2D position of the first and second thermocouple.

4.3.3 Time Delay and Flowrate Calculations

We got the results from experiment as explained in section 2.5 as well as simulation results. The first task is to perform the simulation in both two dimensions and three dimensions and comparing with or without thermocouples. The results show that all the time delay and calculated GPM by the simulations are quite overlapping specially for lower flow rates (Fig 4.15). Since the three dimensional is more close to the reality we

pick that one. Also the results of with and without thermocouples are the same. The results are shown in Fig 4.16.

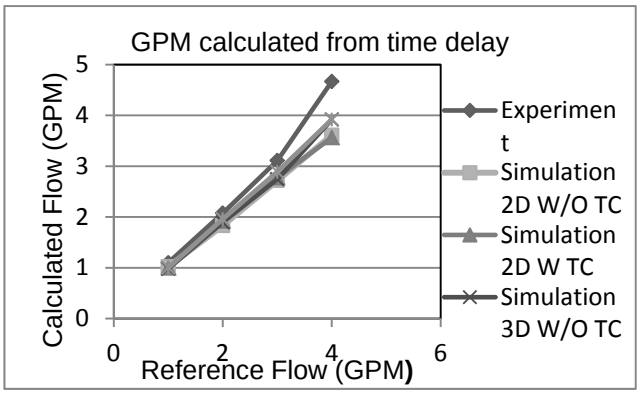

Fig.4.15. the temperature profile detected from locations 1 and 2.

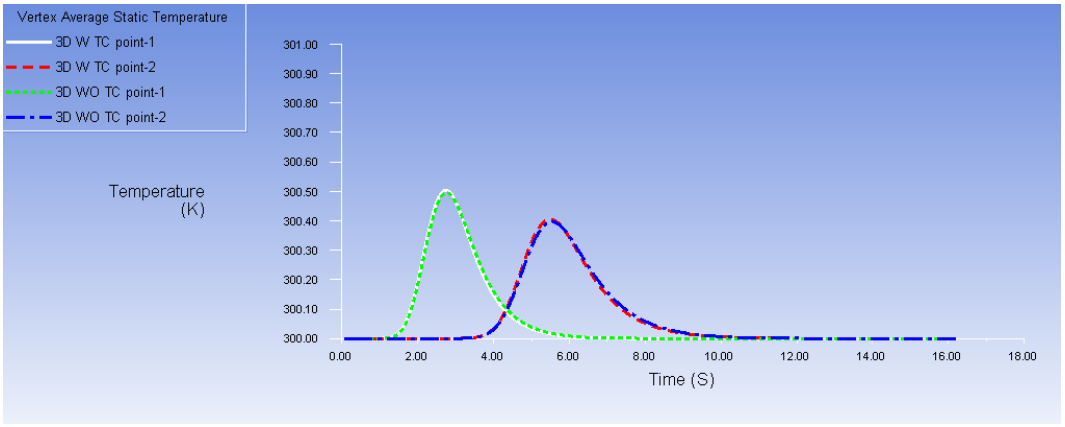

Fig.4.16 The temperature profile detected from locations 1 and 2, Q= 1GPM.

As we can see at location 2, the peak temperature drops which verifies that the cold and hot water are mixing in the pipe.

From the signal processing point of view, we can calculate the time delay of the two signals. That helps to find the flowrate. As we can see in Fig. 4.17 the location of three points at each thermocouple are selected and each pare compared (Fig. 4.18).

Point 1, at Y=0 and X=0.6 m or 23.622 inch, exactly at TC1 location.

Point L, at Y= - 0.058690 inch and X= 23.465 inch

Point M, at Y= - 0.058690 inch and X=23.622 inch

Point R, at Y= - 0.058690 inch and X=23.78 inch

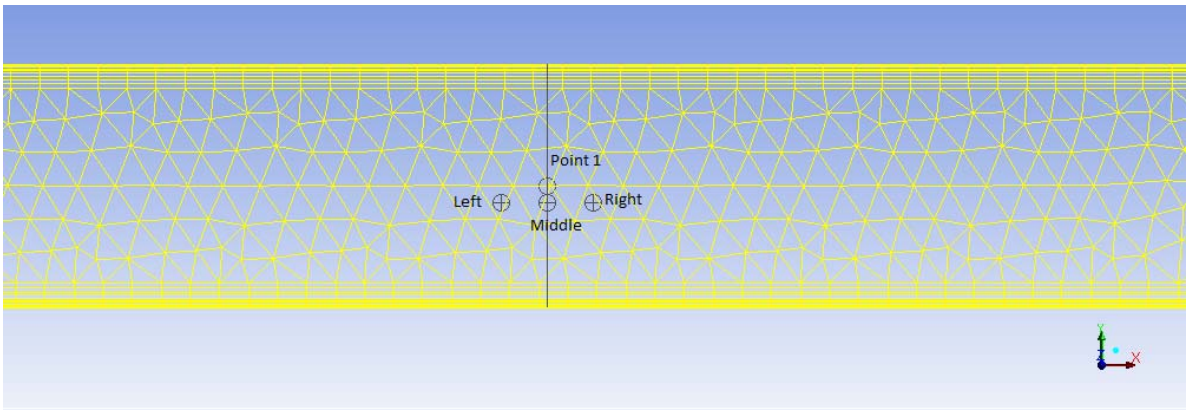

Fig.4.17 Different point at the first thermocouple location (TC1).

The corresponding points for the second thermocouple is

Point 2, at Y=0, X=43.307 inch

Point L, at Y= - 0.058690 inch and X= 43.15 inch

Point M, at Y= - 0.058690 inch and X=43.307 inch

Point R, at Y= - 0.058690 inch and X= 43.46 inch

The results show that the entire first location regions (TC1) are overlapping as well as the second region (TC2). That's confirmed for the four flowrates and for pipe with/without thermocouples.

Three dimensional simulations for 1 GPM flowrate, by having the thermocouples in the pipe are shown in Figure 4.18.

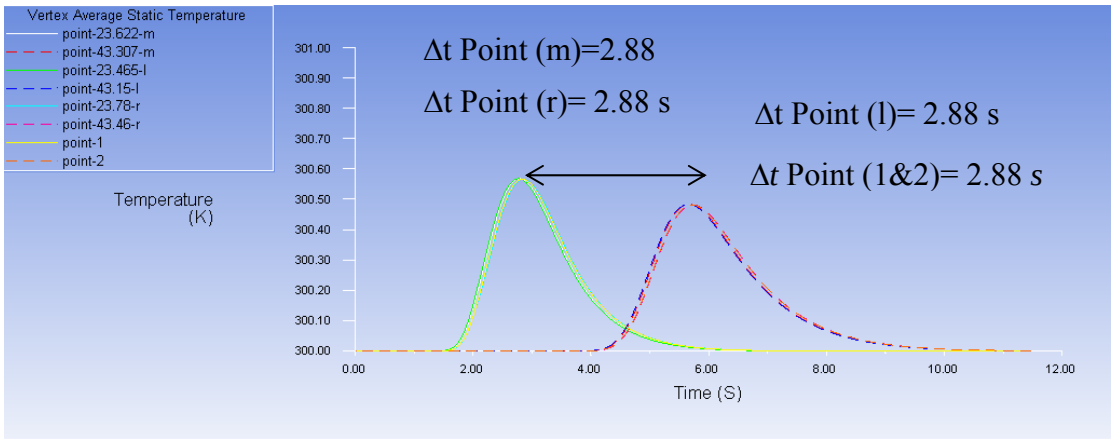

Fig.4.18. Time delay calculation for different points at TC1 and TC2. The flowrate is 1 GPM.

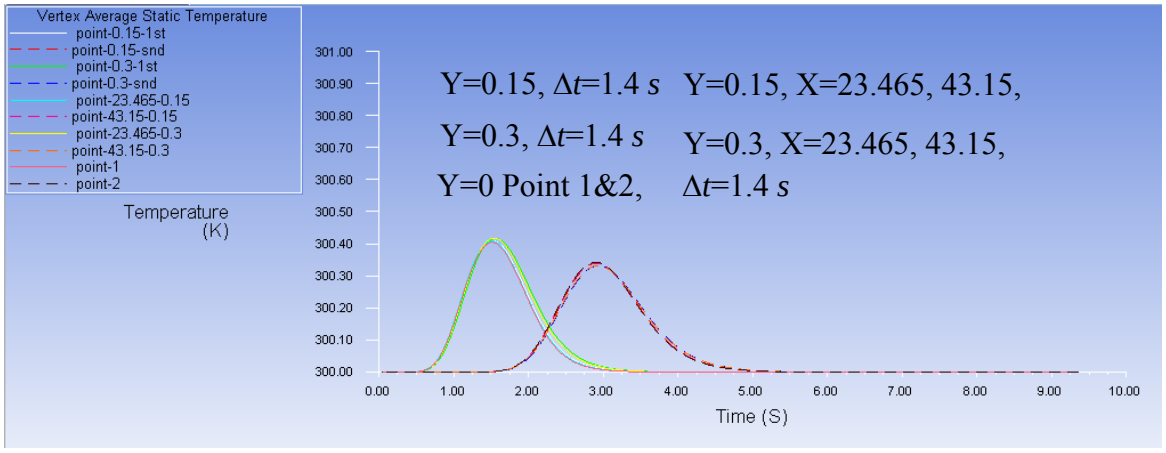

Fig.4.19. Time delay calculation for different points at radial direction at the location of TC1 & TC2. The flowrate is 2 GPM.

Since the results of the 3D with thermocouple overlaps with those of 3D without thermocouple, we are showing here the 3D with inserting the two thermocouples.

Table 4.1 Calculated flowrate from time delay (3D Simulation)

GPM	Delay (point *M*)	Velocity (*m/s*)	Calculated GPM
1	2.88	0.178	0.98
2	1.4	0.357	1.961
3	0.95	0.526	2.889
4	0.7	0.714	3.921

At higher flowrates the peak for temperature decreases. For 1 GPM at least 0.5 degree increases in temperature is acceptable by the signal processing computation to detect the peak points. As the flowrate increases, this way makes it unsuitable for measuring the fluid.

Table 4.2 The experimental results.

GPM	Delay (point *M*)	Velocity (*m/s*)	Calculated GPM
1	1.7	0.294	0.953
2	0.9	0.555	1.961
3	0.6	0.833	2.889
4	0.4	1.25	3.921

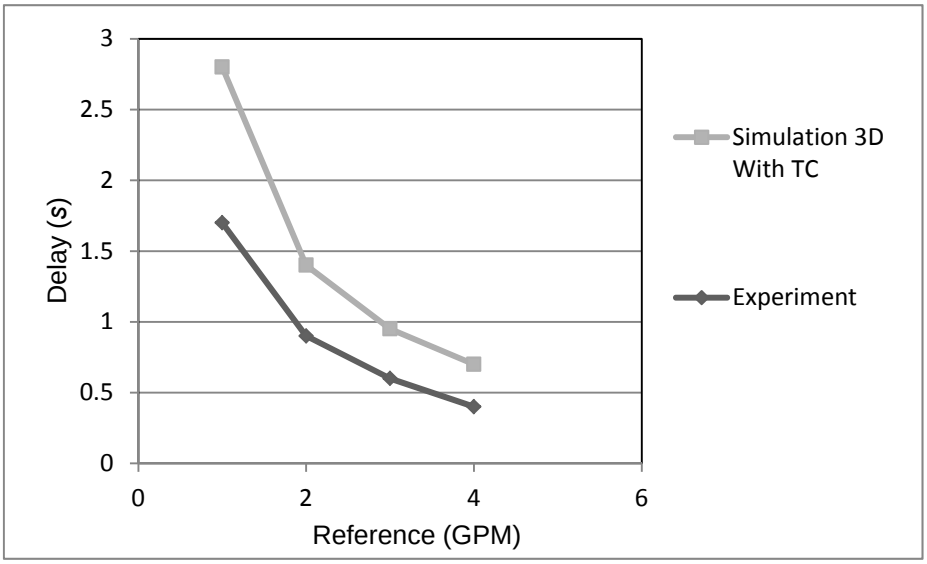

Fig.4.20 Time delay comparison at flowrate range of 1 to 4 GPM as the reference flow.

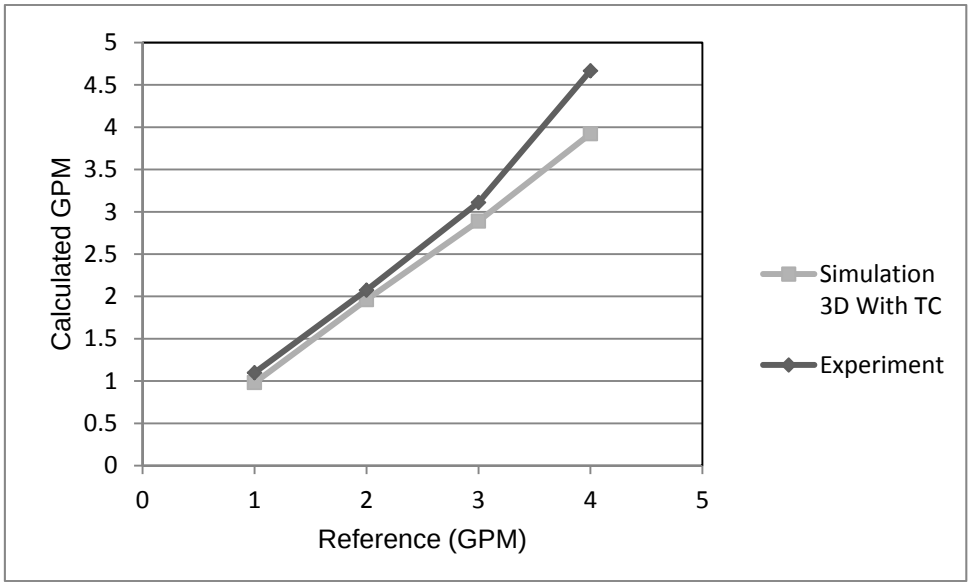

Fig.4.21. The calculated flowrate over the reference flow, using the data in table 4.1 and 4.2.

There is a 4% deviation for experimental data. There are some measurement errors in experiment that might come from the conduction, which leads the temperature from heater to wall and to thermocouples.

Table 4.3 calculated the measurement error for experiment.

Reference GPM	Calculated GPM	Ratio	Alfa (average of ratios)	Calculated GPM/Alfa	Measurement error
1	1.614	1.614	1.59422	1.012	-0.012
2	3.048	1.524		1.912	0.044
3	4.572	1.524		2.868	0.044
4	6.858	1.715		4.302	-0.075

- Part 2: Simulation of the transit time flowmeter in a bypass system

4.4 Geometry

The geometry is created in the ANSYS Design Modeler in 3D. Different settings performed in geometry and results for different settings of the entrance length, height of by-pass, the ratio of diameter, and the position from horizontal to vertical are illustrated.

The design modeler creates the main pipe of 1 inch diameter and 0.5 inch diameter of by-pass which is located at 5 inch entrance length and ends at the 3 inch to the end of main pipe (9 inch length). The radius of the elbow is 1.02 and the radius of connections of by-pass and main pass is 0.3. Using the Boolean, we can combine these two.

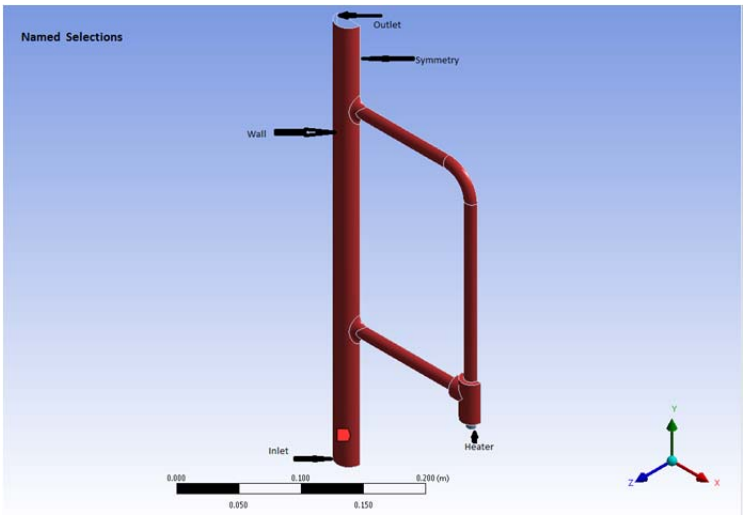

Fig.4.22 Named selections for boundaries.

4.5 Boundary Conditions and Parameter Settings

Through the boundary conditions the flow fields are different even if the governing equations are the same. The *no-slip* condition is the condition in viscous fluid in which there is no relative velocity between the surface and gas or fluid for a boundary condition

which means that the velocity is zero at the wall. The same boundary condition for the single pipe mentioned in above is also applied for both the main pipe and the by-pass. The mesh is generated using body size and patch conforming methods (Fig. 4.23).

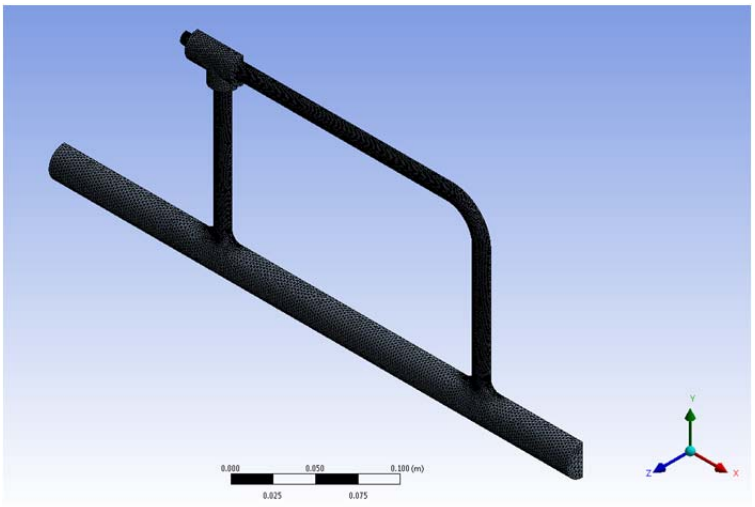

Fig. 4.23 Example of mesh preview in the horizontal pipe (ISO View).

The boundary conditions are shown in Table 4.4. The flow is turbulent in the main pipe. The spatial discretization was second-order upwind scheme for momentum and energy by applying Green-Gauss Node Based approach. The set of spatial discretization uses a simple scheme. The convergence absolute criteria are 10^{-6}. The total number of iteration is 3600.

Table 4.4 Summary of boundary conditions

Boundary	Type	Value
Main Inlet	Velocity inlet	$0.25-1.25\,m/s$
Outlet	Pressure outlet	$0\ Pa$
Wall	Wall	No Slip, Stationary wall
Symmetry		Symmetry

4.6 Verification and Validation of mesh results

The mesh size has the direct effect on the convergence and correct results, especially in calculating the velocity and the temperature. But doing simulation by more mesh size leads to time consuming running time and also the fluent has some limitations for the total element size of the mesh. So, we should select the right mesh so that it takes the correct data close to the boundaries which has the near zero velocity and in the middle of the pipe which has the highest velocity. For this reason we select the inflation layers from wall to take the slow velocity and using the on, curvature for the whole pipe. Since in the bypass the flow is laminar and slow, we may calculate the laminar boundary layer thickness by [3],

$$\delta = \frac{5x_1}{\sqrt{\mathrm{Re}_{x_1}}}$$

$$x_1 = r.\frac{\pi}{2} = \left(\frac{0.5*0.0254}{2}\right).\frac{\pi}{2} = 0.00997 \qquad (4.52)$$

$$\mathrm{Re} = \frac{\rho v D}{\mu} = \frac{998.2*0.0893*(0.5*0.0254)}{0.001003} = 1128.68$$

In the bypass pipe, by integration along the line $x_1 = 9.5$, the velocity will be $v = 0.4076\, m/s$. So,

$\delta = 0.00148 m = 0.06\, inch$

Note that the thickness for the mesh that we use in simulation should be more than this thickness.

For the main pipe that the flow is turbulent, by using Eq. (4.47), the turbulent boundary layer will be,

$$\delta = \frac{0.16 x_1}{\mathrm{Re}_{x_1}^{1/7}}$$

$$x_1 = \left(\frac{1*0.0254}{2}\right)*\frac{\pi}{2} = 0.019939$$

$$\mathrm{Re} = \frac{\rho v D}{\mu} = \frac{998.2*(0.40761885)*(1*0.0254)}{0.001003} = 10303.97$$

By integration along the line $x_1 = 9.5$, the velocity will be $v = 0.4076 m/s$ .So, $\delta = 8.5216697e-04m = 0.034 inch$

So we choose 0.0021 *m* for the total thickness of the laminar and turbulent flow, which is greater than the laminar and turbulent boundary layer thickness. Then we choose the 1.2 for growth rate as the default. If we use 10 layers for the maximum layers, then by Eqs. (4.48) and (4.49), the first layer thickness will be,

$S_1 = 8.0898\mathrm{e}\text{-}5\, m$

For different element size of mesh, we did the calculation of 0.001 absolute criteria. The solution data compared in the post processing and the finest mesh will be the highest value. If we fix the first layer thicknesses, then try different layers or growth rate, we can compare the best mesh.

We peak 10 layers with growth rate 1.2. There isn't much difference in this selection with the five layer growth rate 2 and twelve layer growth rates 1.2, but this one meets the mesh limitation with more layers which have a better convergence. So we can peak 10 layers with growth rate 1.2 and using the first layer thickness.

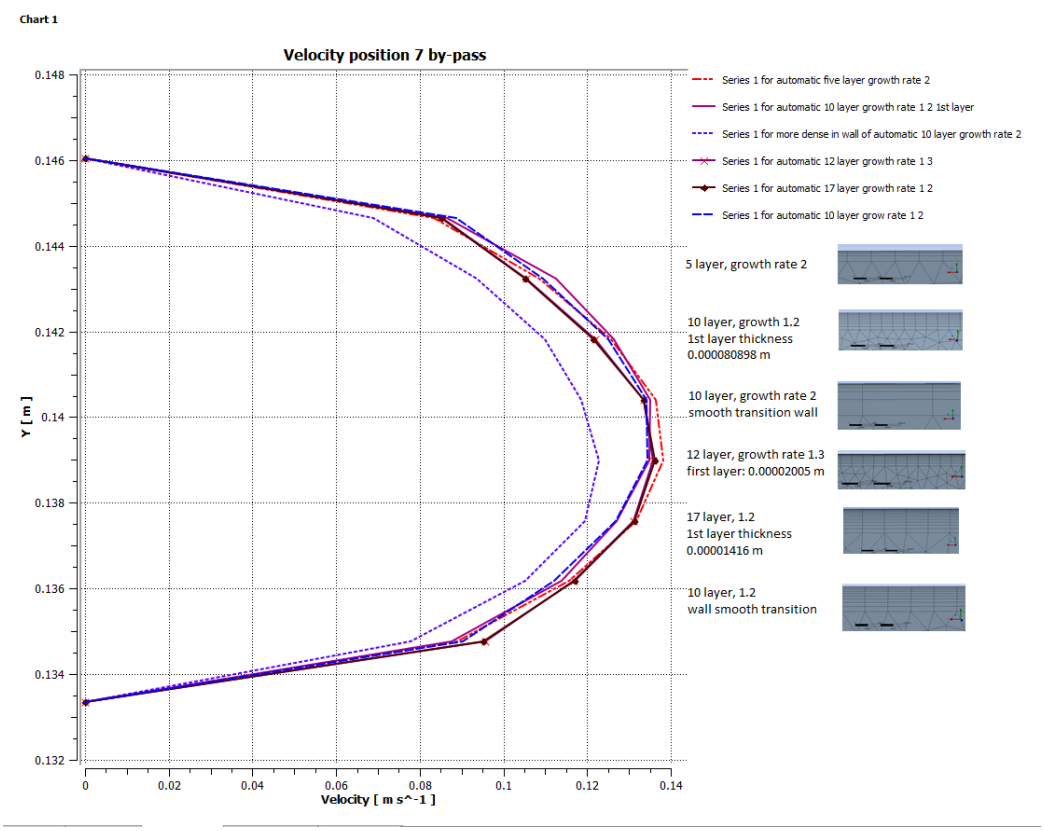

Fig. 4.24 Post processing comparison of different mesh size in bypass at position 7.

4.7 Results and Discussions

4.7.1 Velocity distribution in the pipe

Fluid velocity in a pipe is changing from zero at the surface to the maximum at the pipe center. That's because at wall there is a no slip condition which cause the velocity to be zero. They usually use average velocity which is constant when the cross section area is constant. For laminar pipe flow and fully developed flow, the average velocity is half of maximum velocity.

We are using the simulation to find the velocity in bypass because complexity of analytical solution for the ratio of velocities in the by-pass pipe to the main pipe leads to

numerical analysis which verifies the linearity between two velocities. The impact of bypass here is to reduce the velocity and increase the measurement range.

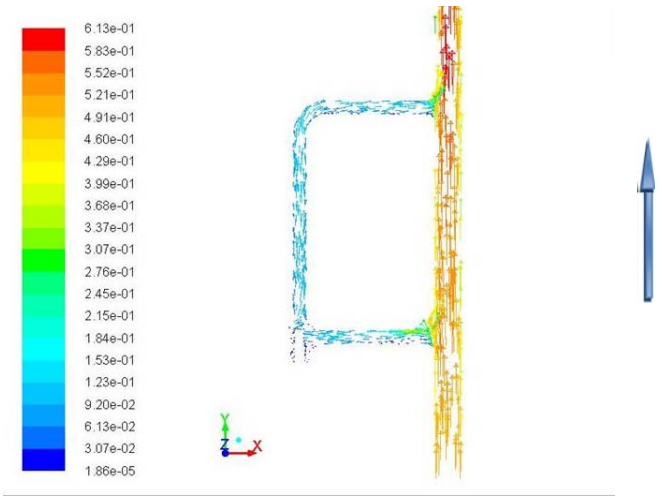

Fig. 4.25 velocity vectors colored by velocity magnitude (m/s)

4.7.2 Turbulent fluid velocity in a pipe

Turbulent velocity profile is based on the analysis and measurement, so in nature they are semi-empirical. If it is the time averaged velocity in the axial direction, then for the profiles in laminar flow we see the parabolic shape while for turbulent it is fuller and has a sharp edge near the pipe wall.

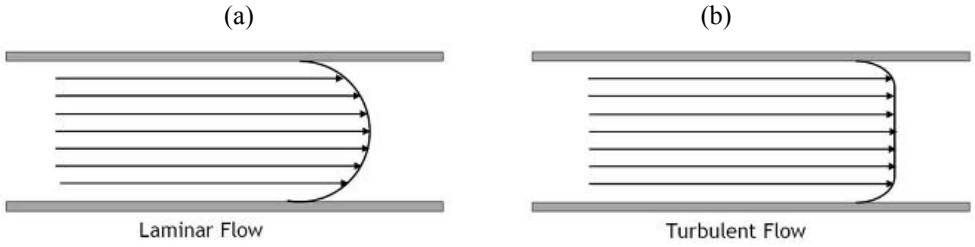

Fig. 4.26 Velocity profile comparison of laminar flow (a) and turbulent flow (b).

There are four sub-layers in turbulent flow. First, the very thin layer next to the wall is the viscous sub-layer in which the viscous effects are dominant. In this layer, the velocity profile is very linear and the flow is distinguished as to the streamlines. Second layer, is buffer layer which is next to the viscous sub-layer and the turbulent flow starts here while the flow affected mostly by viscous layer. Next, is the overlap or transition layer (inertial sublayer). Here, the turbulent effect is significant. In the next layer which is the turbulent layer or outer layer the turbulent effect is dominated and the viscous effect or molecular diffusion has the less effects. Turbulent flow characteristic is complicated and unlike the laminar flow we can't show an analytical relation for the velocity profile in entire flow.

The thickness of viscous sub-layer is so small and less that 1% of the pipe diameter but it involves large velocity gradients and plays an important role in flow characteristics. The velocity profile in this layer is linear with experiment confirmation. So, the velocity gradients remain constant in viscous sub-layer. That is, $du/dy = u/y$

So, the wall shear stress will be,

$$\tau_W = \mu \frac{u}{y} = \rho \nu \frac{u}{y} \qquad (4.53)$$

Or,

$$\frac{\tau_W}{\rho} = \frac{\nu u}{y} \qquad (4.54)$$

where y is the distance from the wall.

The square root of $\frac{\tau_W}{\rho}$ has the velocity dimensions. And the friction velocity expressed as, $u_* = \sqrt{\frac{\tau_W}{\rho}}$, (4.55)

Substituting this for the viscous sub-layer gives,

$\frac{u}{u_*} = \frac{yu_*}{\nu}$. This equation is the law of the wall, for $0 \le yu_*/\nu \le 5$, the thickness of the viscous sub-layer is

$$y = \delta_{sublayer} = \frac{5\nu}{u_*} = \frac{25\nu}{u_\delta} \qquad (4.56)$$

where u_δ is the flow velocity at the edge of viscous layer and it is proportional to the average velocity in a pipe. As a result, the thickness of viscous sub-layer is proportional to the kinetic viscosity and inversely proportional to the average flow velocity. So, as the velocity increases, the viscos sub-layer decreases and becomes thinner. So, the velocity profile becomes flat and velocity distribution at high Reynolds number will be more uniform.

If we want to undimensionalize the distance *y* from the surface the viscous length should be used for the dimensions of length ν/u_*.

The undimensionalized variables are denoted by, $y^+ = \frac{yu_*}{\nu}$, $u^+ = \frac{u}{u_*}$ and the normalized law of the wall, $u^+ = y^+$. Here for normalized *y* and *u*, we use the friction velocity u_*. Also y^+ resembles the Reynolds number expression [1].

4.7.3 Laminar and Turbulent Flows in pipes and Reynolds Number

-Laminar flow

The smooth streamlines and highly ordered motion is considered to be laminar. In laminar flow, the flow is in organized way along the line in which the flow passes. The momentum and energy are transferring in laminar flow by molecular diffusion. The

Reynolds number for this case is less than 2300. Laminar flow and long pipe make the entrance length negligible. By applying the momentum balance to a differential volume element, we can obtain the momentum equation and by solving this we can obtain the velocity profile and use it to obtain a relation for the friction factor. For the laminar flow the velocity profile remains unchanged in the axial direction. So, each fluid particle's velocity is constant along the streamline. A ring-shaped differential volume element has a radius of *r*, a thickness *dr*, and a length *dx* which oriented coaxially with the pipe. The fully developed flow in a horizontal pipe can be obtained by,

$$\left(2\pi r\, dr\, P\right)_x - \left(2\pi r\, dr\, P\right)_{x+dx} + \left(2\pi r\, dx\, \tau\right)_r - \left(2\pi r\, dx\, \tau\right)_{r+dr} = 0 \qquad (4.57)$$

The balance between viscous and pressure forces exists for a horizontal pipe in a fully developed flow. So by rearranging the above equation we get,

$$r\frac{P_{x+dx} - P_x}{dx} + \frac{\left(r\tau\right)_{r+dr} - \left(r\tau\right)_r}{dr} = 0 \qquad (4.58)$$

Taking limit and $dr, dx \to 0$: $$r\frac{dp}{dx} + \frac{d\left(r\tau\right)}{dr} = 0 \qquad (4.59)$$

Since $\tau = -\mu\left(du/dr\right)$ taking μ constant, the desired equation will be,

$$\frac{\mu}{r}\frac{d}{dr}\left(r\frac{du}{dr}\right) = \frac{dp}{dx} \qquad (4.60)$$

The right hand side is constant and can be obtained by writing a force balance on a volume element of radius *R* and thickness *dx*,

$$\frac{dP}{dx} = -\frac{2\tau_w}{R} \qquad (4.61)$$

In the fully developed region the viscosity and the velocity profile are constants. So τ_w is also constant. We can conclude that *dP/dx* = constant. So, if we integrate two times, the velocity profile $u(r)$ will be obtained by,

$$u(r) = \frac{1}{4\mu}\left(\frac{dP}{dx}\right) + C_1 \ln r + C_2 \qquad (4.62)$$

By applying the boundary conditions and the no slip condition for the pipe and considering symmetry geometry surface, and:

$\partial u / \partial r = 0 \; at \; r = 0$

$u = 0 \; at \; r = R$

We get,

$$u(r) = -\frac{R^2}{4\mu}\left(\frac{dP}{dx}\right)\left(1 - \frac{r^2}{R^2}\right) \qquad (4.63)$$

Therefore, the velocity profile is parabolic in a pipe flow and in fully developed region. The maximum velocity is at centerline and the minimum velocity is at the pipe wall. For any *r*, the axial velocity is positive. Since there is viscous effect, pressure decrease in flow direction and so the axial pressure gradient *dP/dx* must be negative. The average velocity can be obtained by,

$$V_{avg} = \frac{2}{R^2}\int_0^R u(r) r dr = \frac{-2}{R^2}\int_0^R \frac{R^2}{4\mu}\left(\frac{dP}{dx}\right)\left(1 - \frac{r^2}{R^2}\right) r \, dr = -\frac{R^2}{8\mu}\left(\frac{dP}{dx}\right) \qquad (4.64)$$

By combining the last two equations, the velocity profile can be determined from the flow rate information,

$$u(r) = 2V_{avg}\left(1 - \frac{r^2}{R^2}\right) \qquad (4.65)$$

The maximum velocity is at the centerline, $r = 0$,

$$u_{\max} = 2V_{avg} \tag{4.66}$$

We see that in fully developed pipe flow for laminar case, the average velocity is half of the maximum velocity.

-Turbulent flow

In turbulent flow the flow has random fluctuations of swirling regions of fluid which called eddies. So the momentum and energy transfer by swirling eddies to different regions are more rapidly than laminar flows which transfer these by diffusion and across streamlines.

The flow regime depends on the ratio of inertial forces to viscous forces in the fluid which is called the Reynolds number (dimensionless) and for a circular pipe we have,

$$\mathrm{Re} = \frac{Inertial\ forces}{Viscous\ forces} = \frac{V_{avg} D}{\nu} = \frac{\rho V_{avg} D}{\mu} \tag{4.67}$$

where V_{avg} is the average flow velocity (*m/s*), D is the diameter (m), $\nu = \frac{\mu}{\rho}$ is the kinematic viscosity of fluid (m^2/s), and μ is the dynamic viscosity of fluid (*kg/m.s*).

The hydraulic diameter for circular pipes is, $D_h = \frac{4A_c}{P} = \frac{4\left(\pi D^2/4\right)}{\pi D} = D$, where A_c is the cross-sectional area of the pipe, and P is the wetted perimeter of the pipe. The transition from laminar to turbulent flow depends on the geometry, surface roughness, flow velocity, surface temperature, and type of fluid. The flow in a circular pipe is laminar for Re ≤2300. It is turbulent for Re≥ 4000. The flow is transitional between 2300≤Re≤4000. In transitional flow, the flow is randomly changed between laminar and turbulent.

4.7.4 Condition in bypass

For the slower flow rate in main pipe, the Reynolds number in bypass is laminar, and for the higher Reynolds number the flow in bypass, up to 10 GPM , the flow is transitional and enters the turbulent. The Reynolds number of bypass for different inlet velocities of main pipe is shown in Table 4.5.

Table 4.5 Reynolds number in bypass

Inlet *V* (*m/s*)	Re in bypass
0.25	507.3
0.5	1099.5
0.75	1844.4
1	2677.1
1.25	3437.9

4.7.5 Impact of different ratios of diameters

Assume that the flow in the main pipe is turbulent. To pick the right diameter for the bypass pipe, we choose the diameter of 1 inch for the main pipe. Then we get the results when the ratio of bypass to main-pass pipe is 0.5, 0.75, and 1. For the different inlet velocities (0.25-1.25 *m/s*) the results is linear for the three ratios. Also as expected the highest velocity comes with the larger ratio.

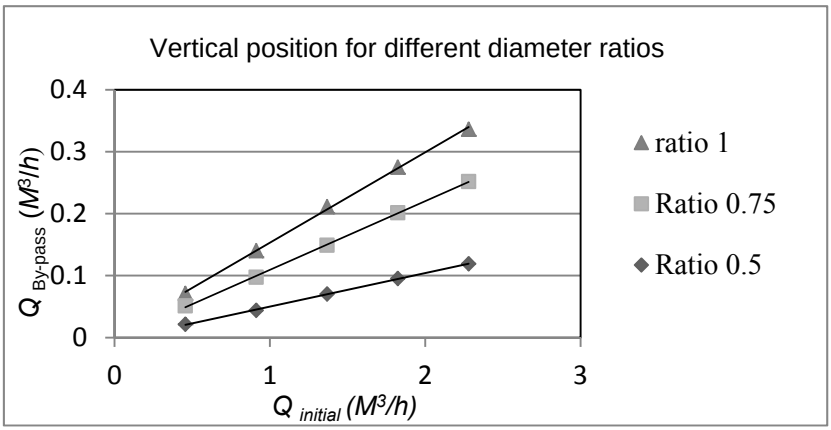

Fig. 4.27 The effect of different diameter ratios

4.7.6 The theory of entrance region

When a fluid is entering a circular pipe with a uniform velocity, due to no slip condition, at the surface of the pipe the fluid particles goes to a complete stop. In this layer the fluid particles slow down as a result of friction. Since the mass flow rate through the pipe is going to keep constant, the velocity of the fluid at the midsection has to increase. So a velocity gradient develops along the pipe. The flow in a pipe divides into two regions: the boundary layer region and the irrotational flow region (core region). In the boundary layer region the viscous effects and the velocity changes are significant. In the irrotational flow region the frictional effects are negligible and the velocity remains essentially constant in the radial direction. The thickness of the boundary layer increase in the flow direction until reaches the pipe center. The region from the pipe inlet to the point at which the boundary layer merges is called the hydrodynamic entrance region and the length of this region is called the hydrodynamic entry length L_h. And since this is the region that the velocity profile develops, flow in the entrance region is called hydrodynamically developing flow. The region beyond the entrance region in which the velocity profile is fully developed and after that it doesn't change, called the hydrodynamically fully developed region. Another definition for fully developed region is when the normalized temperature profile remains unchanged. When the fluid in the pipe is not heated or cooled and the temperature remains constant then the hydrodynamically developed fluid is the same as fully developed flow.

In laminar flow the velocity profile in the fully developed region is parabolic but in turbulent flow it is fuller or flatter because of the eddy motion and more vigorous mixing

in the radial direction. In fully developed flow the time- averaged velocity profile remains unchanged and the hydrodynamically fully developed will be,

$$\frac{\partial u(r,x)}{\partial x} = 0 \rightarrow u = u(r) \qquad (4.68)$$

In the hydrodynamically fully developed region, when the velocity profile remains unchanged, the wall shear stress remains constant as well. In a hydrodynamic entrance region of the pipe, the pipe shear stress is highest at the pipe inlet because the thickness of the boundary layer is smallest. This thickness decreases gradually to the fully developed value. So the pressure drop is higher in the entrance region of the pipe. And the entrance region is increasing the average friction factor for the entire pipe if the pipe is short but it is not significant for the long ones [1].

4.7.7 Entry length

The hydrodynamic entry length is the distance from the pipe entrance to where the wall shear stress and the friction factor is the value of the two percent of fully developed value.

The hydrodynamic entry length for laminar flow is approximately given by,

$$L_{h,laminar} \cong 0.06\,\mathrm{Re}\,D \qquad (4.69)$$

The hydrodynamic entry length for turbulent flow is,

$$L_{h,turbulent} = 4.4D\,\mathrm{Re}_D^{1/6} \qquad (4.70)$$

The entry length in turbulent flow is much shorter and it is less dependent on the Reynolds number. In turbulent flows beyond a pipe length of 10 diameters, the effect of entrance length is insignificant and the hydrodynamic entry length is approximated by [1],

$$L_{h,turbulent} \approx 10\,D \qquad (4.71)$$

By using this formula for turbulent flow the entry length will be 22 meters. For the length of 17 inch and the installation convenience we choose the entrance length from the simulation results.

4.7.8 Impact of entrance length L

The theory of the entrance length and the calculation of the entry length are considered in order to explain the simulation results. To choose an appropriate location where the bypass pipe is positioned, we examine a different set of entrance lengths. The corresponding computed flow rates ratios are brought in Fig. 4.28. As we can see there is a linear relationship between the flows in the bypass and main-pass pipes. This confirms that the flow in the main-pass pipe can be obtained from the bypass flow, regardless the range of flow. Also, it is seen that the trends from 3 to 6 inches are likely overlapped and unlike the others there is no jump in this range. Therefore, we choose the entrance length of 5 inches.

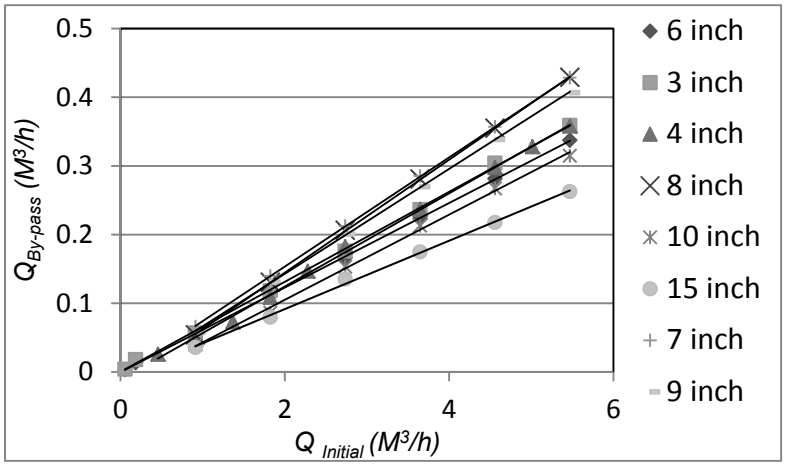

Fig. 4.28 The computed bypass flow rates versus main-pass flow rates for different entrance lengths.

4.7.9 Impact of the bypass height

In this experiment, to choose the length of arm in the bypass pipe we compared the results of flow rate ratios for five different lengths vertical configuration. The results are shown in Fig.4.29. As seen from this Figure, since the lengths of 5.5, 7 and 8 inches have too close ratios, we picked the 5.5 inch length for the computer simulations.

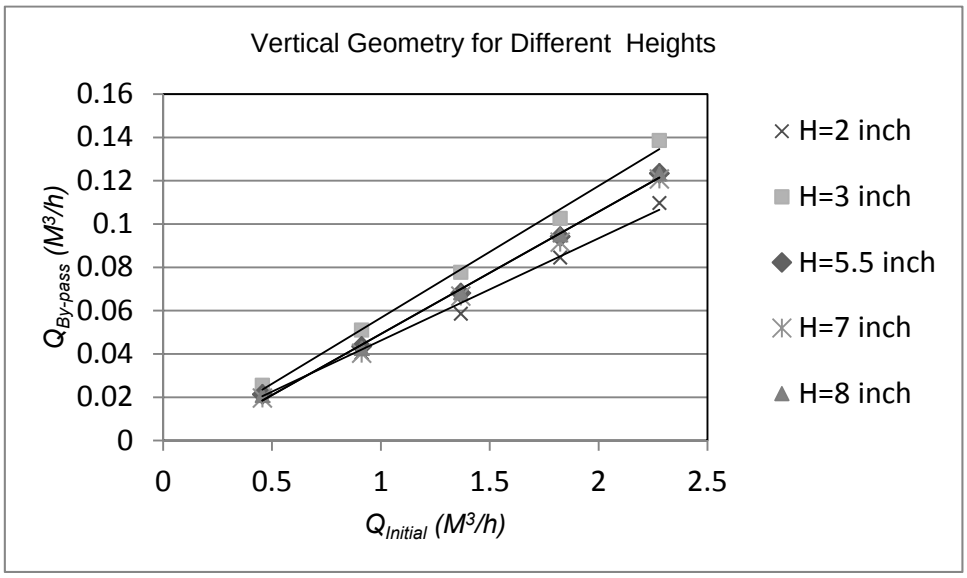

Fig. 4.29 The computed by-pass flow rates versus main-pass flow rates for different length of the vertical arm in the bypass pipe.

4.7.10 Impact of different angle

To estimate the ratio between the flow rates of water drawn through the by-pass route to the flow rate passing through the main pipe, we consider different by-pass configurations with different angles. We investigate this ratio for five different angels: 0, 15, 45, 75, and 90 degree and performed simulation runs for different initial flow rates

from 0.45 to 2.28 m^3 / h . The results are brought in Fig. 4.30. As one can see, this ratio is quite the same with respect to the pipe angle.

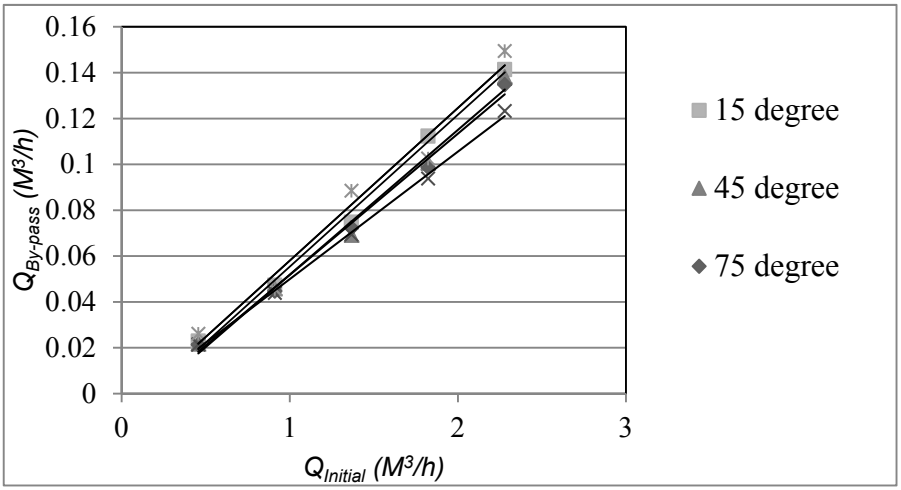

Fig. 4.30 The ratio between the bypass flow and main-pass flow.

By using the tangent degree we can calculate the velocity in the middle of by-pass that has an angle with the horizontal plane.

For 15 degree, the tan15=0.27. In fluent for the solution xy plot input the 1 for x direction and 0.27 for y direction so that y/x equals 0.27. Also repeat for 75 degree which has tangent of 3.73.

As seen in above figure. The results show linearity for the all degrees. The linearity is obvious for 75 degree and the initial velocity of V=0.5 m/s. For small pipe velocity at the centerline is shown in figure 4.31.

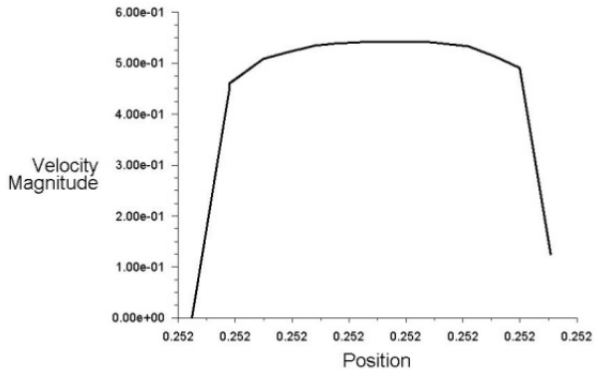

Fig. 4.31 Velocity plot in the centerline of the bypass.

To measure the reliability of obtained ratio, we used the following deviation equation,

$$\sigma = \frac{Q_{\max} - Q_{\min}}{Q_{in}} \qquad (4.72)$$

where $Q_{\max}$ and $Q_{\min}$ are, respectively, the maximum and minimum flow passing through the by-pass pipe, and Q_{in} is the initial flow rate passing through the main pipe.

The results are shown in Fig. 4.32 which obtained from Table 4.6 in which for different flowrates in by-pass we are finding the flowrate in main pipe using Alfa and Beta in the linear equation of each angle design (flow rate ratio of bypass to main pipe). We see that the relative deviation of obtained ratio is less than 8% which means that this ratio does not dependent on the angle of the by-pass pipe with the main-pass pipe.

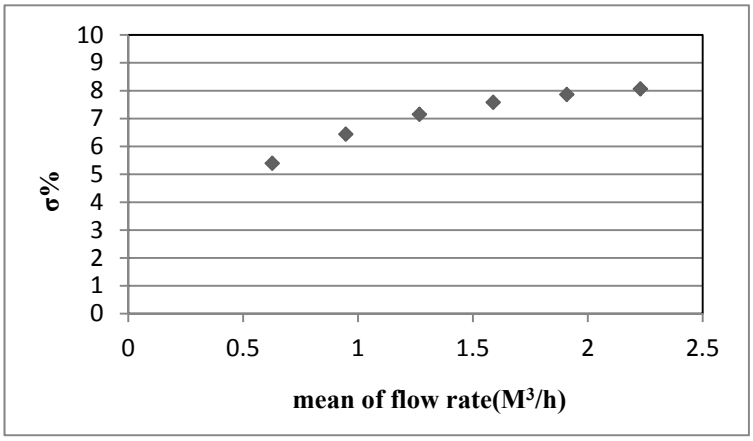

Fig. 4.32 The relative deviation of the ratio between the by-pass flow and main-pass flow.

Table 4.6 Line fitted to different angles

Angels	Line
0	y = 0.0666x - 0.0086
15	y = 0.0663x - 0.0109
45	y = 0.0663x - 0.0109
75	y = 0.0616x - 0.0098
90	y = 0.0556x - 0.0057

Table 4.7 Calculation of Sigma over the average flow rates

Angels	Beta	Alfa	Bypass flowrate 0.03	Bypass flowrate 0.05	Bypass flowrate 0.07	Bypass flowrate 0.09	Bypass flowrate 0.11	Bypass flowrate 0.13
0	0.0086	0.0666	0.579	0.879	1.180	1.480	1.781	2.081
15	0.0109	0.0663	0.617	0.918	1.220	1.522	1.824	2.126
45	0.0113	0.0632	0.647	0.964	1.280	1.597	1.913	2.229
75	0.0098	0.0616	0.646	0.971	1.295	1.620	1.945	2.269
90	0.0057	0.0556	0.642	1.002	1.362	1.721	2.081	2.441
MAX			0.647	1.002	1.362	1.721	2.081	2.441
MIN			0.579	0.879	1.180	1.480	1.781	2.081
Qmax-Qmin/Qinitial			5.39E+00	6.44E+00	7.15E+00	7.58E+00	7.86E+00	8.07E+00
Average			0.626	0.947	1.267	1.588	1.909	2.229

4.7.11 Pressure distribution in the pipes

Water flows through the bypass pipe due to pressure loss along the main-pass pipe as predicted in the following equation,

$$\Delta P = f_D \frac{L}{D} \frac{\rho V^2}{2} \tag{4.73}$$

where ΔP is the pressure loss $(Pa \, or \, kg/ms^2)$, f_D is the friction factor (unitless), L/D is the length/diameter of the pipe, ρ is the density of fluid (kg/m^3), and V is the mean velocity of flow (*m/s*).

Friction Factor:

$$f_D = \frac{64}{R_e} \quad , \qquad \text{Laminar flow} \tag{4.74}$$

$$f_D = a + b(R_e)^{-c}, \text{ Turbulent flow} \tag{4.75}$$

where

$$\begin{aligned} &a = 0.094k^{0.225} + 0.53k \text{ , From Moody Diagram} \\ &b = 88k^{0.44} \\ &c = 1.62k^{0.134} \\ &k = e/d \text{ , Relative Roughness} \end{aligned} \tag{4.76}$$

For the commercial steel and 1 inch diameter we have: relative roughness of 0.002, $k = 0.002$, $a = 0.02428$, $b = 5.71394$, $c = 0.70445$.

To verify these equations, we conducted a simulation of the flow over a flow range from 0.45 to $2.28 \, m^3/h$. By calculation, the pressure loss in the main-pass pipe with diameter $D = 1$ inch, length $L = 15$ inch, and average velocity $\overline{V} = 0.5 \, m/s$, Reynolds number $\mathrm{Re} = 12639.22$, and friction factor $f_d = 0.02428 + 5.713943(\mathrm{Re})^{-0.704455} = 0.03165$, ΔP will be 59.24 *Pa.* The results are shown in Fig. 4.33. As seen, the simulation results

confirm the theoretical prediction. The second experiment is to investigate the pressure loss due to the bypass-pipe. As shown in Fig. 4.34 the pressure drops along the main pipe is not markedly changed when the by-pass system is added to the system.

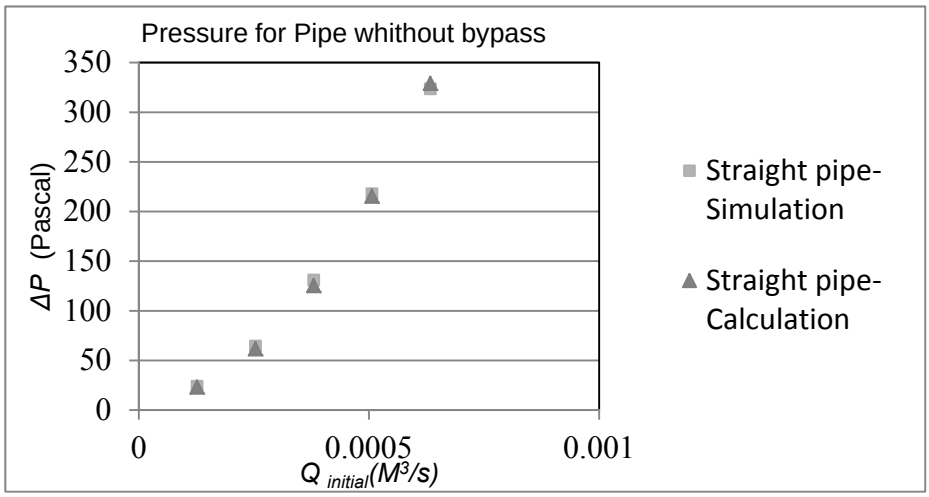

Fig. 4.33 The pressure along the main-pass pipe for velocity of 1 m/s for a pipe simulation and calculation.

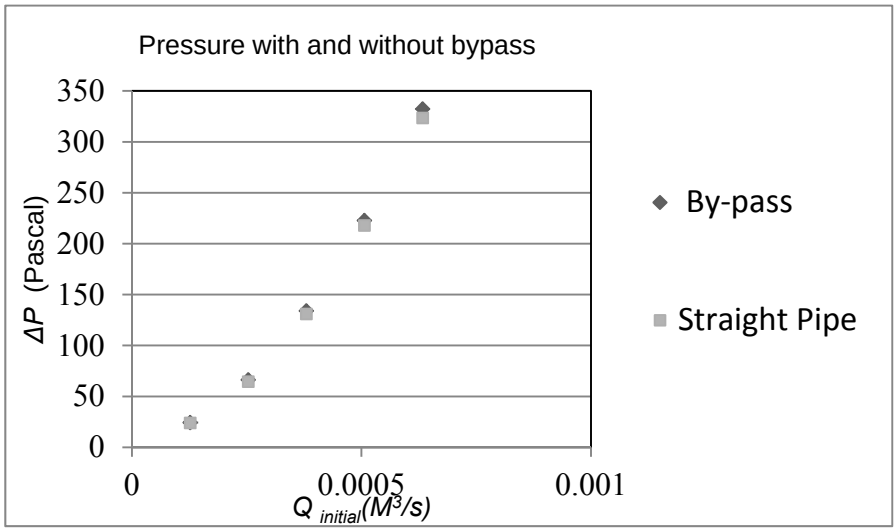

Fig. 4.34 The pressure along the main-pass pipe for velocity of 1 m/s with bypass and without bypass.

Table 4.8: Pressure distribution along the pipe (with and without bypass) using simulations

Calculated pressure using by-pass					
V m/s	Qinitial (M3/s)	Re	Y=16 inch	Y=1 inch	ΔP
0.25	0.00013	6319.61	1.36	25.73	24.37
0.5	0.00025	12639.2	3.25	69.55	66.31
0.75	0.00038	18958.8	6.91	141.00	134.08
1	0.00051	25278.4	11.60	234.47	222.86
1.25	0.00063	31598.1	16.95	349.27	332.31
Calculated pressure using pipe without by-pass					
V m/s	Qinitial (M3/s)	Y=16 inch	Y=1 inch	ΔP	(ΔPbypass-Δppipe)/Δpb
0.25	0.00013	1.27	25.41	24.13	0.97%
0.5	0.00025	3.454	68.08	64.64	2.59%
0.75	0.00038	6.796	137.97	131.17	2.22%
1	0.00051	11.205	229.15	217.95	2.26%
1.25	0.00063	16.648	340.26	323.62	2.69%

Table 4.9 Pressure distributions along the straight pipe using calculations and compare with simulation.

V (*m/s*)	Re	*Fd*	ΔP	(Δ*P*cal-Δ*Pp*)/ Δ*Pp*
0.25	6319.61	0.050	23.39	3.17%
0.5	12639.22	0.033	61.76	4.65%
0.75	18958.83	0.030	125.57	4.46%
1	25278.44	0.029	215.63	1.08%
1.25	31598.05	0.028	329.23	-1.70%

4.7.12 Temperature distribution along the pipes

For velocity 0.5 *m/s*, we pick different points in the bypass and calculate the temperature. In this simulation the pipe is horizontal, the heat generation rate is 4.179414e+08 (W/M^3). Using transient time and turn on the heater for one second and defining not periodic condition in profile, the profile would be written as:

((heater transient 4 0 0)

(time

0.000 1.000 1.001 2.000)

(source

4.179414e+08 4.179414e+08 0.000000e+00 0.000000e+00)

)

From the signal processing point of view, to able to detect the delay point by signal processing algorithms, the temperature change must be at least 0.5 degree in one second. Fig. 4.35 helps us to find the best position for thermocouples in the bypass. By picking the arbitrary points in the bypass and knowing that the heater is located at $x = 5.375$ inch the simulation results are compared with calculation. As we can see Point 5.5 which is close to the heater has some variation because of the cold water is arriving to the point, the variation in temperature makes it unsuitable to place the thermocouple at this location. Point 7, 9, 11 and 12 are suitable positions for the signal processing algorithm.

There is a response time at the beginning of each plot, and that can be calculated. Since we have the distance of each point and we can calculate the velocity of each point from simulation results, so the response time calculated in Table 4.10 and the results confirm Fig. 4.36.

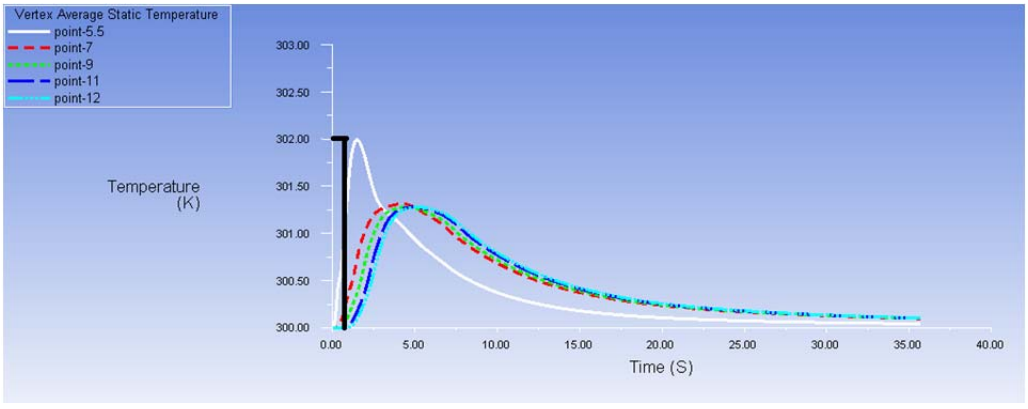

Figure 4.35 Temperature distributions at different position of bypass.

Table 4.10 Calculation of the response time of each thermocouple

Point	Distance from heater (*m*)	*V* (*m/s*)	Response time (*s*)
5.5	0.003	0.039	0.078
7	0.041	0.135	0.303
9	0.092	0.145	0.633
11	0.143	0.149	0.958
12	0.168	0.150	1.120

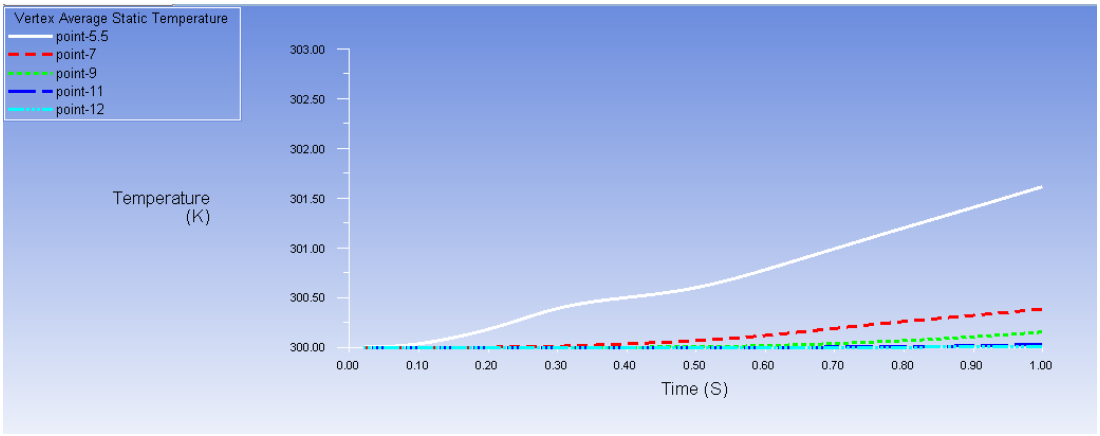

Figure 4.36 Response time at different TC locations.

If we have the temperature rise time, then we can obtain the heat generation rate in terms of watt, by knowing mass flow rate from the average velocity cross section at each point. For example for point $x = 5.5$, $\overline{V} = 0.0352$ and inlet velocity 0.5 *m/s* , using following equations, we have,

$$\Delta T \times \dot{m} \times C_P = Power \qquad (4.77)$$

$$\dot{m} = \overline{V}.A.\rho \qquad (4.78)$$

Where ΔT is the temperature rise time calculated by the Fluent, C_P is the specific heat capacity, and $\dot{m}$ is the mass flow rate, and $\overline{V}$ is the average velocity at the cross section of location 7 in the bypass pipe.

$$1.993 \times 0.0044 \times 4182\, j/kg - k = 36.67\ \ Watt$$

And,

$$\dot{m} = 0.0352\,\frac{\pi(0.5\times 0.0254)^2}{4}\times 998.2 = 0.0044\,\text{kg/s}$$

If we extract the data of Figure 4.35 in word the difference of temperature is exactly: 1.993 *K*

From equation (4.77) we can calculate the power of heater in watt which is in reality is 36.67 Watt.

4.7.13 Flow rate calculation using signal processing method

Considering point 7 and point 11 for the bypass, in transient time, if the heater is one second on and six second off for the inlet velocity of 0.75 *m/s*, the time delay can be calculated by,

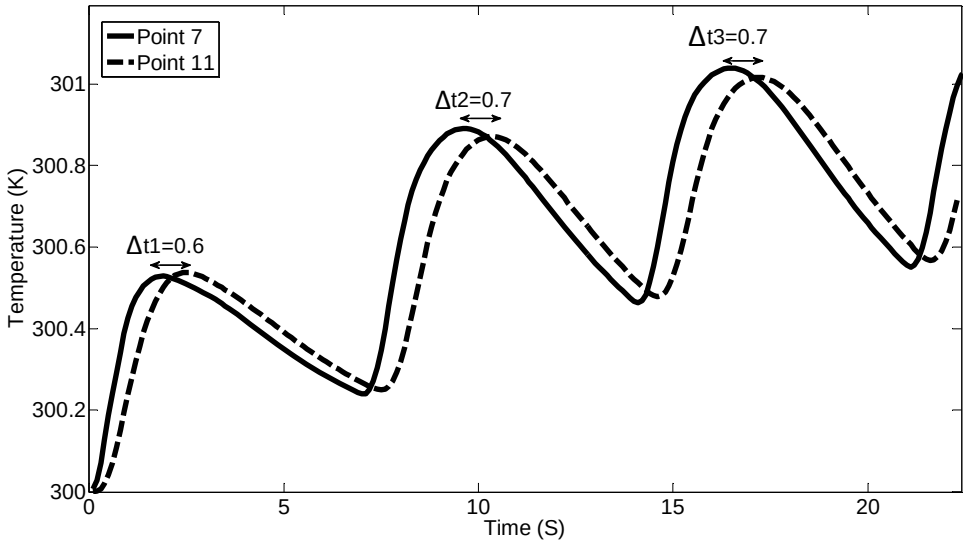

Fig 4.37 The time delay of two signals 1 second heater on and 6 second off

By extracting data from the Fluent for the first pick we have,

- Point 7: 1.9 s 300.5 K Point 11: 2.5 s 300.5 K
- $\Delta t_1 = 0.6\,s$

For the second pick:

- Point 7: 22.8 s 300.8 K Point 11: 23.5 s 300.8 K
- $\Delta t_2 = 0.7\,s$

From simulation for position 7 if we suppose that there is a maximum velocity at the centerline of the pipe and there is an average velocity in cross section position from these two we can catch the constant Alfa here for $V = 0.75\,m/s$ by,

$$\frac{V_{Max}}{\overline{V}} = \alpha \qquad (4.79)$$

Using area weighted average for a cross sectional plane or midline, we get,

$\overline{V} = 0.17\,m/s$

Using vortex average for point 7 in the centerline, we get,

$V_{Max} = 0.21 m/s$, so

$\alpha = 1.23 \approx 1.2$

In this case the flowrate will be,

$$Q = A\overline{V} = 0.00013(0.17) = 2.2e-05\,(m^3/s) = 0.08\,(m^3/h)$$

From signal processing, by having the two thermocouples 4 inch away at positions 7 and 11, the flow rate will be calculated by,

$$Q = \overline{V}.A = \frac{L}{\Delta t}A = \frac{4\times 0.0254m}{0.6\,s}\frac{3.14\left(0.5\times 0.0254\right)^2}{4} = 2.2e-05\,(m^3/s) = 0.08\,(m^3/h)$$

For the range of the 2 GPM to 10 GPM, the simulation results are shown in Table 4.11 in which the data are from the most accurate mesh with the element size of 0.0009. At position 7 in bypass we used the integral along the line from simulation results.

Table 4.11 Simulation data for different velocities

V (m/s)	Q Initial (M^3/h)	V at x=7 Bypass (m/s)	Q bypass at x=7 (M^3/h)
0.25	0.46	0.055	0.025
0.5	0.91	0.104	0.047
0.75	1.37	0.166	0.076
1.00	1.82	0.227	0.103
1.25	2.28	0.285	0.130

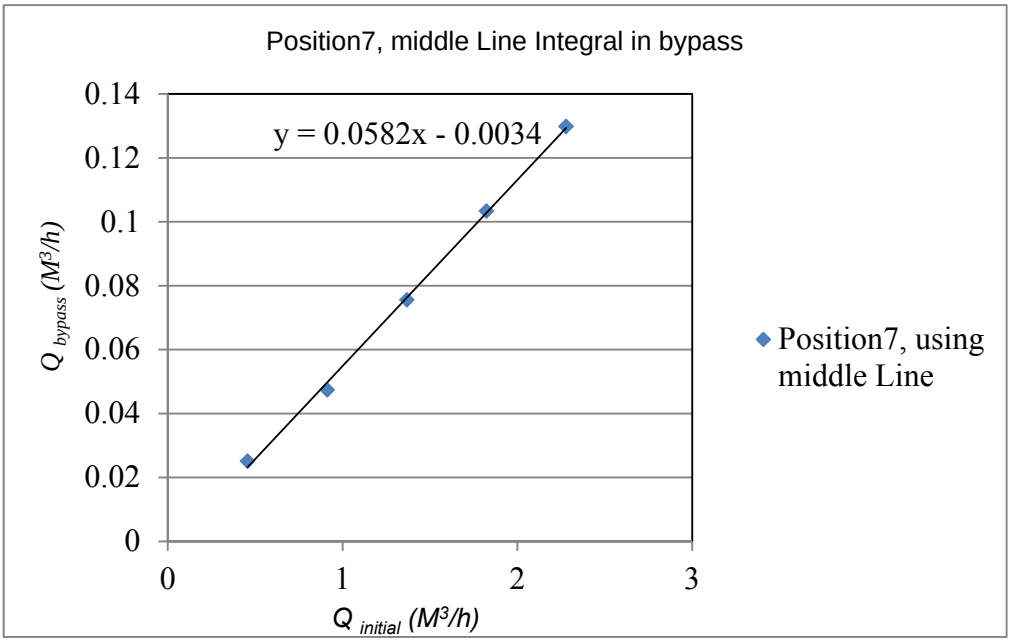

Fig 4.38 Linearity of bypass to mainline from table 4.11.

We can calculate the error measurement in Fig. 4.38 from the following equation,

$$error = \sqrt{\frac{\left(Q_{bypass} - \hat{Q}_{bypass}\right)^2}{N}} \qquad (4.80)$$

$\hat{Q}_{bypass}$ can be calculated from the line $y = 0.0582x - 0.0034$, by putting the initial flow rate instead of *x*, the bypass flowrate can be calculated from the simulated velocity at position 7. The results are reported in Table 4.12.

Table 4.12 Error measurement data calculation.

V (*m*/s)	*Q* initial (M^3/*h*)	$\hat{Q}_{bypass}$	Q_{bypass}	Q_{bypass} - $\hat{Q}_{bypass}$	(Q_{bypass} - $\hat{Q}_{bypass}$)^2
0.25	0.456	0.023	0.025	0.0019	3.815e-06
0.5	0.912	0.050	0.047	0.0023	5.177e-06
0.75	1.367	0.076	0.075	0.0006	3.664e-07
1	1.823	0.103	0.103	0.0006	4.101e-07
1.25	2.279	0.129	0.130	0.0006	3.351e-07
SUM					1.010e-05
SUM/5					2.021e-06
(SUM/5)^0.5					0.0014

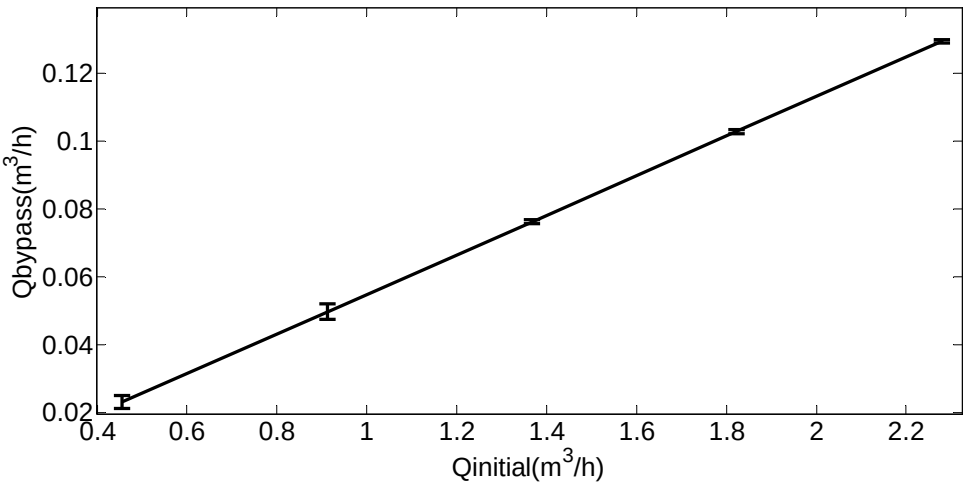

Fig 4.39 Error bars showing the errors at each points

If we check the convergence of the results to see how correct are the calculations, we see enough convergence achieved by reporting the flux, and calculate the mass flow rate

for inlet and outlet. It should be a very small amount. Here $\frac{Net\,\mathrm{Re}\,sults}{inlet/outlet} = 3.5e-08$ this is small and less than 0.2% showing the accuracy of the results.

4.8 Simulations of Experimental setup

4.8.1 Geometry and Mesh

In this experiment, as we can see in Fig. 4.40, the dimensions of bypass height and arm are 4.6 and 11 inch. The other dimensions are the same as before.

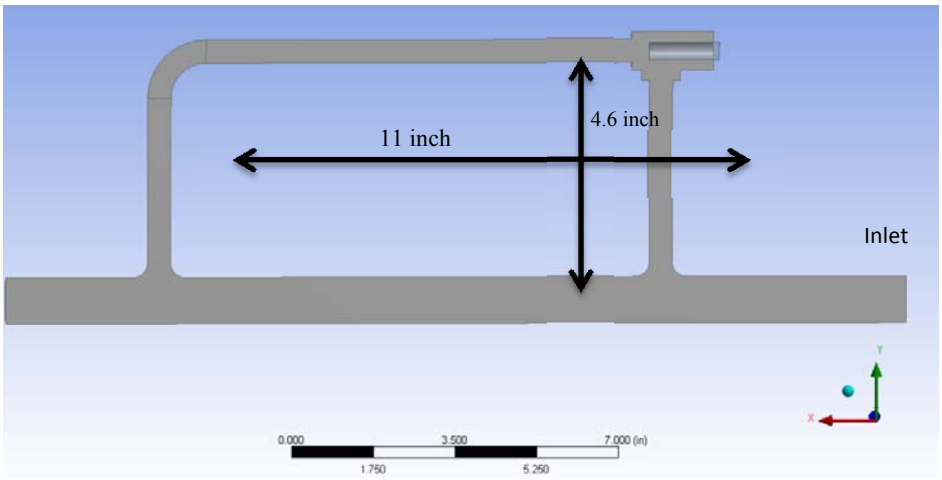

Fig 4.40 Simulation geometry used for experiment.

For the mesh part, as mentioned earlier, 10 layer of the inflation layer with the growth rate of 1.2, and the first layer thickness of 8.0898e-05 *m* is used.

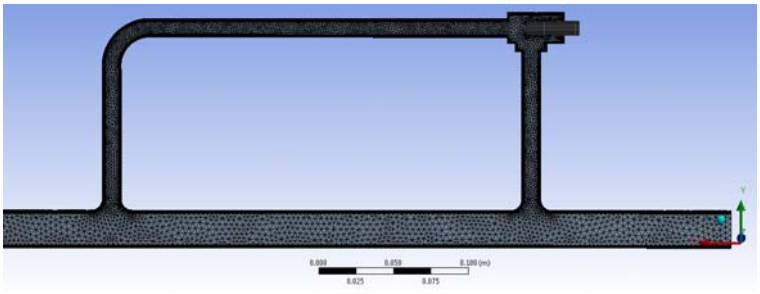

Fig 4.41 Mesh using the inflation layer from the wall and calculate the first layer thickness.

4.8.2 Results and Discussions

We run the simulation for the steady state and transient for the velocity of 1 GPM. The Reynolds number will be 3147.2 which shows that the fluid is in transition mode. The two thermocouples are located along the bypass at 8.25 inch and 13.25 inch points. From the steady state we can calculate the velocity at bypass first TC location and the flow rate. Finally the ratio of bypass flowrate to the initial flowrate is calculated. From the transient simulation, we can find the time delay between the two thermocouples by using time step of 0.1. The distance of the two thermocouples is five inch. So the velocity is calculated and from that the bypass flowrate is obtained. From the ratio of steady state, the initial flowrate can be calculated. Also the initial flowrate equals to the flowrate in the bypass plus the flowrate in the main-pass which confirms the results.

Table 4.13 Ratio calculation of by-pass flowrtae to initial flowrate in steady state condition.

V (m/s)	$Q_{initial}$ (M^3/h)	TC1 (m/s)	$Q1$ (M^3/h)	$Q_{bypass}/Q_{initial}$	Q_{bypass} (time delay) GPM	$Q_{initial}$ GPM	Main-pipe (m/s)	Q_{main} (M^3/h)	$Q_{ini}=Q_{main}+Q_{by}$
0.1245	0.227	0.0293	0.0134	0.059	0.047	1.05	0.116	0.212	0.226

For transient time and time step 0.01,

$$\Delta t = 5.38\,s$$

$$X = 0.127\,m \;\; BTW \;\; TCs$$

$$V = \frac{0.127}{5.38} = 0.02361\ m/s$$

$$Q = V.A = 0.02361 \times 1.267e-4 = 2.99e-06\,(m^3/s) = 0.047\ GPM$$

CHAPTER 5

CONCLUSIONS

Based on the correlated thermal signals a flowmater is designed. Computer simulations are performed and the results confirm the real experiments. Due to the limitations such as short response time of thermal sensor and need of strong heating signals, we present a solution by using a bypass system in which a small fraction of flow is measured along with the smaller velocity and hence increasing the range of the measurement. In this case, using a smaller diameter of the bypass helps to reduce the electrical power consumption. Also, the pressure drop in the bypass pipe is insignificant. We examined the performance of the system for different angles, entrance lengths, and heights. A linear relationship between the bypass and main flow is obtained for a range of turbulent flow up to $2.28\, m^3 / h$. We obtained the temperature distribution for each sensor and calculate the time delay. Therefore, by finding the bypass flowrate from the transit time delays, we can find the initial flowrate.

REFERENCES

[1] Flow & Level measurement (Omega), Trans. in Measurement and Control, vol. 4.

[2] http://www.flow-network.com/flow-switches-flow-meters.html

[3] http://www.engineeringtoolbox.com/flow-meters-d_493.html

[4] Friedrich Hofmann, "Fundamentals of Ultrasonic flow measurement for industrial applications", Krohne Messtechnik Gmb H & Co. KG, Krohne 04/2001.

[5] http://www.engineeringtoolbox.com/ultrasonic-doppler-flow-meter-d_495.html

[6] Instrumentation Engineers Handbook, Vehicular Instrumentation/Transducer Committee Telemetry Group, Dec. 2007.

[7] J.D. Siegwarth "Vortex shedding flowmeters for high velocity liquids", Int.J. Heat and Fluid Flow, Vol. 10, No. 3, September 1989.

[8] T. Moazzeni, J. Ma, Y. Jiang, and Ning Li, "Flow Rate Measurement in a High Temperature, Radioactive, and Corrosive Environment," *IEEE Trans. Instrumentation and Measurement*, vol. 60, no. 6, pp. 2062-2069, June 2011.

[9] G. Por, M. Berta, and M. Csuvar, "Measurement of the coolant flow rate using correlation of temperature fluctuations," *Progress in Nuclear Energy,* vol. 43, no.1- 4, pp. 281-288, 2003.

[10] H. Knapp and G. C. Carter, "The generalized correlation method for estimation of time delay," *IEEE Trans. Acoust., Speech, Signal Process*, vol. 24, no. 4, pp. 320–327, 1976.

[11] J. N. Ash and R. L. Moses, "Acoustic time delay estimation and sensor network self- localization: Experimental results," *Journal of Acoustical Society of America*, vol. 188, no. 2, pp. 841–850, 2005.

[12] S. Hirata and T. Karagiri, "Cross-correlation by single-bit signal processing for ultrasonic distance measurement," *IEICE Tans. Fundamentals,* vol. E91–A, no. 4, pp. 1031-1037, 2008.

[13] M. S. Beck and A. Plaskowski, *Cross correlation Flowmeters, Their design and Application.* Adam Hilger, Bristol, 1987.

[14] T. Moazzeni, J. Ma, and Y. Jiang, "Measurement and Calibration of Thermal Cross-correlation-based Flowmeter Operating in Harsh Environment," *IEEE Trans. Instrumentation and Measurement*, vol. 62, no. 8, pp. 2280-2285, Aug. 2013.

[15] D. F. Young, B. R. Munsun and T. H. Okiishi, A Brief Introduction to Fluid Mechanics, John Wiley & Sons, Inc, 1997.

[16] http://mathworld.wolfram.com/LeastSquaresFitting.html

[17] J. M. Dias Pereira, P.M.B. Silva Girao, and O. Postolache, "Fitting transducer characteristics to measured data," *IEEE Instrumentation and Measurement Magazine*, vol. 4, no. 4, pp. 26-39, Dec. 2001.

[18] Joseph P. DeCarlo, *Fundamentals of Flow Measurement,* 1984.

[19] David W. Spitzer, *Industrial Flow Measurment,* 1984.

[20] Flow Measurement, edited by Béla G. Lipták,

[21] Differential Pressure Sensors for Flow Measurement in Bypass Configuration, Press Release: Product Announcement, January 2013, Sensirion AG, 8712 Staefa, Switzerland, Sensirion (the sensor company)

[22] Fundamentals of mass flow control Critical terminology and operation principles for gas and liquid MFCs, Advanced Energy.

[23] F. A. Morrison, "*An Introduction to Fluid Mechanics*", 2013.

[24] Introduction to using ANSYS FLUENT in ANSYS Workbench: Fluid Flow and Heat Transfer in a Mixing Elbow.

VITA

Graduate College

University of Nevada, Las Vegas

Elaheh Alidoosti

Degrees:

- B.S., Earth Sciences, 2003

Melli University (University of Shahid Beheshti), Tehran, Iran

Publications:

[1] **E. Alidoosti**, J. Ma, Y. Jiang and T. "Moazzeni, Numerical Simulation of Thermal Transit-Time Flow Meter for High Temperature, Corrosive and Irradiation Environment,"in *Proc. ASME 2013 Heat Transfer Summer Conference,* pp. V004T19A006; 6 pages, July 2013.

Thesis Title:

Simulation of Thermal Transit-Time Flow meter for High temperature, Corrosive and Irradiation Environment

Thesis Committee:

Chairperson, Yingtao Jinag, Ph. D.

Committee Member, Biswajit Das, Ph. D.

Committee Member, Mei Yang, Ph. D.

Graduate Faculty Representative, Hui Zhao, Ph. D.